

MODELLING OF LASER FORMING AT MACRO AND MICRO SCALES

Thesis submitted in accordance with the requirements of the University of
Liverpool for the degree of Doctor in Philosophy

by

JONATHAN DAVID GRIFFITHS

June 2012

Primary supervisor: Prof. Ken Watkins

Secondary supervisor: Dr. Geoff Dearden



Laser Engineering Group
School of Engineering
University of Liverpool
Liverpool
L69 3GH

LIST OF PUBLICATIONS

Journal Papers

1. Griffiths J., Edwardson S.P., Dearden G., Watkins K.G., Finite Element modelling of laser forming at macro and micro scales, *Physics Procedia*, Vol 5, pp 371-380 (2010)
2. Edwardson S.P., Griffiths J., Dearden G., Watkins, K.G., Temperature gradient mechanism: Overview of the multiple pass controlling factors, *Physics Procedia*, Vol 5, pp 53-63 (2010)
3. Edwardson S.P., Griffiths J., Edwards K.R., Dearden G., Watkins K.G., Laser forming: overview of the controlling factors in the temperature gradient mechanism, *Proceedings of the Institution of Mechanical Engineers, Part C: Journal of Mechanical Engineering Science*, Vol 224, 5, pp 1031-1040 (2010)
4. Griffiths J., Edwardson S.P., Boegelein T., Prandina M., Dearden G., Watkins K.G., Finite Element Modelling of the Laser Forming of AISI 1010 Steel, *Lasers In Engineering*, Vol 22, 5, pp 401-412, (2011)
5. Edwardson S.P., Griffiths J., Dearden G., Watkins, K.G., Towards Controlled Three-Dimensional Laser Forming, *Lasers in Engineering*, Vol 22, 5, pp 393 (2011)
6. Griffiths J., Edwardson S.P., Dearden G., Watkins K.G., Thermal Laser Micro-Adjustment Using Picosecond Pulse Durations, *Applied Surface Science*, Vol 258, 19, pp 7639–7643 (2012)

Conference Papers

1. Prithwani, I., Otto, A., Schmidt, M., Griffiths, J., Watkins, K. G., Edwardson, S. P., Dearden, G., “Laser Beam Forming of Aluminium Plates under Application of Moving Mesh and Adapted Heat Source”, *Proceedings of the Fifth International WLT-Conference on Lasers in Manufacturing 2009, Munich, June 2009*
2. Griffiths, J., Edwardson, S. P., Dearden, G., Watkins K. G., “Finite Element Modelling of the Laser Forming of AISI 1010 Steel”, *Proceedings of the 36th international MATADOR conference, Manchester, 2010*
3. Edwardson, S. P., Griffiths, J., Dearden, G., Watkins K. G., “Towards Controlled 3D Laser Forming”, *Proceedings of the 36th international MATADOR conference, Manchester, 2010*
4. Griffiths, J., Edwardson, S. P., Boegelein, T., Dearden, G., Watkins K. G., “The Effect of Graphite Burn Off on Multi Pass Laser Forming”, *Proceedings of IWOTE'2011, Bremen, Germany, 2011*

5. Griffiths, J., Edwardson, S. P., Dearden, G., Watkins K. G., “Short Pulse Thermal Laser Microforming Technique”, *Proceedings of IWOTE’2011, Bremen, Germany, 2011*
6. Griffiths, J., Edwardson, S. P., Dearden, G., Watkins K. G., “Laser Micro Adjustment Using Ultra Short Pulses”, *Proceedings of ICALEO’2011, Florida, USA, 2011*
7. Griffiths, J., Edwardson, S. P., Dearden, G., Watkins K. G., “Modeling of Real Temporally Variant Beam Shapes in Laser Materials Processing”, *Proceedings of ICALEO’2011, Florida, USA, 2011*
8. Griffiths, J., Edwardson, S. P., Dearden, G., Watkins K. G., “Thermal Laser Micro-Adjustment Using Ultra-Short Pulses”, *Proceedings of the 37th international MATADOR conference, Manchester, 2012*

Press Articles

1. Griffiths, J., Edwardson, S. P., Dearden, G., Watkins K. G., “Laser Micro Adjustment Using Ultra Short Pulses”, *The Laser User, Issue 65, Winter 2012*

DECLARATION

I hereby declare that all of the work contained within this thesis has not been submitted for any other qualification.

Signed: _____

Date: _____

ABSTRACT

Laser forming (LF) offers industry the promise of controlled shaping of metallic and non-metallic components in prototyping, correction of design shape or distortion and precision adjustment applications. In order to fulfil this promise in a manufacturing environment the process must have a high degree of controllability, which can be achieved through a better understanding of its underlying mechanisms.

The work presented in this thesis is primarily concerned with the use of modelling of the LF process at macro and micro scales as a means of process development.

At the macro scale, finite element (FE), finite difference (FD) and analytical modelling were used to gain a better understanding of the complex interrelation between the various process parameters for specific geometries, reducing the need for extensive empirical investigations. A particular focus of the investigation was ascertaining which of these parameters influenced the fall off in bend angle *per* pass in multiple pass LF, along with the magnitude of their influence.

The development of a full thermal-mechanical model of the LF process is detailed, as well as its application in a feasibility study into the forming of square section mild steel tubes for the automotive industry. Using this model, experimental observations were rationalized and novel scan strategies were developed which optimized the efficiency and accuracy of the process, something hitherto not possible using empirical methods alone.

At the micro-scale, FE modelling was used to determine the mechanism of deformation in a novel laser micro-forming (L μ F) technique, in conjunction with a full empirical study. The technique combined short pulse durations (20 ps) with high repetition rates (500 kHz) to generate localized heat build-up on the top surface of micro-scale stainless steel components, allowing for controlled and repeatable micro-adjustment. Modelling results suggest the mechanism works by confining the heating effect to the surface of the material, thereby selectively inducing thermal stresses and avoiding thermal damage of the component.

CONTENTS

LIST OF PUBLICATIONS	III
Journal Papers.....	iii
Conference Papers.....	iii
Press Articles	iv
DECLARATION	V
ABSTRACT	VI
CONTENTS	III
LIST OF FIGURES	VII
ACKNOWLEDGMENTS	XV
NOMENCLATURE	XVI
Greek symbols.....	xvii
GLOSSARY OF TERMS	XIX
INTRODUCTION.....	1
Research Objectives	2
Thesis Structure	3
CHAPTER 1.....	5
LITERATURE REVIEW	5
1.1 The Laser Heating Process.....	5
1.2 Laser Forming Mechanism Overview	8
1.2.1 Temperature gradient mechanism (TGM)	9
1.2.2 Buckling mechanism (BM)	13
1.2.3 Upsetting mechanism (UM)	14
1.2.4 Effect of process parameters.....	14
1.3 Metallurgy of Steels during Laser Forming	16
1.3.1 Kinetics of austenite formation.....	18
1.3.2 Martensitic transformation on cooling	19
1.3.3 Diffusivity of carbon and Fick's second law	20
CHAPTER 2.....	22
STATE OF THE ART IN MODELLING OF LASER FORMING	22
2.1 Analytical Modelling	23
2.2 Numerical Modelling	29
2.2.1 Early numerical models	30
2.2.2 Multiple scan numerical models.....	31
2.2.3 Modelling of metallurgy during laser forming.....	34
2.2.4 Laser tube bending	37
2.2.5 Non-conventional intensity distributions	40

CHAPTER 3.....	43
STATE OF THE ART IN MICRO-SCALE LASER FORMING	43
3.1 Non-Thermal Processes	43
3.2 Thermal Processes.....	46
CHAPTER 4.....	52
ANALYTICAL AND NUMERICAL MODEL DEVELOPMENT	52
4.1 Finite Element Thermal-Mechanical Model Development	52
4.1.1 Heat transfer	54
4.1.1.1 Conductive heat flux.....	55
4.1.1.2 Convective and radiative heat flux at a boundary.....	55
4.1.1.2.1 Convection	55
4.1.1.2.2 Radiation	56
4.1.2 Structural mechanics.....	58
4.1.2.1 The stress-strain relationship	58
4.1.2.2 Hardening.....	60
4.2 Finite Difference Diffusion Model Development	61
4.2.1 The heat equation	62
4.2.2 Fick's second law	65
4.2.3 Solving in MATLAB	67
4.3 Analytical Phase Transformation Model.....	68
4.3.1 The ferrite to austenite transformation	68
4.3.2 Martensitic transformation.....	69
CHAPTER 5.....	71
FACTORS AFFECTING BEND ANGLE PER PASS IN MACRO SCALE LASER FORMING ...	71
5.1 Introduction	71
5.2 Experimental Set-up and Model Development	72
5.2.1 Experimental set-up	72
5.2.1.1 Custom software	74
5.2.1.2 Metallurgical study	75
5.2.2 FE model development.....	76
5.2.2.1 Modelling the heat source.....	78
5.2.2.2 Modelling temperature dependant material properties	80
5.2.2.3 Solver settings	80
5.3 Results and Discussion.....	81
5.3.1 Thermal effects.....	81
5.3.1.1 Effect of process parameters	81
5.3.1.2 Effect of material property variation	83
5.3.2 Microstructural effects	85
5.3.3 Variation in absorption	94
5.3.4 Geometrical effects	96
5.3.5 Edge effects	97
CHAPTER 6.....	99

NUMERICAL SIMULATION OF LASER FORMING FOR FEASIBILITY STUDY	99
6.1 Introduction	99
6.2 Experimental Procedure	100
6.2.1 Experimental set-up	100
6.2.2 FE model development	103
6.3 Axial Bending	104
6.3.1 Applicability of the temperature gradient mechanism	104
6.3.2 Applicability of the upsetting mechanism and in plane shortening	107
6.3.2.1 Numerical simulation	109
6.3.2.2 Experimental study	113
6.4 In-plane Twisting	116
6.4.1 Numerical simulation	116
6.4.2 Experimental study	118
CHAPTER 7	120
LASER MICRO-ADJUSTMENT USING SHORT AND ULTRA-SHORT PULSES	120
7.1 Introduction	120
7.2 Experimental	121
7.2.1 Laser micromachining of actuator arms	122
7.2.2 Laser forming of actuators	124
7.2.3 Measuring the deformation	126
7.2.4 FE model development	127
7.2.4.1 Modelling the heat source	128
7.2.4.2 Modelling temperature dependant material properties	129
7.2.4.3 Solver settings	130
7.3 Results and Discussion	131
7.3.1 Determination of ablation threshold	131
7.3.2 Effect of pulse duration	133
7.3.3 Effect of repetition rate	136
7.3.4 Laser micro-forming using picosecond pulse durations	138
CONCLUSIONS	145
1. Factors affecting bend angle per pass	145
2. LF of square section mild steel tubes	146
3. Short and ultra-short pulse micro-adjustment	147
FUTURE WORK	150
1. Macro scale	150
1.1 Finite element modelling of laser forming	150
1.2 Laser forming of square section mild steel tubes	151
2. Micro scale	152
REFERENCES	154
APPENDIX A	165

FINITE ELEMENT MODEL VALIDATION.....	165
A.1 Thermal analysis.....	165
A.2 Bend angle analysis.....	166
APPENDIX B.....	170
TEMPERATURE DEPENDENT MATERIAL PROPERTIES	170
B.1 AISI 1010 Mild Steel.....	170
B.2 AISI 302 Stainless Steel	173
APPENDIX C.....	177
CODE EXAMPLES	177
C.1 MATLAB code.....	177
C.1.1 FDM diffusion model.....	177
C.1.2 Analytical phase transformation model	179
C.2 Visual BASIC code	182
C.2.1 Example of linear interpolation	182

LIST OF FIGURES

Figure 1 – Stages of the laser heating process with (a) solid heating, (b) melting, (c) liquid heating and (d) vaporization where L_f and L_v are the latent heats of fusion and vaporization respectively.....	6
Figure 2 - Desired heating isotherms throughout the workpiece thickness for the three principle LF mechanisms. The arrows depict the bend direction for edge clamped components.	9
Figure 3 - Simulated displacement at the edge of the sheet as a function of processing time in the TGM (80 x 80 x 1.5 mm mild steel AISI 1010, 760 W, 5.5 mm beam diameter, 35 mm/s traverse speed, 80% absorption).....	10
Figure 4 - Typical stress-strain path during a laser scan with 0→a) initial heating and restriction of thermal expansion, a→b) increasing temperature and reduction of flow stress, b→2) compressive strain development, 2→c) residual plastic strain and 2→3) compressive stress reduction to tensile stress [36].	12
Figure 5 – Space filling models for BCC (α_{Fe} and δ -iron) and FCC (γ -iron) crystal structures [46].	17
Figure 6 - Development of LF modelling [59].	22
Figure 7 – Graphical illustration of the trivial model [62].	24
Figure 8 - Graphical illustration of the two-layer model [63].	25
Figure 9 - Schematic diagram of angular deformation in the heated region with sheet thickness (h) and bend angle (α_B) [66].	28
Figure 10 - Temperature distribution after laser curve bending simulation [71].....	31
Figure 11 - Flow chart of the FE simulation [73].	32
Figure 12 - Experimental and numerical relationship between scan number and bend angle [73].	33
Figure 13 – Predicted volume fraction of transformed austenite with increasing proximity to the surface along the irradiation path (80x40x0.89 mm AISI 1010 mild steel) [79].	35

Figure 14 - Predicted volume fraction of martensite after cooling in the half cross-section of the HAZ at the centre of the component (80x40x0.89 mm AISI 1010 mild steel) [80].	36
Figure 15 - Comparison of numerical bending angle history with and without microstructure consideration (MS) with experimental measurements in multi-scan laser forming (80x80x0.89 mm AISI 1010 mild steel) [74].	37
Figure 16 – Diagram of the experimental set-up for the laser tube forming investigation with pre-loading [83].	39
Figure 17 – Schematic diagram of the loading model: (1) laser beam; (2) sheet metal; F is the pre-loading; L the length of sheet metal [84].	39
Figure 18 – Heating isotherms resulting from application of traversing real beam geometry, implemented in an FE simulation of the laser heating process [86].	41
Figure 19 - Beam geometries used in FE simulations [88].	41
Figure 20 – Simulated and experimental bending angle vs. power for the circular laser beam geometry [90].	42
Figure 21 – SEM image of grinding pattern in silicon after 14 irradiations (25 mm/s, 910 mW) [93].	45
Figure 22 – Photograph of laser formed boro-silicate glass a) towards and b) away from the beam [101].	48
Figure 23 - Schematic diagram of laser micro-adjustment of a bridge-style actuator [104].	49
Figure 24 - Variation of the reflectivity of the polarized light with different incident angles [105].	50
Figure 25 - Linear, triangular and tetrahedral elements as used in 1D, 2D and 3D FE simulations, respectively.	53
Figure 26 - Inward (left) and outward (right) radiative heat flux at a boundary.	57
Figure 27 - Idealised stress-strain curve depicting Young's modulus E , yield stress point σ_{ys} and isotropic tangent modulus E_{TISO} .	61
Figure 28 - Idealised depiction of geometry for the 1D heat equation.	63
Figure 29 - Spatial and temporal distribution of nodes used for the 1D heat equation.	64
Figure 30 - Idealised depiction of geometry for the 1D solution of Fick's second law	67
Figure 31 - Flow chart of coupled FD numerical simulation.	68

Figure 32 - Electrox intensity distribution as obtained by 3D laser profiling of a perspex beam print (top) and 2D profile trough centre of the beam compared with an ideal Gaussian intensity distribution (bottom).....	73
Figure 33 – Schematic diagram of edge clamped cantilever arrangement with component length (L) and sheet thickness (s_0). Dashed-dot lines represent irradiation path and direction.....	74
Figure 34 -Screenshot of custom software used in edge effects investigation.	75
Figure 35 - COMSOL Multiphysics FE model output for the top surface directly on the laser scan line (80 x 80 x 1.5 mm mild steel AISI 1010, 760 W, 5.5 mm beam diameter, 35 mm/s, 80% absorption, edge clamped).	76
Figure 36 - Experimentally determined stress-strain curve for AISI 1010 mild steel.....	77
Figure 37 - Experimental and theoretical elastic portion of the stress strain curve (AISI 1010).	77
Figure 38 - Meshed geometry used in FE simulations.	78
Figure 39 - 3D plot of Gaussian intensity distribution created in MATLAB.....	79
Figure 40 -Screenshot from COMSOL Multiphysics illustrating how interpolation functions can be used to apply temperature dependent material properties.....	80
Figure 41 - FE simulation of temperature at 10mm and 22mm from the irradiation path over the first six passes (80 x 80 x 1.5 mm mild steel AISI 1010, 760 W, 5.5 mm beam diameter, 35 mm/s, 80% absorption).	82
Figure 42 - FE Experimental and simulated bend angle per pass over the first six passes (80 x 80 x 1.5 mm mild steel AISI 1010, 760 W, 5.5 mm beam diameter, 35 mm/s, 80% absorption).	83
Figure 43 - Effect of varying k , C_p and α_{th} on the cumulative bend angle after six passes (80 x 80 x 1.5 mm mild steel AISI 1010, 760 W, 5.5 mm beam diameter, 35 mm/s, 80% absorption).	83
Figure 44 - The effect of varying C_p (top) and k (bottom) on α	85
Figure 45 - Single pass FE simulation of peak temperature with different scan speeds (top) and volume fraction of austenite transformation on the top surface at the centre of the sheet (bottom) (80 x 80 x 1.5 mm mild steel AISI 1010, 760 W, 5.5 mm beam diameter, 80% absorption).....	87

Figure 46 - Single pass FE simulation of volume fraction of none-ferritic phases on the top surface at the centre of the sheet (80 x 80 x 1.5 mm mild steel AISI 1010, 760 W, 5.5 mm beam diameter, 80% absorption).	88
Figure 47 - Single pass FE simulation of temporal cooling rate on the top surface at the centre of the sheet for a) 35 mm/s and b) 17.5 mm/s (80 x 80 x 1.5 mm mild steel AISI 1010, 760 W, 5.5 mm beam diameter, 80% absorption).	89
Figure 48 - Simulated martensite volume fraction on the surface of the substrate at the leaving edge after a single irradiation. (80 x 80 x 1.5 mm mild steel AISI 1010, 760 W, 5.5 mm beam diameter, 35 mm/s, 80% absorption).....	90
Figure 49 - Cumulative bend angle (80 x 80 x 1.5 mm mild steel AISI 1010, 760 W, 5.5 mm beam diameter, 35 mm/s, force cooled).	91
Figure 50 - Microscope image of heat affected zone (80 x 80 x 1.5 mm mild steel AISI 1010, 760 W, 5.5 mm beam diameter, 35 mm/s, 1 scan, 200x).	92
Figure 51 - Vickers hardness variation with increasing z-depth along irradiation path (80 x 80 x 1.5 mm mild steel AISI 1010, 760 W, 5.5 mm beam diameter, 35 mm/s, 60 scans).	93
Figure 52 - Cumulative bend angle and the bend angle per pass for a) experimental and b) simulation of LF (80 x 80 x 1.5 mm mild steel AISI 1010, 760 W, 5.5 mm beam diameter, 35 mm/s, 80% absorption).	94
Figure 53 - Cumulative bend angle (80 x 80 x 1.5 mm mild steel AISI 1010, 760 W, 5.5 mm beam diameter, 35 mm/s, force cooled).	95
Figure 54 - The geometrical effect in LF for an edge clamped arrangement.	96
Figure 55 - Effect of reducing energy density on simulated initial bend angle (80 x 80 x 1.5 mm mild steel AISI 1010, 760 W, 5.5 mm beam diameter, 35 mm/s, 80% absorption).	97
Figure 56 - Single pass FE simulation of edge effects with different scan strategies (80 x 80 x 1.5 mm mild steel AISI 1010, 760 W, 5.5 mm beam diameter, 80% absorption).	98
Figure 57 - Edge clamped rotation stage arrangement.	100
Figure 58 - Faro Arm 3D profiling system.	101
Figure 59 - Screenshot of the IP_Draw GUI.	102
Figure 60 - Screenshot of the Jog Controller and terminal.	103
Figure 61 - Geometry used in FE simulations.	103

Figure 62 - Meshed geometry used in FE simulations.	104
Figure 63 - Experimental (top) and simulated (bottom) initial bend angle in degrees as a function of traverse speed, power and distance from focus.	105
Figure 64 - Two geometries used in the FE simulations.	106
Figure 65 - FE simulated z-displacement in metres for two geometries using TGM process parameters (mild steel AISI 1010, 800 W, 6 mm beam diameter, 50 mm/s, 80% absorption).	107
Figure 66 - Depiction of in-plane shortening of component.	108
Figure 67 – Scan strategy A. Dashed-dot lines represent irradiation path and direction.	109
Figure 68 - Simulated x, y and z displacement (500 W, 8 mm beam diameter, 10 mm/s, 80% absorption).	110
Figure 69 – FE simulated z and x-displacement in metres, top and bottom respectively (mild steel AISI 1010, 500 W, 8 mm beam diameter, 10 mm/s, 80% absorption, 20x deformation scale factor).	111
Figure 70 - Scan strategy B. Dashed-dot lines represent irradiation path and direction.	112
Figure 71 - Simulated x, y and z displacement (500 W, 8 mm beam diameter, 10 mm/s, 80% absorption).	112
Figure 72 - Experimental scan strategy B. Dashed-dot lines represent irradiation path and direction.	113
Figure 73 - 3D profile of a) formed component, b) side on view revealing significant z-displacement, c) close up of side on view and d) top down view revealing minimal x-displacement.	114
Figure 74 – Appearance of HAZ after ten iterations of scan strategy B at powers of (a) 300 W, (b) 400 W and (c) 500 W (8 mm beam diameter, 10 mm/s).	115
Figure 75 - Bend angle after ten iterations of scan strategy B at various powers (8 mm beam diameter, 10 mm/s traverse speed).	115
Figure 76 - Cumulative bend angle for multiple iterations of scan strategy B (400 W power, 8 mm beam diameter, 10 mm/s traverse speed).	116
Figure 77 – Schematic diagram depicting (a) scan strategy C and (b) irradiation path for initial scan. Dashed-dot lines represent irradiation path and direction.	117

Figure 78 - Simulated overall displacement (400 W, 8 mm beam diameter, 10 mm/s, 80% absorption, 20x deformation scale factor).....	117
Figure 79 - Simulated overall displacement at the end of the component with FE post-processing image superimposed (400 W, 8 mm beam diameter, 10 mm/s, 80% absorption, 20x deformation scale factor).....	118
Figure 80 - Experimental scan strategy C. Dashed-dot lines represent irradiation path and direction.....	119
Figure 81 - Experimental (left) and simulated (right) total displacement at the end of the component (400 W, 8 mm beam diameter, 10 mm/s, 80% absorption).	119
Figure 82 – Schematic illustration of the L μ F process.....	121
Figure 83 - Schematic of stainless steel AISI 302 actuator style arms, with dimensions in μ m. The dashed line represents the irradiation path used in laser forming of the actuators.	122
Figure 84 - Number of pulses per spot and degree of pulse overlap (35 μ m beam diameter, 5 kHz repetition rate, 50 mm/s traverse speed).....	123
Figure 85 - The workpiece delivery set-up on the High-Q system: 1) laser source, 2) beam expander, 3) beam steering mirrors, 4) scanning galvanometer and 5) Aerotech 3-axis stage.....	123
Figure 86 - Heat diffusion depth with increasing pulse length for AISI 302 stainless steel.	125
Figure 87 - Custom designed sample holder: (a) aluminium frame, (b) ridge used for alignment purposes and (c) Perspex grid and arrangement of actuator arms.	125
Figure 88 - Example output from Veeco NT1100 WLI.....	126
Figure 89 - Screenshot the Alpha_B MATLAB GUI.	127
Figure 90 - Schematic of truncated stainless steel AISI 302 actuator style arms geometry used in FE simulations.	127
Figure 91 - Meshed geometry used in the FE simulations.	128
Figure 92 - Screenshot of the Pulse Shape Generator MATLAB GUI. 1) Laser process parameters, 2) Pulse shape settings, 3) Temporal pulsed relative intensity value plot, 4) Plot of individual pulse shape, 5) Initial section of MATLAB generated time list for use in COMSOL.....	129

Figure 93 - Time steps taken by solver during pulsed laser simulation (500 kHz repetition rate).....	131
Figure 94 - D^2 against E_p (top) and D^2 against Φ_0 , plotted on a Log_{10} scale (bottom).....	133
Figure 95 - Simulated temperature at the centre of the irradiation path and at four powers (1000 x 300 x 50 μm stainless steel AISI 302, 1500 mW, 35 μm beam diameter, continuous wave, 35 mm/s traverse speed).....	134
Figure 96 – FE simulated temperature (K) after a single irradiation of the geometry (1000 x 300 x 50 μm stainless steel AISI 302, 1500mW, 35 μm beam diameter, continuous wave, 10 mm/s traverse speed).....	135
Figure 97 - WLI image showing deformation of an actuator arm after 10 irradiations (1000 x 300 x 50 μm stainless steel AISI 302, 0.02 W average power, 30 μm beam diameter, 1 kHz repetition rate, 10 mm/s traverse speed).....	136
Figure 98 - Profile view of z-deformation after 10 irradiations at 200 and 500 kHz repetition rate and 3 μJ pulse energy (1000 x 300 x 50 μm stainless steel AISI 302, 35 μm beam diameter, 10 mm/s traverse speed).	137
Figure 99 - FE simulation of temperature directly beneath the beam for a stationary laser heat source at 200 kHz and 500 kHz (1000 x 300 x 50 μm stainless steel AISI 302, 3 μJ pulse energy, 35 μm beam diameter).	137
Figure 100 - Cumulative bend angle variation with successive irradiations (1000 x 300 x 50 μm stainless steel AISI 302, 35 μm beam diameter, 500 kHz repetition rate, 10 mm/s traverse speed).	138
Figure 101 - WLI image of ablated groove after 6 irradiations (1000 x 300 x 50 μm stainless steel AISI 302, 1500 mW, 35 μm beam diameter, 500 kHz repetition rate, 10 mm/s traverse speed).	139
Figure 102 - Bend angle and ablation depth variation with increasing speed, 50 and 75 μm thickness top and bottom respectively (1000 x 300 μm stainless steel AISI 302, 35 μm beam diameter, 500 kHz repetition rate, 1.5 W average power).	140
Figure 103 - Number of pulses per spot and degree of pulse overlap (35 μm beam diameter, 500 kHz repetition rate, 35 mm/s traverse speed).....	141
Figure 104 - Scanning electron microscope image of ablated groove after hatch irradiation strategy at a) 1500 mW, b) 1250 mW, c) 1000 mW and d) 750 mW (1000 x 300 x 50	

µm stainless steel AISI 302, 35 µm beam diameter, 500 kHz repetition rate, 35 mm/s traverse speed).	142
Figure 105 - Bend angle variation with increasing power, 50 and 75µm thickness top and bottom respectively (1000 x 300 µm stainless steel AISI 302, 35 µm beam diameter, 500 kHz repetition rate, 35 mm/s traverse speed).....	143
Figure 106 - Relative range of deformation and aspect ratio of components.....	149
Figure 107 - WLI image of deformed actuator arm in a comb drive arrangement.	152

ACKNOWLEDGMENTS

First of all, I would like to thank my supervisors Professor Ken Watkins and Dr Geoff Dearden for their help and support throughout my PhD and assistance in the preparation of this manuscript. In addition, special thanks go to Dr Stuart Edwardson for guidance throughout the course of this investigation and without whose expertise in the field of laser forming this work would not have been possible.

I would also like to thank all the members of the Laser Group at the University of Liverpool over the last 4 years; Leigh Mellor, Joe Croft, Olivier Allegre, Kenneth Edwards, Craig Williams, Walter Perrie, Jian Cheng, Dun Liu, Zheng Kuang, Dan Wellburn, Taku Sato and Eamonn Fearon. Thanks also to Andy Snaylam, Dave Atkinson and Tony Topping for their endless assistance in setting up experiments, using equipment and preparing samples, as without them this work could not have been conducted. I would also like to thank all postgraduate students I've worked with over the course of my PhD for contributions made to it, especially Thomas Boegelien.

I would especially like to thank MATLAB 'gurus' Marco Prandina and Yazdi Harmin for their invaluable assistance, as well as for the much welcome coffee breaks at 10.30 am, 3 pm, and 5.30 pm (not to mention 11 am at weekends). I would also like to thank Denise Bain for her advice and guidance over the years.

I would like to thank Juan Jacobo 'Jay Jay' Angulo, Nick 'John Gooseman' Underwood, Samuel Bautista Lazo, Elizabeth Christie, David 'Spanish Dave' Vallespin, Simao Marques, Sean Malkeson, Savio Varghese, Cathy Johnson, Stephen Lawson and Marina Carrion for their superb friendship and for keeping me entertained at lunch over the years. Special thanks go to Paul 'Fitzzy' Fitzsimons for sorting absolutely everything out in the flat, being a fantastic colleague and an even better friend.

Finally, I would like to thank all my family and friends, especially my parents, for their constant support throughout my PhD.

NOMENCLATURE

A_3 – Upper critical transformation temperature (K)

C_p - Specific heat capacity (J/kg.K)

C_0 – Initial carbon concentration (%wt)

C_s – Carbon concentration on surface (%wt)

d_0 – Beam diameter (m)

D_0 – Proportionality constant (m^2/s)

D – Diffusion coefficient (m^2/s)

E - Young's modulus (Pa)

E_p – Pulse energy (J)

E_{TISO} - Isotropic tangent modulus (Pa)

f – Volume fraction (1)

F_0 – Fourier number

G – Net inward radiation (W/m^2)

H – Enthalpy (J)

h - Heat transfer coefficient (W/m^2K)

J – Radiosity (W/m^2)

k - Thermal conductivity ($W/m.K$)

l – Heat diffusion length (m)

L – Component length (m)

L_p – Pulse length (s)

M_s – Martensite start temperature (K)

M_f – Martensite finish temperature (K)

P - Power (W)

p – Pressure (bar)

p_0 – Initial pressure (bar)

Q – Activation energy of diffusion (J/mol)

q_0 – Boundary heat source (W/m²)

q – Net flux of radiation (W/m²)

R - Universal gas constant (J/mol/K)

s_0 – Sheet thickness (m)

T_{amb} – Ambient temperature (K)

T_{inf} – reference temperature (K)

U – Overall heat transfer co-efficient (W/m²)

v_0 - Traverse speed (m/s)

V_m – Volume fraction of martensite (1)

Greek symbols

α - Thermal diffusivity (1/K)

α_B – Bend angle (Deg)

α_{fe} – Ferrite

α_{th} - Thermal expansion co-efficient (1/K)

γ – Austenite

ε_0 – Initial strain (1)

ε_{th} – Thermal strain (1)

ε_{el} – Elastic strain (1)

ε_p – Plastic strain (1)

ε – Total strain (1)

λ – Wavelength (m)

ν - Poisson's ratio (1)

ρ - Density (kg/m^3)

σ - Stress (Pa)

σ_s – Stefan Boltzmann constant (J/mol/K)

σ_{ys} - Yield strength (Pa)

Φ – Fluence (J/m^2)

Φ_{th} – Ablation threshold fluence (J/m^2)

ω_0 - Beam radius (m)

GLOSSARY OF TERMS

BM – Buckling mechanism

CCD – Charge coupled device

CCR – Critical cooling rate

CR – Cooling rate

CW – Continuous wave

FE – Finite element

FD – Finite difference

HAZ - Heat affected zone

LBA – Laser beam analysis

LF – Laser forming

L_μF – Laser micro-forming

LSH – Laser surface hardening

LS_μF – Laser shock micro-forming

MEMS – Microelectromechanical systems

PDE – Partial differential equation

SEM – Scanning electron microscope

TEM – Transverse electromagnetic mode

TGM – Temperature gradient mechanism

UM – Upsetting mechanism

WLI – White light interferometry

Introduction

The work presented in this thesis focuses on the use of both numerical simulation and analytical models to gain a better understanding of the mechanism of the laser forming (LF) process at macro and micro scales.

At the macro scale, LF [1,2] is a process for the shaping or correction of distortion in metallic components through the application of laser radiation, without the need for permanent dies or tools. The non-contact nature of the process has the advantage of no tool-wear, as well as sharing the high degree of flexibility associated with other laser based process such as cutting [3-5] and marking [6,7].

The process typically involves the use of defocused infrared laser radiation to thermally induce stresses in components. Through manipulation of process parameters [8] and depending on workpiece geometry, either localized plastic compressive strains or elastic-plastic buckling can be achieved, producing out of plane bends in either direction (that is, towards or away from the beam) or in-plane shrinkage.

At the micro scale, MEMS manufacturing requires accurate positioning of components as well as a high degree of reproducibility [9]. Laser micro forming (L μ F) can be utilized in accurate post-fabrication adjustment of such components, allowing for manufacturing processes with relatively large tolerances [10]. The non-contact nature of the process is also useful in accessing specific micro-components within a device which may be highly sensitive to mechanical force. As such it has potential for widespread application in both the manufacturing and microelectronics industry.

When scaling down the LF process, limits to conventional thermal forming techniques become evident, such as excessive, non-localized heating of the substrate and long thermal relaxation times [11,12]. Research has been conducted on non thermal L μ F techniques, such as laser shock micro-forming (LS μ F), a process with its origins in laser shot peening (also

known as laser shock hardening) [13]. Utilizing shockwaves generated through the breakdown of an absorptive layer, the LS μ F process induces compressive stresses in the materials upper surface, typically using nanosecond pulsed laser systems [14-16]. High repetition rate femtosecond pulsed systems have also been applied to the LS μ F process, producing bending away from the beam when used in conjunction with a pre-bend induced by favourable clamping conditions [17,18].

Whilst firmly established as a process in a research environment, both LF and L μ F have had limited application in industry thus far due to an inadequate understanding of aspects of the process, leading to insufficient process control. In order for laser forming to realize its potential as a fully controlled process in a manufacturing environment, an increased understanding of the complex interrelation between processing parameters [19] and the influence of component geometry is essential.

Numerical modelling can be used to simulate the LF process prior to experimentation, thereby determining the suitability of the process for the shaping of specific components. In addition, process parameter optimization can be conducted numerically, significantly reducing process development time and cost.

Such an approach requires the development of a robust and non-case specific model of the LF process, which is capable of accurately predicting both the nature and magnitude of deformation for a given combination of processing parameters and component geometry. A key additional consideration is the effect of laser processing on the subsequent performance properties of the component as a result of potential metallurgical transformations.

Research Objectives

The primary objective of this thesis is to develop a robust numerical simulation of the LF process for steels, capable of predicting the nature and magnitude of deformation for a given combination of processing parameters and component geometry. The model will subsequently be applied to the following:

- An investigation into the variation in bend angle *per* pass observed during multi-pass laser forming along a single irradiation path, specifically the decrease in bend angle

per pass after multiple irradiations. Thermal-mechanical FE simulations will be used to ascertain which of the various factors (such as absorptive coating degradation, geometrical effects, variation in absorption, *etc.*) identified contributes towards this phenomenon and subsequently the magnitude of their contribution.

- A numerical study into the process suitability and subsequent optimization of processing parameters for the LF of square section, mild steel tubes for the automotive industry.
- An experimental and numerical investigation into the mechanism of deformation upon the application of short and ultra-short pulse durations in the thermal L μ F of actuator-style components.

Thesis Structure

This thesis is structured as follows:

Chapter 1 provides a background on the laser heating process and how, through control of process parameters, the nature of laser induced thermal cycles can yield three distinct LF mechanisms. A summary of the metallurgical characteristics of steels during laser heating is also presented.

A review of the state of the art in both numerical modelling of the LF process at macro scales and a summary of the recent developments in LF at micro scales is presented in Chapters 2 and 3 respectively.

Chapter 4 details the theoretical development of a full thermo-mechanical FE model of the LF process. The development of two additional models, both of which utilizing post-processing data from the aforementioned FE model, are also detailed in this chapter. The first is an analytical phase transformation model which can be used to predict the microstructural composition of the component as a result of the thermal cycles induced during LF. The second is a finite difference (FD) model of the solid-state diffusion of carbon from an absorptive graphite coating into the surface of the component during laser heating.

In Chapter 5, the various analytical and numerical models developed in Chapter 4 are applied in an investigation into the controlling factors in LF, with specific consideration given to the fall off in bend angle *per* pass which is evident in multiple pass LF.

Chapter 6 presents a feasibility study into the laser forming of square section mild steel tubes for the automotive industry. The suitability of the LF process is assessed and process parameter regimes identified through use of the models detailed in Chapter 4. These models were also applied to the development of suitable scan strategies for the axial bending and in-plane twisting of the components, with analogous experimentation conducted for validation purposes.

Chapter 7 presents a numerical and experimental investigation into an entirely novel mechanism for L μ F of micro-scale components (<1000 μ m in their largest dimension), with empirical results being used to examine and optimize laser processing parameters for process development purposes.

This thesis concludes with a summary of the key contributions to knowledge resulting from the work detailed in Chapters 5 to 7, as well as recommendations for future work in the field of laser forming at macro and micro scales.

Chapter 1

LITERATURE REVIEW

Laser forming involves the use of thermally induced stresses to plastically deform a component, typically a metallic substrate. Through control of process parameters and depending on workpiece geometry, either localised plastic compressive strains or elastic-plastic buckling can be achieved [1].

The process has its origins in flame bending, a process in which an oxy-acetylene torch is employed as a heat source [20-22]. Whilst suitable for the forming of large, thick section components, such as the constituent parts of a ships hull, the relatively crude nature of the heat source means that flame bending has reached the limits of applicability in the shaping of smaller, more geometrically complex components. Lasers offer increased selectivity in terms of heating and a higher degree of controllability, with far greater potential for process automation.

This chapter details the theoretical background of the laser heating process, with specific emphasis on how the nature of laser induced thermal cycles can yield three distinct LF mechanisms through control of process parameters such as laser power, speed and spot size. In addition, a summary of the metallurgical characteristics of steels during laser heating is presented.

1.1 The Laser Heating Process

Laser based processes generally involve some thermal input from the laser beam into a substrate, good examples of which being surface treatment and direct write processes. Surface treatments often involve melting or thermally induced changes in microstructure [23-25] whilst direct writing utilizes the thermal input in order to sinter, coalesce or polymerize powder or resins in a selective manner [26-28].

Laser heating of a substrate is generally the most important factor in laser based processes. In the simplest case, this will result in heating with no loss of mass and cooling due primarily to conduction away from the irradiated area. At higher powers and intensities, however, phase change and material ejection may occur. Therefore, models of laser heating must take into consideration conductive, convective and radiative heat transfer. The stages of the laser heating process are illustrated in Figure 1.

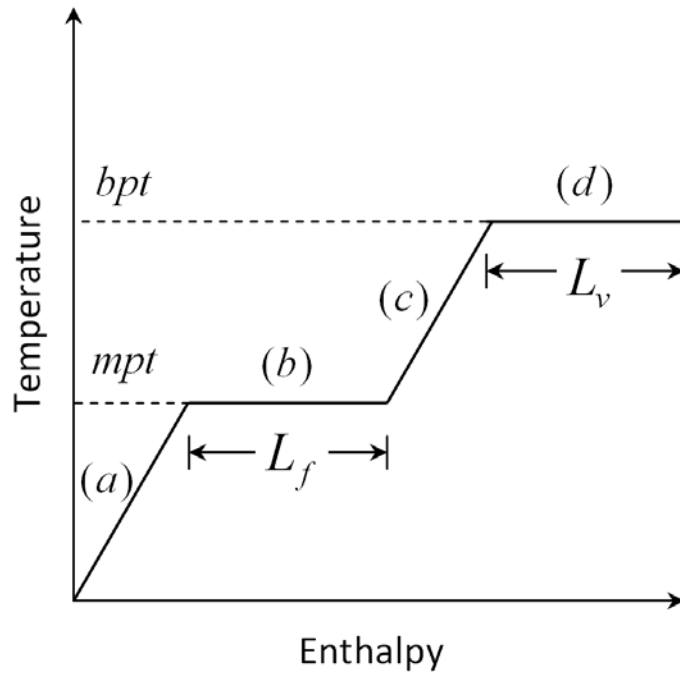


Figure 1 – Stages of the laser heating process with (a) solid heating, (b) melting, (c) liquid heating and (d) vaporization where L_f and L_v are the latent heats of fusion and vaporization respectively.

As a focused laser beam impinges on a material it heats a surface layer a few nanometres thick by the process of Fresnel absorption. Fresnel absorption is the physical process by which light is absorbed by solids and is due to the incident light wave penetrating the metal surface and imparting energy to electrons below the surface *via* the inverse Bremsstrahlung effect (the emission of photons from excited electrons is known as the Bremsstrahlung effect) [13]. The oscillating electric field of the incident electromagnetic radiation causes free electrons close to the surface of the metal to oscillate at the same frequency. Collision of these electrons with the solids metal lattice structure leads to localized lattice vibration, resulting in a rise in temperature.

The laser beam acts as a circular heat source on the surface with a heat flux distribution determined by the beam intensity distribution or transverse electromagnetic mode (TEM). The rate of heating observed is often dependant on the absorptivity of the metal surface relative to the wavelength of the laser radiation. As a rule of thumb, highly reflective surfaces (such as aluminium) typically require the use of shorter wavelength beams in order to ensure sufficient coupling of laser radiation into the surface of the material [29].

In the case of pulsed lasers typically applied at micro-scales, pulse duration times are generally lower than the thermal response time of the substrate, thus a steady state is never achieved. This limits heating to within a thin layer on the substrate surface. Conversely, continuous wave (CW) lasers used primarily in macro-scale applications result in conduction limited heating of the substrate, with the lateral and axial heat flux governed by the thermal properties of the substrate.

If the intensity of the beam and the irradiation time are sufficient, solid state phase transformations may occur, altering the microstructure of the substrate. Thermal properties which are of key importance in the LF process (see Section 1.2) such as thermal conductivity, density and thermal expansion coefficient are affected by the crystal structure of the metal lattice [30]. As such, the temperature dependence of material properties is a key consideration in modelling of the laser heating process. Upon further heating a thin layer on the substrate surface can become molten. This introduces solid to liquid phase change into what previously would have been a simple heat transfer process. Such phase transformations are associated with variation in energy *per* unit mass (enthalpy) with temperature according to the laws of thermodynamics.

If the intensity of the beam is sufficient, vaporization can occur. This process can be accelerated by the presence of a laser induced plasma just above the surface as it has the effect of enhancing the coupling efficiency of laser radiation. This avalanche effect causes the liquid to become more volatile due to surface waves, with bubble cavities breaking the surface and droplets being ejected. This in turn enhances coupling efficiency through light trapping and multiple reflections, with absorption through inverse bremsstrahlung occurring if the ejected droplets are vaporized.

Mass removal now takes place due to the surface liquid boiling away, accompanied by vapour ejection. The shear force of the reaction on the liquid surface also typically has the effect of pushing the liquid out sideways away from the beam path due the relatively lower surface tension at the hot centre of the melt pool [29].

Mathematical modelling of laser heating phenomena can provide a powerful tool for furthering an experimentalists understanding and subsequently control of a process. For instance, the results obtained from analytical models or numerical simulation can be used to predict likely outcomes or improve the efficiency of a process without the need for lengthy experimentation [31-33].

Providing the combination of process parameters used is suitable, LF is a sub-melting laser heating process. The atomic vibrations resulting from Fresnel absorption manifest themselves in thermal expansion, which can lead to elastic or plastic deformation. The localized nature of laser heating ensures that thermal expansion is restricted by the cold bulk of the substrate, often leading to compressive forces acting on the irradiated area causing plastic deformation. The following section details how, through control of process parameters and component geometry, three distinct forming mechanisms of forming can be achieved.

1.2 Laser Forming Mechanism Overview

As previously mentioned, through control of process parameters and depending on workpiece geometry, either localised plastic compressive strains or elastic-plastic buckling can be achieved [34,35]. There are three different mechanisms of laser forming, as depicted in Figure 2.

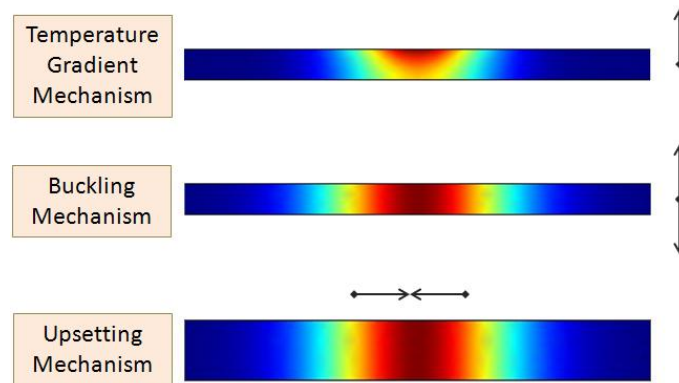


Figure 2 - Desired heating isotherms throughout the workpiece thickness for the three principle LF mechanisms. The arrows depict the bend direction for edge clamped components.

The following subsections discuss each mechanism in detail.

1.2.1 Temperature gradient mechanism (TGM)

The mechanism most commonly employed in this work is the temperature gradient mechanism (TGM), which bends the sheet metal out of plane towards the beam. A steep thermal gradient is generated locally along the irradiation path, causing the softer upper material to plastically deform. Upon cooling, providing the temperature was raised enough to cause sufficient thermal strain, elastic contraction of the previously plastically deformed material occurs on this upper surface, yielding a bend angle of 1 to 2° per pass. The temporal evolution of the deformation resulting from a single irradiation in straight line LF is illustrated in Figure 3.

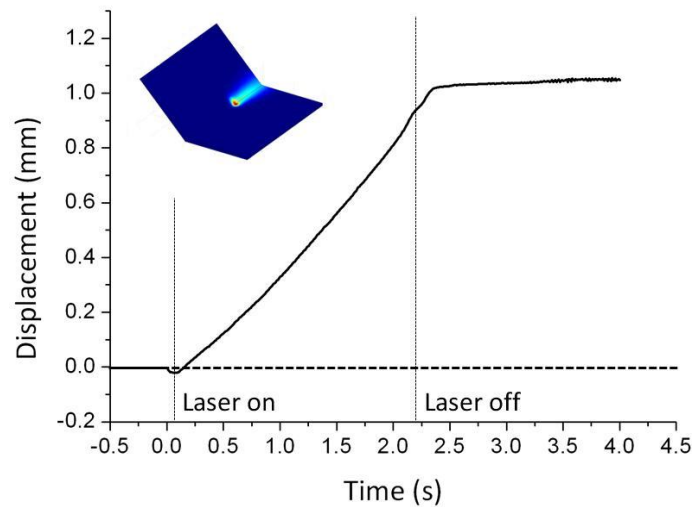


Figure 3 - Simulated displacement at the edge of the sheet as a function of processing time in the TGM (80 x 80 x 1.5 mm mild steel AISI 1010, 760 W, 5.5 mm beam diameter, 35 mm/s traverse speed, 80% absorption).

In order to establish the required thermal gradient the depth of heating must be relatively small compared to the sheet thickness, this being achieved through a suitable combination of traverse speed, spot size and laser power.

During the initial stages of laser heating, purely elastic strains are induced within the irradiated area on the upper surface of the component. These elastic strains manifest themselves as differential thermal expansion throughout the sheet thickness, causing the sheet to bend away from the beam slightly in a stage of the process known as counterbending. The magnitude of this counterbend is negligible compared to the resulting bend angle but is nevertheless detrimental to the process, as it reduces the proportion of thermal strain that is converted into plastic strain and therefore residual deformation.

Upon further heating the stress induced by thermal strain exceeds the yield strength of the material, which has decreased with increasing temperature. Further thermal expansion is restricted by the cold surrounding material, resulting in plastic deformation in the heated area. This is aided by a reduction in flow stress as a result of increased temperature.

Under typical TGM conditions, laser heating of an area on the surface of the component equivalent to the area of the incident laser beam lasts for approximately 0.2 s, after which the traversing beam is moved on and cooling occurs [19]. Cooling of the irradiated area proceeds

for the most part by a process of self quenching, in which heat is transferred to the cold surrounding material by conduction. Whilst convective and radiative heat transfer to the surroundings also contribute to the cooling process, the large temperature gradient between the irradiated area and the bulk makes self quenching the predominant mechanism. Therefore, material properties such as the thermal diffusivity of the workpiece are important considerations when choosing suitable process parameters.

During cooling, shrinkage occurs in the heated material. Due to plastic compression undergone during heating, the surface layer is shorter after cooling to room temperature than the bottom layer. This difference in degree of shortening throughout the component thickness results in the sheet bending out-of plane towards the beam.

Cooling of the irradiated area is essential for the establishment of a suitable temperature gradient upon subsequent irradiation. Therefore, a rest time between laser passes is necessary, with typical rest times in the order of 60 s; substantially longer than the duration of laser heating. This difference between the heating and cooling duration is key to the establishment of net bending angles towards the beam in the TGM. Localized counterbending as a result of thermal expansion during heating is restricted by the high stiffness of the unheated bulk of component. However, thermal contraction during cooling occurs comparatively simultaneously along the length of the irradiation path due to the relatively long time required for the component to cool, with the flow stress of the part reduced due to the elevated temperature. This leads to a substantially higher degree of residual bending towards the beam.

Jamil *et al.* [36] analysed a typical stress-strain path at the centre-point on the top surface of a sheet during a laser scan, depicted in Figure 4. Jamil identified four distinct stages in the development of the stress-strain path; pre-heating, heating, post-heating and cooling. During pre-heating the beam begins to traverse the workpiece, moving towards the measured point. The stress at this stage is tensile due to thermal expansion of the heated region, with the maximum tensile stress being reached just prior to the beams arrival at the measured point. Upon arrival of the beam at the measurement point the stress rapidly converts to compression as thermal expansion is restricted by the cold surrounding material. During the post-heating and cooling stages the beam moves on from the measurement point, resulting in a decrease in

temperature and therefore a reduction in thermal strain, leaving plastic and residual elastic strain. In addition, the compressive stress reduces and becomes tensile.

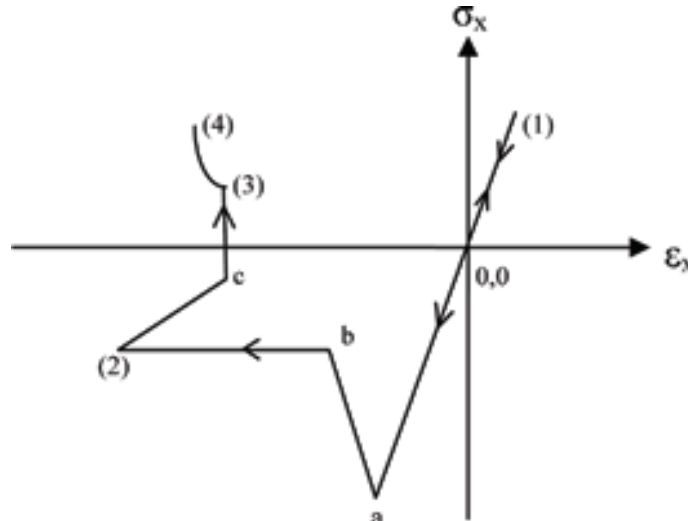


Figure 4 - Typical stress-strain path during a laser scan with 0→a) initial heating and restriction of thermal expansion, a→b) increasing temperature and reduction of flow stress, b→2) compressive strain development, 2→c) residual plastic strain and 2→3) compressive stress reduction to tensile stress [36].

Whilst firmly established as the most commonly applied LF technique, the mechanism by which the TGM induces deformation is subject to debate. Pirch and Wissenbach [37] noted that, for process parameters which satisfy the conditions for the TGM (that is, the establishment of a steep thermal gradient throughout the thickness of the sheet) there exists a critical number of irradiations, after which no further deformation occurs. It was proposed that, by irradiating the bottom surface after this critical irradiation number was reached, that bend angles of up to 180° were possible, as demonstrated numerically. However, this is in strict contrast with experimental observations [38,39]. One potential explanation for this discrepancy is the nature of the boundary conditions used in the numerical simulations conducted by Pirch, which do not take into account the elliptical nature of the beam incident on non-uniform surfaces such as those used in the pre-bended sheet investigations. Therefore, it is likely that the further bending incrementing towards 180° simulated was as a result of elastic-plastic buckling (see Section 1.2.2) on the reverse side of the sheet.

LF using the TGM is typically an incremental process due to the relatively small initial bend angles obtained. Whilst the bend angle *per* pass is fairly constant initially (typically over the first 15 to 20 passes) there is a fall off in the angle of bending achieved with successive irradiations after this. The effect of process parameters, material properties and workpiece geometry on the variation in bend angle *per* pass in straight line forming of flat sheets is a focus of the experimental and numerical work detailed in Chapter 5 of this thesis.

1.2.2 Buckling mechanism (BM)

Large beam diameters relative to workpiece thicknesses coupled with low traverse speeds typically result in elastic-plastic buckling, which can cause deformation towards or away from the beam [40,41].

The process parameters ensure that, during heating, there is as small a temperature gradient throughout the thickness of the sheet as possible, resulting in near homogeneous thermal expansion in the irradiated area. This produces in-plane thermal strain (ε_{th}) in x or y on both the top and bottom surfaces, as expressed by:

$$\varepsilon_{th} = \alpha_{th} \Delta T \quad (1)$$

where α_{th} is the thermal expansion co-efficient and ΔT is change in temperature. Theoretically, the value for ε_{th} on the irradiated surface should always be greater than on the bottom surface due to the inability to establish an entirely uniform temperature gradient in LF. However, in practice an instability (or ‘buckle’) typically forms across the workpiece as a result of the near homogeneous thermal expansion in the irradiated area. The direction of this instability can be influenced by external factors, such as plastic pre-bending or applied elastic force. In the absence of such an external factor the direction of the buckle can also be influenced by residual stresses in the substrate.

The reduction in flow stress which accompanies the temperature rise ensures that any deformation in the irradiation zone is predominantly plastic, whereas deformation away from the laser beam resulting from buckle formation is elastic. The thermally induced buckle is subsequently traversed over the remainder of the workpiece, the direction of deformation now determined by the existing buckle.

As previously stated the bend direction is dependent on residual stresses in the component or externally applied stress. Such external force could be applied in the form of a gas jet but more often takes the form of mechanical pressure or restriction.

Alternatively, a slight pre-bend in the desired direction can be employed to make the forming process by buckling more predictable. This can be achieved through mechanical force or indeed a single pass of the laser using TGM process parameters.

1.2.3 Upsetting mechanism (UM)

The UM is a mechanism of in-plane shortening in which BM process parameters are applied to a workpiece geometry that restricts out of plane bending [1].

Ideally, homogeneous heating is applied throughout the thickness of the workpiece. Thermal expansion in the irradiated area occurs as a result of this heating, reducing the flow stress of the material. As in the TGM and BM, this thermal expansion is restricted by the cold surrounding material and, providing the thermal strain induced is sufficiently high, this causes compressive stresses to develop, resulting in in-plane shortening of the workpiece.

As encountered in the BM, it is not possible in practice to achieve an entirely uniform temperature throughout the thickness of the sheet. Therefore, this slight temperature gradient manifests itself as a difference in thermal expansion, and subsequently shrinkage upon cooling. Unlike in the BM, buckle formation is prevented due to a relatively larger moment of inertia in the workpiece, leading to deformation towards the beam.

This slight bend towards the beam can be reduced by tailoring the process parameters to diminish the temperature gradient induced, typically through reduction of the traverse speed of the beam. Shi *et al.* [42] proposed a heating method in which both the top and bottom surfaces are irradiated simultaneously, reducing the dependence of temperature gradient on traverse speed as well as the out of plane deformation observed, allowing for higher throughput times.

1.2.4 Effect of process parameters

As discussed in the previous subsections, the selection of process parameters for a given workpiece geometry has a controlling effect on the mechanism by which deformation occurs

in the LF process. The process parameters, along with geometry requirements and bend direction, for each of the three principle LF mechanisms are summarized in Table 1.

Mechanism	Traverse speed	Spot size	Power	Section thickness	Bend direction
TGM	High	Small	High	Thin	Out of plane towards beam
BM	Low	Large	Low	Thin	Out of plane either direction
UM	Low	Large	Low	Thick	In-plane shortening

Table 1 - LF mechanism process characteristics.

As highlighted in Table 1, laser power, traverse speed and spot size are the three main process parameters in LF when using CW laser sources. For pulsed laser sources, such as those commonly used in micro-scale laser forming (see Chapter 3), pulse duration and repetition rate also play an important role.

Whilst the information in Table 1 is useful as a general rule, it is important to quantitatively establish which mechanism dominates for a given combination process parameters and workpiece geometry. The Fourier number, Equation (2), is a useful quantitative indication of the likely mechanism [43]:

$$F_0 = \frac{\alpha_{th} d_0}{\nu_0 s_0^2} \quad (2)$$

where d_0 is the beam diameter, ν_0 is the traverse speed and s_0 is the sheet thickness. The Fourier number can be used to characterize the nature of heat conduction for a given laser-material interaction time, equal to the beam diameter divided by the traverse speed (d_0/ν_0). For thin section sheets, low Fourier numbers suggest that the TGM will be the predominant mechanism, with the BM and UM operating at higher Fourier numbers. Typically, Fourier numbers of less than 1 correspond to TGM parameters [13], although much higher values have been shown to result in bending towards the beam in practice.

Li *et al.* [44] conducted an experimental investigation into the effect of the Fourier number on the direction of bending for 80 x 80 x 0.89 mm AISI 1010 steel sheet. The Fourier number was varied between 6.25 and 7.75 by adjusting the focal spot size of the incident beam

independently of all other process parameters. Between Fourier numbers of 6.25 and 6.6 the TGM mechanism dominated due to the steep thermal gradient induced throughout the sheet thickness, as indicated by out of plane bending towards the beam. However, for Fourier number values between 6.6 and 6.8, Li identified a critical region in which neither the TGM or BM dominated; the bend direction fluctuated between towards and away from the beam. At higher Fourier values the bend direction was always away from the beam.

The Fourier number correctly identifies laser power, traverse speed, beam diameter, and sheet thickness as key factors influencing the mechanism by which deformation in LF occurs whilst also taking into account the thermal diffusivity (α_{th}) of the substrate. Shi *et al.* [45] identified the critical conditions under which the BM is the dominant mechanism for thin sheet LF, Equation (3), taking into account the Poisson's ratio (ν) of the substrate:

$$\frac{P}{s_0^2} \left(\frac{d_0}{\rho C_p s_0 v_0} - \frac{s_0}{3k} \right) \geq \frac{\pi^3}{20.76(1+\nu)A\alpha_{th}} \quad (3)$$

where P is the power, s_0 is the sheet thickness, d_0 is the beam diameter, v_0 is the traverse speed, k is the thermal conductivity, ρ is the density, C_p is the specific heat capacity and A is the absorption co-efficient.

1.3 Metallurgy of Steels during Laser Forming

As mentioned in Section 2.1, the generation of heat as a result of the application of laser radiation is the most significant aspect of the majority of laser based processes. It is therefore important to be cognisant of the effect of the induced thermal cycle on the metallurgical properties of the component during processing.

Applications such as laser surface hardening (LSH) [46] use the selective nature of laser heating to induce metallurgical change in components to improve wear resistance and corrosion properties in specific areas where it is needed.

Metallurgical considerations are important in the LF process due to the high cooling rates encountered in the TGM and the relatively long amount of time at elevated temperatures associated with the BM and UM.

The stable forms of iron in iron-carbon alloys at room temperature are ferrite (α_{Fe}) or the metastable intermediate compound iron-carbide, known as cementite (Fe_3C). Ferrite has a body centred cubic (BCC) crystal structure (see Figure 5). For pure iron, upon heating to above 1185 K α_{Fe} fully transforms to face centred cubic (FCC) austenite, or γ -iron. Further heating to above 1665 K results in the austenite transforming to BCC δ -iron, before melting occurs at 1810 K.

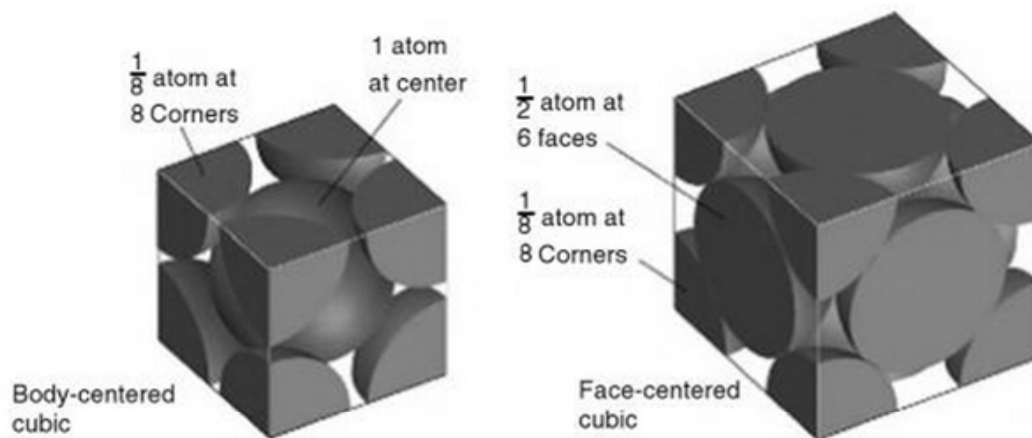


Figure 5 – Space filling models for BCC (α_{Fe} and δ -iron) and FCC (γ -iron) crystal structures [46].

The microstructural composition at elevated temperatures is also dictated by the carbon concentration in the alloy, the addition of which to ferritic iron has a significant strengthening effect on the material. Carbon in iron is an interstitial alloying constituent with varying degrees of solubility in the various phases. Due to the shape and size of the interstitial sites in BCC and FCC crystal structures, the maximum solubility of carbon in austenite (2.14 wt%) is approximately 100 times greater than in ferrite (0.022 wt%).

Whilst iron-carbon equilibrium diagrams are suitable for predicting phase composition on the basis of temperature for isothermal conditions, during non-isothermal laser heating the time dependent kinetics of the phase transformations must be considered. The following subsections detail the key phase transformations associated with the LF process in mild steels; ferrite to austenite during laser heating and subsequent austenite to martensite during rapid cooling.

1.3.1 Kinetics of austenite formation

Whilst the iron-carbon equilibrium phase diagram describes the temperature dependence of crystal structure in steels, given the short heating times associated with the LF process, it is necessary to consider the time dependence or rate such transformations.

The ferrite to austenite ($\alpha_{\text{fe}} \rightarrow \gamma$) transformation involves the nucleation of γ phase from the α_{fe} matrix and growth of the γ phase by diffusion. Austenite nucleates on ferrite grain boundaries and grows rapidly into the parent phase. This solid-state transformation behaves kinetically, with the volume fraction f of austenite as a function of time t described by the Johnson-Mehl-Avrami (JMA) equation; an equation which can be used to describe the kinetics of transformations involving nucleation and growth [47-51]. At constant temperature, the JMA equation can be expressed as:

$$1 - \alpha_{fe} = f = \exp - (k(T)t)^n \quad (4)$$

where n the JMA time exponent, a non temperature dependant constant whose value is determined by the nucleation and growth mechanism. The equation describes three different processes that occur during the transformation; nucleation, growth and the impingement of the grains of the new phase. The term $k(T)$ is the temperature dependant rate constant for nucleation and growth rate and can be calculated using the Arrhenius equation:

$$k(T_i) = k_0 e^{-\left(\frac{Q}{RT_i}\right)} \quad (5)$$

where Q is the activation energy of the $\alpha_{\text{fe}} \rightarrow \gamma$ transformation involving both the nucleation and growth processes of the γ phase and R is the universal gas constant. Therefore, temperature has a significant influence on the nucleation and growth rate of the γ phase and constitutes an important metallurgical consideration during the LF process in which short heating times and high peak temperatures are typical. Although the growth process is diffusion controlled as both ferrite and austenite are of the same element, the diffusion rates are very fast as the diffusion distances are very short (less than one lattice spacing in the case of pure iron).

1.3.2 Martensitic transformation on cooling

Martensite is a non-equilibrium phase in steels and as such does not appear on the iron-carbon equilibrium phase diagram. When cooling following austenitization in the heat treatment of steels, providing the cooling rate is sufficiently low, transformation of austenite to ferrite occurs due to the instability of austenite at room temperature.

Martensite formation occurs when austenitized iron-carbon alloys are rapidly cooled (or ‘quenched’) at high cooling rates (CR). A diffusionless shear displacement of iron atoms in the FCC austenite lattice occurs as a result of this rapid temperature change, trapping any carbon present in the interstitial sites due to insufficient time for diffusion to take place [52]. The result is a supersaturated solution of carbon in iron with a body centred tetragonal (BCT) crystal structure, similar to BCC ferrite although with one elongated (or ‘distorted’) dimension [53]. The amount of distortion is dependent on the carbon content of the structure.

Martensitic transformation initiates when cooling reaches the martensite start temperature (M_s). The M_s temperature is dictated by the relative abundance of alloying elements which can enter into solid solution in austenite, according to Equation (6).

$$M_s (^{\circ}C) = 539 - 423(\%C) - 30.4(\%Mn) - 17.7(\%Ni) - 12.1(\%Cr) - 7.5(\%Mo) \quad (6)$$

A progressively larger volume fraction of austenite is transformed to martensite until the martensite finish (M_f) temperature is reached and the transformation is complete. At this temperature all austenite should have transformed to martensite. However, a small volume fraction of austenite is often not transformed and is referred to as retained austenite. The volume fraction of retained austenite in quenched steels typically increases with increasing relative abundance of alloying elements as the M_f temperature is reduced, sometimes to below room temperature.

For martensite to form, rapid cooling is required so that the metastable austenite phase reaches the M_s temperature and higher temperature transformations, such as the austenite to ferrite and pearlite transformation, are suppressed. The threshold or critical cooling rate (CCR) which is required for martensite formation is dependent on the relative abundance of alloying elements and can be determined from continuous cooling transformation (CCT)

diagrams for a given steel [54]. Using CCT diagrams, the final microstructural composition of steel for a given cooling rate can be predicted. Depending upon where the superimposed cooling rate intersects the curves, which represent the various phases, predicts the resulting microstructure. For only martensite to form, the superimposed cooling rate should not intersect any of the curves prior to reaching the M_s temperature. It should be noted that martensite can co-exist with other microstructures.

Martensitic steels typically exhibit high hardness and tensile strengths. However, they are also brittle, exhibiting negligible ductility. Due to the higher density of austenite compared to martensite there is a net volume increase upon martensitic transformation in steels. This phenomena has been exploited in the LSH technique to improve the fatigue properties of components by selectively inducing martensitic transformation on the surface. The aforementioned volume expansion associated with the transformation leads to the development of compressive stresses on the surface of the component. As fatigue cracks are often initiated by surface tensile stresses, such stresses must be sufficient to overcome this residual compressive stress prior to crack formation and propagation [13]. However, during the LF process martensitic transformation is highly undesirable due to its detrimental impact on the ductility of the component. As such, the induced thermal cycle forms an important consideration when selecting appropriate process parameters in LF.

1.3.3 Diffusivity of carbon and Fick's second law

Carbon exhibits rapid diffusivity in iron due to its relatively small size when compared to other alloying elements in steel, a phenomena that has exploited by metallurgists to increase the hardness of steels in a process called carburizing [55]. During carburization, steels are typically heated in a furnace with a carbon rich atmosphere, such as in the presence of CO, to within their austenitic range (approximately 1300 K). This results in a carbon concentration gradient in the steel, facilitating solid-state diffusion of carbon into the surface. Upon appropriate heat treatment, such high carbon surfaces can be made to exhibit greater strength and wear resistance relative to the bulk of the component.

The use of lasers in the carburizing process is well established [56,57]. The most common of the laser carburizing techniques is laser surface alloying, in which the surface of a component

is selectively melted in the presence of a carbon source such as graphite. Laser carburizing can also proceed by solid-state diffusion of carbon into austenite in the steel surface. This is of particular relevance to the laser forming process because, as detailed in Section 4.2.3, absorptive coatings are often required as a means of increasing the coupling efficiency of laser radiation into the substrate. The coating most commonly used is graphite in the form of a spray, due to the ease at which it can be removed after processing and the high coupling efficiencies that can be achieved (approximately 80% for wavelengths of 10.6 μm). During laser heating carbon from this absorptive coating can diffuse into the component surface, thereby increasing the hardness. As such, the thermal cycle induced by the laser on the surface of the component is an important consideration regarding solid-state diffusion of carbon during the LF process. The relationship between time at elevated temperature t and carbon concentration at depth z is given by Fick's 2nd law of diffusion [58]:

$$\frac{\partial C}{\partial t} = D \frac{\partial^2 C}{\partial z^2} \quad (7)$$

where C is the concentration of carbon and D is the temperature dependent diffusion coefficient (m^2/s) which can be calculated using:

$$D = D_0 e^{-\left(\frac{Q}{RT}\right)} \quad (8)$$

where D_0 is the proportionality constant (m^2/s), Q is the activation energy of diffusion (J/mol), T is the temperature (K) and R is the universal gas constant (8.3 J/mol/K) where D_0 and Q are phase dependent.

Chapter 2

STATE OF THE ART IN MODELLING OF LASER FORMING

Extensive work has been conducted on modelling the LF process. Initially, analytical models were developed, the aim of which was to assess the suitability of various combinations of process parameters and give a reasonable estimate of the bend angle. With the increasing processing power of computers, ever more accurate numerical models of the LF process have been developed which have allowed the user to assess the applicability of process parameters and scan strategies in conjunction with complex, realistic geometries.

Shen [59] summarized the development of LF modelling since its origins in the 1980s, as shown in Figure 6.

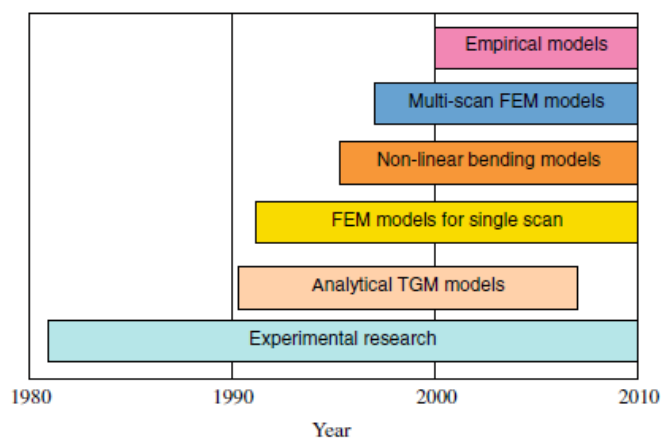


Figure 6 - Development of LF modelling [59].

Empirical models, such as those proposed by Cheng *et al.* [60,61], are supervised neural networks based on genetic algorithms; optimization techniques which utilize probabilistic transition rules. Input parameters such as spot diameter, traverse speed, power, and geometry can be optimized for a specific application using empirically obtained data from previous

experiments in an iterative heuristic approach. However, for the purposes of this investigation the focus will be on explicit simulation of the process.

The following subsections detail the state of the art in both analytical and numerical modelling of the LF process relevant to this thesis.

2.1 Analytical Modelling

Vollertsen [62] proposed an analytical or ‘trivial’ model of the TGM in which a slice through the section of a substrate is considered. This section comprises two layers; an upper layer heated by laser and a bottom layer, which remains at room temperature. Firstly, the temperature gradient (ΔT) is calculated using:

$$\Delta T = \frac{2AP}{\rho v_0 s_0 C_p} \quad (9)$$

where A is the absorption co-efficient, P is the laser power, ρ is the density, v_0 is the traverse speed, s_0 is the sheet thickness, l is the initial length of the heated zone and C_p is the specific heat capacity. The heat flux is then used to calculate the change in length (Δl) as a result of linear thermal expansion *per* unit length in the heated layer:

$$\Delta l = \alpha_{th} \Delta T l = \frac{2AP\alpha_{th}}{\rho v_0 s_0 C_p} \quad (10)$$

where α_{th} is the coefficient of thermal expansion. Assuming that all thermal expansion results in plastic compression this can then be translated into a net bending angle (α_B) for small angles from entirely geometrical considerations (11).

$$\tan\left(\frac{\alpha_B}{2}\right) \approx \frac{\alpha_B}{2} = \frac{\Delta l}{s_0} \quad (11)$$

Therefore, the solution for the bend angle (α_B) in the TGM according to the two-layer model can be calculated by assuming that the new lengths pivot about the centreline of their respective cross sections and is described by Equation (12).

$$\alpha_B = \frac{2\Delta l}{s_0} = \frac{4AP\alpha_{th}}{\rho\nu_0 s_0^2 C_p} \quad (12)$$

The two-layer model is depicted in Figure 7.

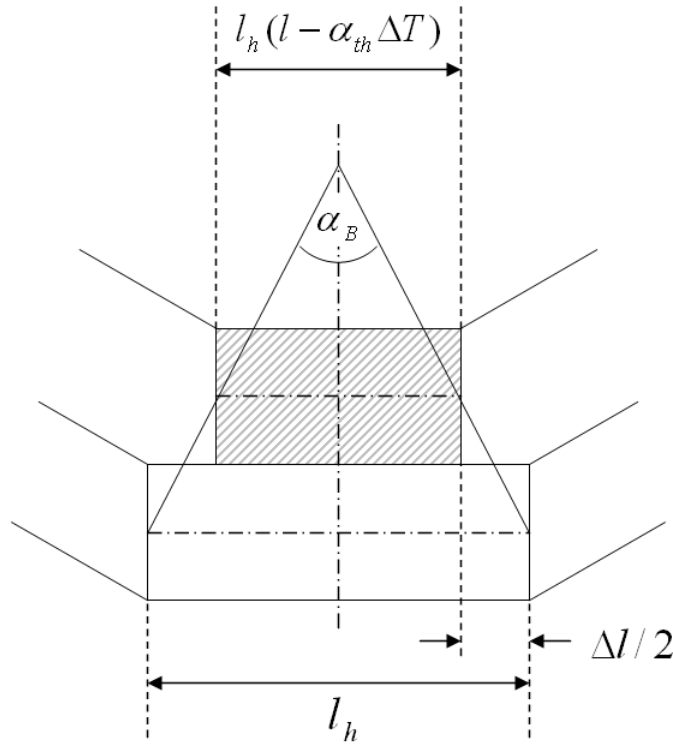


Figure 7 – Graphical illustration of the trivial model [62].

A number of assumptions are made in the trivial model, the most striking of which are the step profile of the temperature distribution throughout the thickness of the sheet and the non-dependence of the net bending angle on the forces and moments during cooling of the sheet. Additionally, all linear expansion results in plastic deformation, which would not be the case in reality. As a result of the latter, the bend angle is typically over-estimated.

In order to address this overestimation, Yau [63] proposed a modified version of the trivial model in which the counterbend during laser heating is accounted for, therefore assuming that a portion of the thermal expansion is used for elastic deformation. This was achieved by using two analytical solutions; one for the counter-bending angle and one for the bend angle at the end of the cooling cycle. For the latter, the dependence of bend angle on the Young's

modulus (E) and yield strength (σ_{ys}) of the substrate were considered. The equation for the net bend angle according to Yau's model is:

$$\alpha_B = \frac{2l\alpha_{th}PA}{2\rho C_p v_0 s_0^2} - \frac{36l\sigma_{ys}}{s_0 E} \quad (13)$$

where l is the half length of the heated zone. Another solution to the overestimation of bend angle in the trivial model proposed by Liu *et al.* [64] simply involved the introduction of a correction factor (η) to the laser power (ηP) to account for heat losses to the surroundings and elastic deformation during counterbending.

As previously mentioned, a key assumption in the trivial model is a non-dependence of bending angle on forces and moments during cooling of the sheet. Also, the heated layer is arbitrarily considered to be half the sheet thickness, thereby not allowing for consideration of thermal conductivity. To address these assumptions, Vollertsen proposed the two-layer model; another geometrically based model for prediction of the bend angle in TGM dominated LF processes, also comprising a heated and non-heated layer [35].

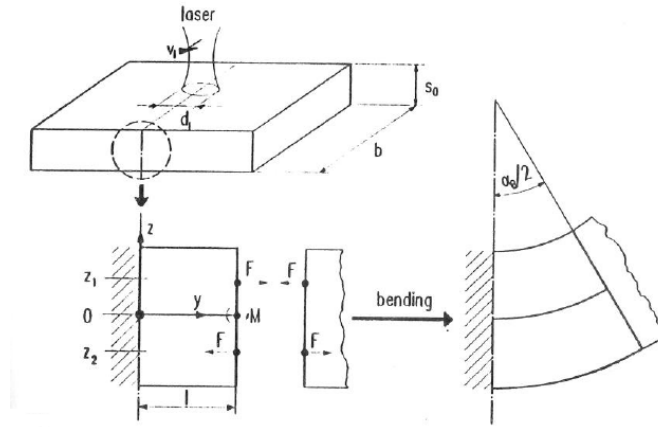


Figure 8 - Graphical illustration of the two-layer model [63].

In this model, the bend angle is defined geometrically by the difference in strains between a heated upper layer (ε_1) and non-heated lower (ε_2) layer according to Equation (14).

$$\tan\left(\frac{\alpha_B}{2}\right) \approx \frac{\alpha_B}{2} = \frac{l(\varepsilon_2 - \varepsilon_1)}{0.5s_0} \quad (14)$$

The normal strain in the upper and lower layers can be calculated using Equations (15) and (16) respectively:

$$\varepsilon_1 = \frac{F}{E_1 A_1} - \frac{M_1}{E_1 I_1} z_1 + \alpha_{th} \Delta T \quad (15)$$

$$\varepsilon_2 = \frac{F}{E_2 A_2} - \frac{M_2}{E_2 I_2} z_2 \quad (16)$$

where F is the bending force, E is the Young's modulus, A is the section area, M is the bending moment and I is the second moment of area. There is no thermal expansion term in Equation (16) as it is assumed that the lower layer remains un-heated. A further assumption is that all thermal expansion results in plastic deformation, as was the case for the trivial model. Therefore, on cooling the strain in the upper layer is given by Equation (17).

$$\varepsilon_1 = \frac{F}{E_1 A_1} - \frac{M_1}{E_1 I_1} z_1 - \alpha_{th} \Delta T \quad (17)$$

By combining Equations (16) and (17) for the local strains of the top and bottom layers an expression for the net bending angle can be derived, Equation (18).

$$\alpha_B = \frac{12\alpha_{th}\Delta T l s_1(s_0 - s_1)}{s_0^3} \quad (18)$$

This expression, however, contains three unknown parameters; the temperature gradient (ΔT), length of the heated layer (l) and thickness of the heated layer (s_l). As shown in Equation (9), the temperature rise in the heated layer is dependent upon the sheet thickness and length of the heated layer. Thus, by using an energy approach, these parameters can be calculated simultaneously. It is arbitrarily assumed that the thickness of the heated layer is half the sheet thickness. This allows for the formulation of an expression for bending angle using only known parameters, Equation (19).

$$\alpha_B = \frac{3AP\alpha_{th}}{\rho v_0 s_0^2 C_p} \quad (19)$$

More recently, Shen [65] developed a model which utilized an analytical solution to the heat equation (see Section 4.2.1 for more detail on the heat equation) to calculate more realistic temperature gradients throughout the sheet thickness:

$$T(t, z) - T_0 = T(t, z) + \sum_{n=1}^{\infty} [T(t, z_n) - T(t, z_{-n})] \quad (20)$$

where z is the distance from the irradiated surface and n is the current time step number. The model proceeds in a iterative fashion, with the results for the temperature gradient throughout the thickness of the substrate being used to calculate the corresponding stress and strain, as related by:

$$\varepsilon_{\sigma} = \begin{cases} \frac{\sigma}{E} & EL \\ \frac{\sigma_{ys}}{E} + \frac{\sigma - \sigma_{ys}}{E_{TISO}} & PL \\ \frac{\sigma}{E} + (\sigma_{max} - \sigma_{ys}) \left(\frac{1}{E_{TISO}} - \frac{1}{E} \right) & UL \end{cases} \quad (21)$$

where E_{TISO} is the tangent modulus of plastic deformation and σ_{max} is the maximum stress in the loading history. EL, PL and UL refer to elastic loading, plastic loading and unloading, with the latter also applicable to reloading. It should be noted that this model neglects work hardening and creep effects. Both the Young's modulus and plastic deformation modulus are temperature dependent and defined by a bi-linear approximation of a stress/strain curve (see Section 4.1.2.2).

A key advantage of Shens model is its ability to predict the mechanism of deformation for a given combination of process parameters, as the characteristic depth of plastic compression is predicted. The model showed good agreement with existing experimental data for single pass LF for both TGM and BM process parameter regimes.

Shi *et al.* [66] proposed an analytical model of the TGM based on the temperature distribution throughout the thickness of a thin metallic sheet. The workpiece of length L is divided into three sections; a heated zone (zone 1) and two normal temperature zones (zones 2 and 3) either side of it, with deformation in zone 1 depicted in Figure 9.

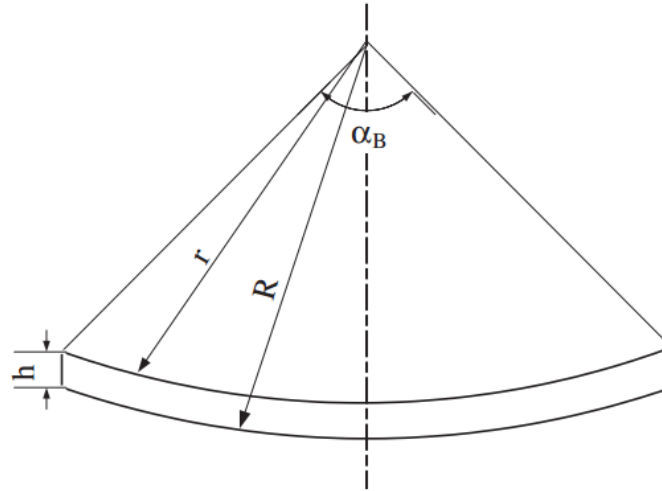


Figure 9 - Schematic diagram of angular deformation in the heated region with sheet thickness (h) and bend angle (α_B) [66].

During laser heating, differential thermal expansion as a result of a steep laser induced thermal gradient results in non uniform thermal expansion. Due to the constraint of thermal expansion in zone 1 as a result of the unheated zones either side of it, the total thermal expansion (ΔL_T) consists of both plastic and elastic components:

$$\Delta L_T = \Delta L_P + \Delta L_E \quad (22)$$

where ΔL_E and ΔL_P are the elastic and plastic deformations respectively. The elastic deformation can be expressed as follows:

$$\Delta L_E = \frac{d_e \sigma_{ys}(T)}{E(T)} \quad (23)$$

Where σ_{ys} is the yield strength, d_e is the width of the deformation zone and E is the Young's modulus. Due to the difficulty in implementing temperature dependent material properties in analytical models, the ratio of yield strength to Young's modulus over a temperature range of 20 to 600 °C was averaged to 1.727×10^{-3} . From Figure 9, the bend angle can be determined geometrically on the basis of differential thermal expansion:

$$\alpha_B = \frac{\Delta L_{1P} - \Delta L_{2P}}{R - r} = \frac{\Delta L_{1P} - \Delta L_{2P}}{h} \quad (24)$$

where ΔL_{P1} and ΔL_{P2} are the transverse plastic shrinkages on the top surface and bottom surface respectively. Strictly speaking, when operating under TGM conditions no plastic compressive deformation should occur on the bottom surface. Therefore in such cases the bend angle can be expressed as follows:

$$\alpha_B = \frac{\Delta L_{1P}}{h} = \frac{\Delta L_{1T} - \Delta L_{2E}}{h} = \frac{\Delta L_{1T} - 1.727 \times 10^{-3} d_e}{h} \quad (25)$$

It was claimed that the results from a parametric study conducted using both the analytical model and an experimentally validated FE numerical model showed approximate agreement.

With the advent of ever more powerful computers, research activity involving analytical modelling has decreased drastically in favour of more complex numerical modelling. It is worth noting, however, that analytical solutions continue to be used in conjunction with numerical simulations, using readily available post-processing data to model peripheral phenomena that do not require coupling into the thermal or mechanical aspects of the simulations (a good example of which is metallurgical aspects of the LF process, see Section 4.3).

2.2 Numerical Modelling

One of the key challenges in modelling the LF process is the complex interrelation of the various process parameters and the geometry. In addition, the two distinct physical phenomena of heat transfer and structural mechanics must be effectively coupled. These considerations necessitate a more holistic approach, the complexity of which requires the use of numerical methods to implement.

In simulation of the LF process, numerical methods (see Chapter 4) offer the potential to model multiple irradiations over long simulation times for complex, realistic geometries which also incorporate variable material properties that are pressure or temperature dependent.

Due to the necessity of coupling heat transfer and structural mechanics, and the desire to use realistic geometries, FE has become the predominant method for simulation of the LF process. The FE method is a numerical technique for solving PDEs which has found

widespread use in the simulation of physical phenomena, aided by ever greater computer processing power [67], as discussed in Section 4.1.

2.2.1 Early numerical models

In 1996, Zhong and Shichun [68] made specific mention of the complicated nature of the coupling between the thermal and mechanical aspects of the LF process, surmising that, given the relatively small fluctuation in strain, the temperature field could be calculated independently, neglecting the effect of thermal stresses.

The FE method was used to simulate the three-dimensional temperature field in steel as a result of heating with a Gaussian intensity distributed heat source over a range of process parameter combinations. The effect of process parameters on the thermal gradient between the top and bottom surface was investigated and proposed as a means of selecting suitable process parameters for the TGM.

The results of the simulations were validated against results from literature calculated using the finite difference numerical method and found to be in good agreement. A follow up publication by the same authors [69] coupled the mechanical aspects of the process to the aforementioned thermal simulation, using the model to simulate the displacement field and magnitude of stress field variation during LF.

Zhang *et al.* [70,71] used Zhong's thermal-mechanical model to analyse the transient temperature and displacement fields during curve bending of 80 x 50 x 0.8 mm Ti₆Al₄V sheet metal. The curve was described by B-spline interpolation as a Bezier curve, as depicted in Figure 10.

Zhang identified laser power, traverse speed and spot diameter as key parameters affecting the temperature field during laser heating and conducted a limited parametric study to investigate the magnitude of influence each had on the peak temperature simulated. Given that the desired forming mechanism was the TGM, the effect on simulated temperature gradient at the centre of the irradiation path was also monitored.

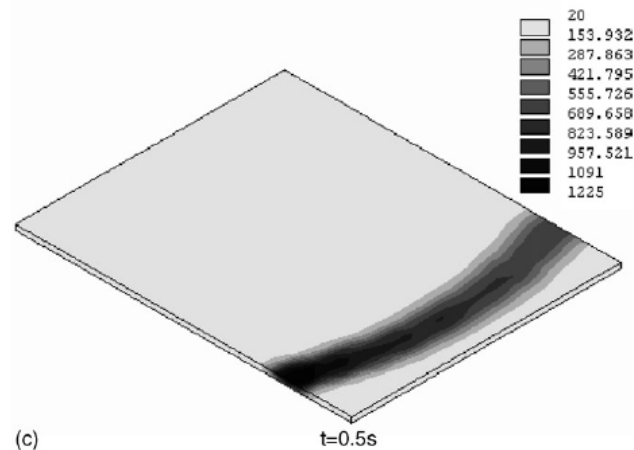


Figure 10 - Temperature distribution after laser curve bending simulation [71].

Kyrsanidi [72] also mentions the complexity of thermal-mechanical coupling in modelling of the LF process and suggests this as the reason for the process specific nature of analytical approximations for the net bending angle. This process specific nature restricts the use of analytical models in parametric studies required for the rationalisation of empirical observations.

A full thermal-mechanical simulation of the LF process was developed in ANSYS, implementing a Gaussian distributed heat source. As in this investigation, a bi-linear curve approximating a stress strain curve was used to dictate the relationship between stress and strain. The results of the limited parametric study conducted showed good correlation with the numerically simulated deformation.

2.2.2 Multiple scan numerical models

Hu *et al.* [73] developed a linearly coupled thermal-mechanical FE simulation of the LF process in ANSYS, notable for being one of the earliest published instances of multi-scan simulation of the process. A flow chart of the simulation is shown in Figure 11. The 12000 element model consisted of a uniform mesh distribution, Gaussian distributed heat source and incorporated full temperature dependent material properties as sourced from literature.

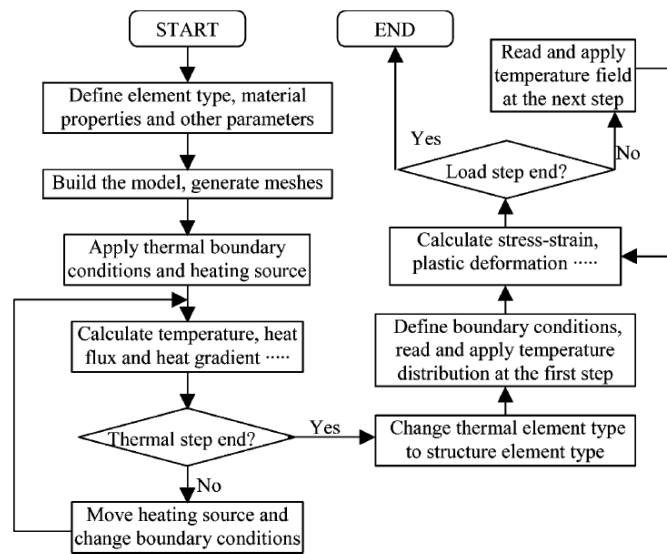


Figure 11 - Flow chart of the FE simulation [73].

As part of a wider investigation into the capabilities of numerical modelling to predict the transient stress and strain fields during LF, the effect of 20 sequential irradiations was simulated for 50 x 100 x 1.5 mm AISI 304 and aluminium sheet, with results showing good agreement with analogous experimentation.

The same model was utilized in a follow up publication by the same authors to simulate the transition between TGM and BM operating conditions, as shown in Figure 12. Whilst keeping both the traverse speed and spot size of the beam constant at 10 mm/s and 2 mm, the power was increased from 250 to 300 W. This increase in power corresponded to a decrease in the thermal gradient, sufficient enough for buckling to become the dominant mechanism of deformation; causing the sheet to bend away from the beam.

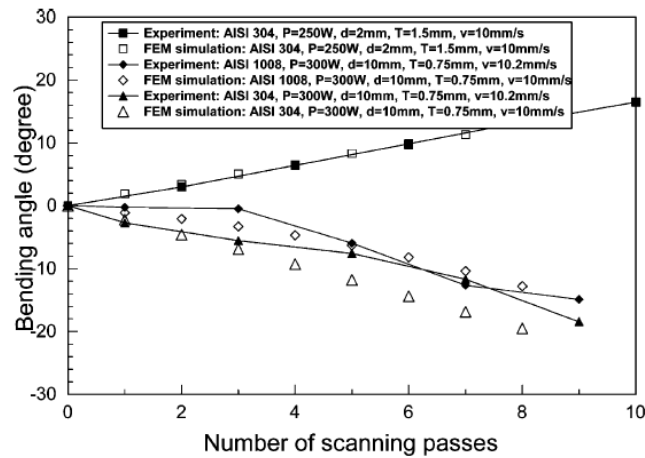


Figure 12 - Experimental and numerical relationship between scan number and bend angle [73].

Cheng *et al.* [74] also developed a numerical simulation of multiple pass LF in order to ascertain the magnitude of influence that microstructural transformation has on flow stress during LF, as detailed in Section 2.2.3.

The effect of multiple simultaneous as opposed to sequential irradiations was investigated numerically by Shen *et al.* [75]. A linearly coupled thermal-mechanical FE simulation of the LF process was developed in ANSYS and applied to the forming of 40 x 40 x 4 mm steel sheet. Only the thermal expansion co-efficient, Young's modulus and yield strength were considered temperature dependent.

It was found that, providing the scans were conducted at an optimal distance apart, a greater degree of out-of plane deformation could be attained when using simultaneous scans in conjunction with TGM process parameters. When the scans were too close to one another, however, the temperature fields induced by each beam interfered with one another, adversely affecting the temperature gradient achievable and therefore reducing the amount of deformation.

Along with intensive memory usage, one of the key challenges in the numerical modelling of multi-scan LF is simulation time and effective use of computational power. Pitz *et al.* [76-78] noted the long computational times associated with the simulation of large plate three-dimensional laser forming. A 'moving mesh' was proposed, in which the high mesh density

required in area of interest is roughly the size of the beam and is moved synchronously with it during the simulation. The substrate was a 100 x 100 x 2 mm aluminium plate, with only inward heat flux from the laser source and conduction within the plate considered in the simulation (that is, convection and radiation were neglected).

Experimentally determined initial bend angle and temporal temperature profiles were used to validate the simulation results, showing reasonable agreement. The focus of the paper was on reducing the computational time, rather than the effect of the various spatial discretization techniques on the accuracy of the results, with reductions of up to 28% being achieved.

2.2.3 Modelling of metallurgy during laser forming

Accurate modelling of the metallurgy of a component during transient thermal cycles in LF has the potential to give the experimentalist a better idea of the suitability of either the process parameter combinations used or the LF process itself for the shaping of specific components. Whilst process parameters can be chosen which avoid excessive heating, undesirable microstructural transformations may result from a combination of peak temperature, time at peak temperature and subsequent cooling rate (*e.g.* martensitic transformation upon cooling). Such microstructures could adversely affect the ductility of the substrate during LF by increasing the flow stress, making it more difficult to deform [19,74].

Fan *et al.* [79] investigated the effect of phase transformations on the mechanical behaviour of 80 x 40 x 0.89 mm AISI 1010 steel components during the single pass laser forming process. Two process parameters sets were used as part of the investigation; 400 W average power and 25 mm/s traverse speed as well as 800 W average power and 50 mm/s traverse speed. It should be noted that both parameters sets had the same line energy ($LE = P/v_0$). The investigation focussed on analytical modelling of the potential for martensite formation as a result of the high cooling rates associated with the LF process. Therefore, the key phase transformations considered were the ferrite to austenite ($\alpha_{fe} \rightarrow \gamma$) transformation during laser heating and the diffusionless displacive austenite to martensite transformation on cooling.

The $\alpha_{fe} \rightarrow \gamma$ transformation involves the nucleation of γ phase from the α_{fe} matrix and growth of the γ phase by diffusion. As discussed in Section 1.3.1, this type of phase transformation

can be modelled using the Johnson-Mehl-Avrami (JMA) equation. Fan *et al.* employed a version of the JMA equation modified for non-isothermal processes:

$$f(t) = 1 - \exp\left[-(kt)^n\right] = 1 - \exp\left[-\left\{\sum_{i=1}^n k\Delta t_i\right\}^n\right] \quad (26)$$

where f is the volume fraction of austenite and k is the rate factor, related to both nucleation and growth and calculated by the Arrhenius equation. The JMA time exponent n is a temperature independent constant whose value is determined by the nucleation and growth mechanism. The modified JMA equation was used to predict the volume fraction of γ transformed during laser heating, utilizing time and temperature data obtained from a three-dimensional thermal model of the LF process, modelled using the FE software package ABAQUS.

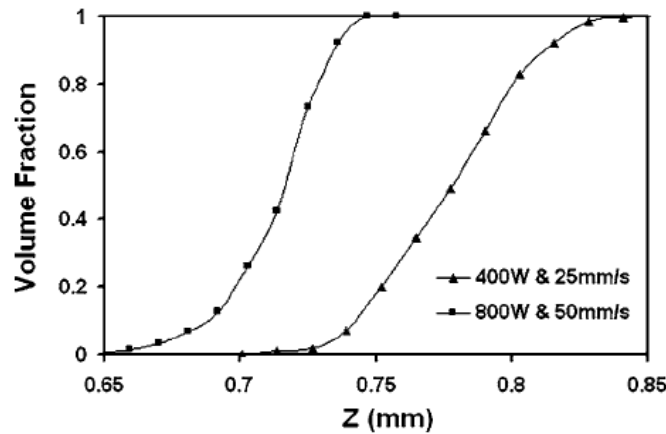


Figure 13 – Predicted volume fraction of transformed austenite with increasing proximity to the surface along the irradiation path (80x40x0.89 mm AISI 1010 mild steel) [79].

The decomposition of transformed austenite to martensite during cooling was predicted using Bhadeshia's phase transformation model [80]. Initially applied to modelling of the welding process, Bhadeshia's model could be used to quantitatively describe the composition of the HAZ in terms of volume fractions of ferrite, pearlite, bainite and martensite. Due to the high cooling rates associated with the LF process, martensite was considered to be the dominant phase after processing. The volume fraction of martensite $V_{\alpha'}$ was calculated by:

$$V_{\alpha'} = (1 - V_{parent}) [1 - \exp\{-0.001(M_s - T)\}] \quad (27)$$

where V_{parent} is the volume fraction of the parent phase and M_s is the martensite start temperature. The calculated martensite distribution after single pass laser forming is shown in Figure 14.

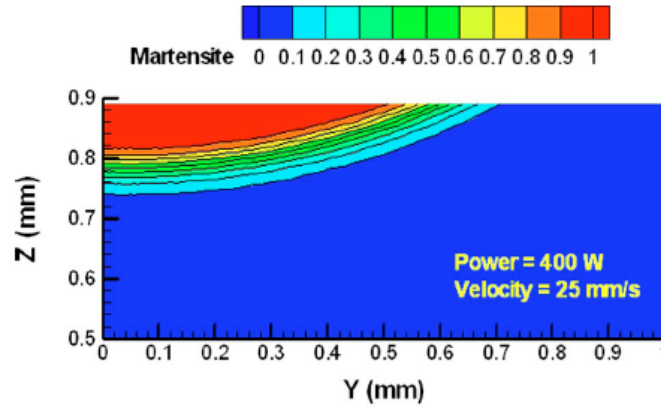


Figure 14 - Predicted volume fraction of martensite after cooling in the half cross-section of the HAZ at the centre of the component (80x40x0.89 mm AISI 1010 mild steel) [80].

The calculated phase distribution after processing was validated by experimental observations using scanning electron microscopy. Near the surface of the component, martensite was the predominant phase. With increasing distance from the surface a mixture of martensite and ferrite was observed. Towards the bottom of the HAZ the main phase was ferrite. The work revealed a high propensity for martensite formation in LF for the parameters used, attributed to the peak temperature reached and high cooling rates simulated.

Cheng *et al.* [74] used a thermal-mechanical FE simulation of the LF process, also modelled using ABAQUS and directly coupled to the JMA equation to ascertain the magnitude of influence microstructural transformation has on flow stress during LF. As in the work by Fan *et al.* two process parameters sets were used as part of the investigation; 400 W average power and 25 mm/s traverse speed as well as 800 W average power and 50 mm/s traverse speed. FE simulations of multiple scan LF were conducted both with and without considering the effect of phase transformation on flow stress and validated against empirical results, as shown in Figure 15.

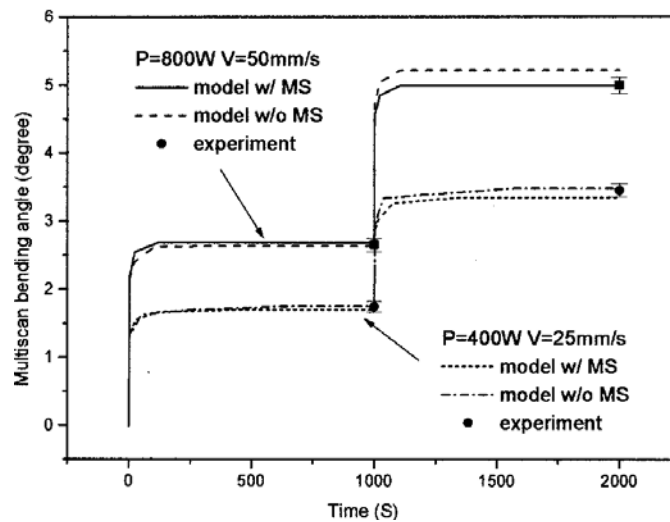


Figure 15 - Comparison of numerical bending angle history with and without microstructure consideration (MS) with experimental measurements in multi-scan laser forming (80x80x0.89 mm AISI 1010 mild steel) [74].

It was found that there was a better agreement between numerical and experimental results when the FE simulations considered the effect of microstructural change on the flow stress of the substrate. This was attributed to an underestimation of the flow stress for the model without microstructure consideration, and thus an overestimation of the bend angle. It was concluded that the dominant effect of microstructural change during LF was hardening for the process parameters investigated and thus an increase in flow stress. This was consistent with experimental and numerical observations regarding the yield stress of the material, which was found to increase as a result of grain refinement and phase transformation.

It was also observed that the discrepancy between the numerical predictions for bend angle shown in Figure 15 was larger for 800 W average power and 50 mm/s traverse than for 400 W average power and 25 mm/s traverse speed. This was attributed to the higher peak temperature and cooling rate simulated for the former parameter set, resulting in a larger predicted volume fraction of martensite, increasing the hardening effect and therefore the flow stress.

2.2.4 Laser tube bending

Hao [81] developed a thermal-mechanical FE model in ADINA of the LF of circular section mild steel tubes, 100 mm in length with an outer diameter of 20 mm and a wall thickness of 1

mm. Process parameters were chosen which induced in plane shortening on a portion of the outer surface of the tube, resulting in an axial bend towards the beam. Fluctuations in stress and strain in the axial direction were simulated and used to rationalize an experimental hypothesis that selective in plane-shrinkage caused the tube to bend due to differences in length between the top and bottom surface, not too far removed from the principle of the TGM. It was concluded that thermal expansion in the irradiated area during laser heating was constrained by the bulk of the substrate causing it to convert to plastic compressive strain, thereby causing in-plane shortening on the top surface of the tube and producing out-of-plane bending towards the beam.

Hsieh [82] used FE models to investigate the axial bending of circular section AISI 304 stainless steel tubes, 100 mm in length with an outer diameter of 8 mm and a wall thickness of 0.5 mm. A linearly coupled thermal-mechanical FE simulation was developed in ABAQUS, employing a Gaussian intensity distributed beam and full range of temperature dependent properties with the exception of Poisson's ratio, which was kept constant at 0.3.

Experimental validation was conducted using a CW CO₂ laser operating at 100 to 200 W. The transient deformation was monitored using a laser based displacement analysis technique. The single-scan strategy employed was circumferential at the centre of the tube. Whilst numerical results were in good agreement with experimentally determined displacements, residual displacement was only achieved in the lateral direction (which was undesired). Transient analysis of the axial displacement revealed that the tube did bend towards the beam during heating but receded upon cooling due to lateral shrinkage of the tube.

In a follow up publication, Hsieh [83] addressed the issue of non-residual axial displacement by applying a pre-load force to the end of the tube, as depicted in Figure 16. The pre-load enhanced compressive stresses in the irradiated region during heating, which in turn enhanced the thermal shrinkage of this region during cooling and resulted in increased out-of-plane deformation towards the beam.

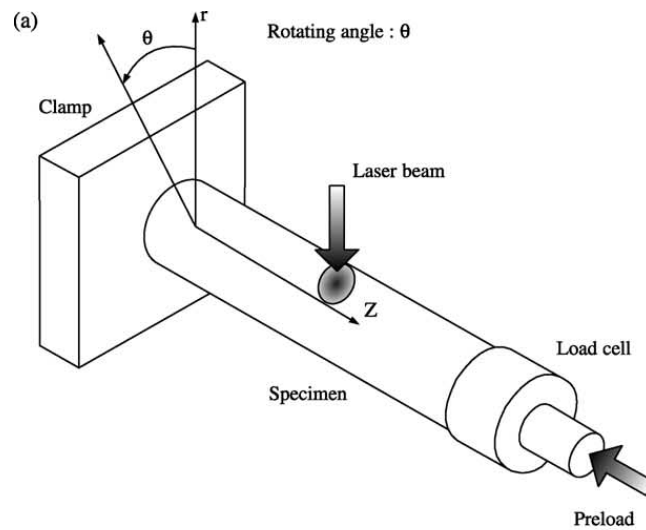


Figure 16 – Diagram of the experimental set-up for the laser tube forming investigation with pre-loading [83].

A similar numerical investigation into the effect of pre-loads had previously been conducted by Yanjin [84], in this instance for the LF of flat sheet metals, as depicted in Figure 17.

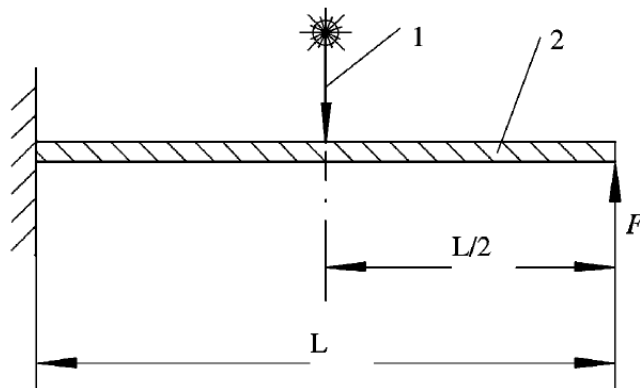


Figure 17 – Schematic diagram of the loading model: (1) laser beam; (2) sheet metal; F is the pre-loading; L the length of sheet metal [84].

Pre-loads oriented towards the beam were found to reduce the plastic compressive forces acting on the bottom surface of the sheet in the irradiated region for TGM process parameters. Simulation results suggested that bending in the desired direction (either towards or away from the beam) could be achieved for any process parameter regime (that is, TGM, UM, BM) providing the direction and magnitude of pre-load force was suitable.

In the investigation by Hsieh *et al.*, the pre-load was varied between 100 and 400 N, the application of which yielding bend angles of up to 0.11 milliradians. Also monitored was the effect of pre-loading on the variation in thickness of the tube around the irradiation path. It was found that the variation in thickness was increased under pre-loading, due to the conservation in volume attributed with the large bend angles achieved.

Safdar [85] studied the axial bending of circular section AISI 304L stainless steel tubes, 100 mm in length with an outer diameter of 14 mm and a wall thickness of 1 mm. Numerical and experimental investigations were carried out, with experimentally determined temperature and bend angle data used to validate the simulations.

Axial bending of up to 0.34° was achieved with undesirable lateral bending present in the same order of magnitude as in-plane shortening (0.06° , 0.05 mm displacement). Also, the effect of scan strategy on bend angle and the asymmetry of the process was investigated, which is of particular relevance to the work presented in Chapter 5 of this thesis.

It was found that scanning in alternate directions across the circumference of the tube at its half way point reduced the undesired lateral deformation considerably when compared to circumferential scanning in the same direction each time. This was attributed to alternating of the lateral bending for each scan. Also noted was the increase in bend angle of up to an order of magnitude for axial scanning, in which the beam is traversed along the length of the tube.

2.2.5 Non-conventional intensity distributions

Invariably, modelling of laser heating is performed using beams with uniformly characteristic intensity profiles (Gaussian, top hat, annular, *etc*). However in reality, under all but the most ideal of conditions, a beams intensity profile undergoes aberrations for a variety of reasons. These aberrations can result from the atmosphere, plasma effects close to the interaction zone and damaged optics. Particularly in the case of propagation aberrations, the beam is not stationary but will wander with time.

Griffiths [86] proposed a method for the implementation of real beam geometries obtained by laser beam analysis (LBA) in FE numerical simulations created in COMSOL Multiphysics. By converting LBA images into greyscale intensity maps, stationary temporally variant beams could be implemented in simulations of laser heating, although traversing beams

applied were non-temporally variant. The effect of non-temporally variant traversing beams on the laser surface hardening and curing of silver particulate inks for the direct writing of conductive tracks was investigated, as depicted in Figure 18.

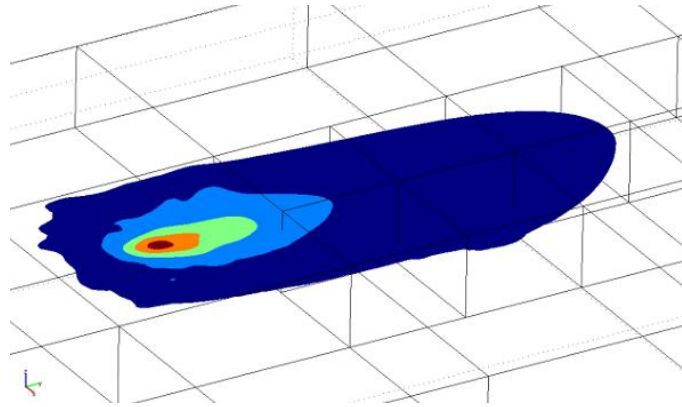


Figure 18 – Heating isotherms resulting from application of traversing real beam geometry, implemented in an FE simulation of the laser heating process [86].

In a follow-up publication [87], Griffiths *et al.* applied traversing temporally variant beams obtained by the LBA method to a parametric FE simulation of the LF process. The study involved a direct comparison between the application of two temporally variant beams, one of which having a defect introduced by an aberration on a reflective optic along the beam path. It was found that the introduction of an aberration required an increase in the laser power to compensate for the reduced energy density of the beam.

Jamil [36,88-90] studied the effect of laser beam geometry on the buckling of AISI 304 stainless steel sheet metal during LF. Various beam geometries were selected, each with different axial dimensions, as depicted in Figure 19.







CASE	A	B	C	D	E	CIRCULAR
Beam profile	 Width = 25mm Length = 8mm	 Width = 20mm Length = 10mm	 Width=14.14mm Length=14.14mm	 Width = 10mm Length = 20mm	 Width = 8mm Length = 25mm	 Diameter = 16mm
Aspect ratio	3.125	2.0	1.0	0.5	0.32	-

Figure 19 - Beam geometries used in FE simulations [88].

A full thermal-mechanical model of the LF process was developed in ANSYS, with each beam geometry assumed to have a uniform average intensity distribution. A 100 x 50 x 0.9 mm AISI 304 stainless steel sheet was specified, with temperature dependant material properties up to between 1000 and 1500 K. In order to reduce overall simulation times the dwell time was five seconds in the numerical model, with the effect of water cooling of the substrate between irradiations ‘simulated’ by an excessively high convective heat transfer coefficient of 2000 W/m²K.

The results of the simulation were validated by a limited experimental study, conducted using a 1.5 kW diode laser operating at between 808 and 940 nm, with sheet dimensions identical to those used in the FE simulations. The beam, fibre delivered to the workpiece, had a circular geometry with a multi-mode intensity distribution and diameter of 16 mm, broadly analogous to the circular beam geometry depicted in Figure 19 that was used in the simulations. The results of this experimental and numerical study are shown in Figure 20.

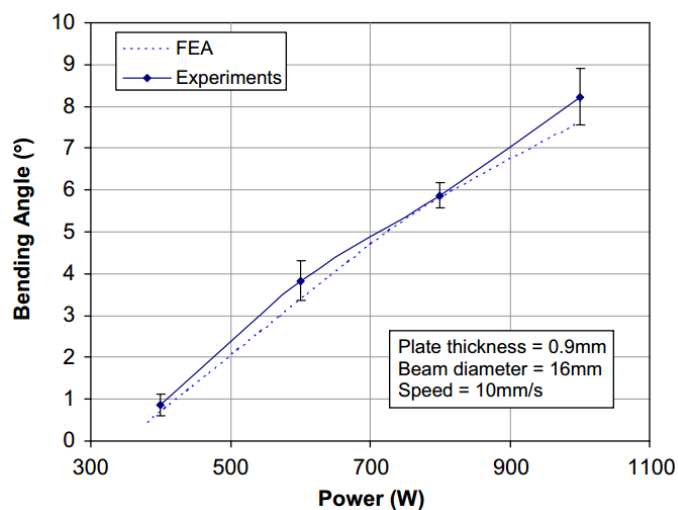


Figure 20 – Simulated and experimental bending angle vs. power for the circular laser beam geometry [90].

Whilst Figure 20 shows good agreement between the numerical and experimental results for bend angle, it is worth noting that there is no mention of whether the substrate was physically water cooled between scans, as in the numerical simulations.

Chapter 3

STATE OF THE ART IN MICRO-SCALE LASER FORMING

Laser micro forming (L μ F) is a process for the precision adjustment, shaping or correction of distortion in micro-scale metallic components through the application of pulsed laser radiation, without the need for permanent dies or tools [9,14,91]. The non-contact nature of the process is also useful in accessing specific micro-components within a device which may be highly sensitive to mechanical force. As such it has potential for widespread application in both the manufacturing and microelectronics industry.

Vollertsen, in an invited presentation at the 2010 LANE conference in Erlangen, Germany [12], summarized the recent advances in micro-scale laser forming, categorizing the various different approaches as the following:

- Non-thermal processes, utilizing nanosecond to femtosecond duration pulses. These processes typically involve the laser ablation of an absorptive or confining layer and the generation of a shockwave, imparting mechanical stresses in the component surface.
- Thermal processes, analogous to the TGM, UM and BM used in macro-scale laser forming applications with appropriately scaled process parameters.

The following subsections detail the state of the art in both thermal and non-thermal L μ F.

3.1 Non-Thermal Processes

As previously mentioned, non-thermal L μ F processes involve laser ablation of the surface of the substrate or an absorptive layer through the use of laser systems with pulses ranging from nanoseconds to femtoseconds in duration. A high pressure plasma is created which expands rapidly, resulting in the generation of a shockwave which propagates through the substrate. If

the pressure of the shockwave creates stresses that exceed the yield strength of the material then this will result in permanent plastic deformation. Commonly referred to as laser shock micro forming (LS μ F), the process has been developed to address the challenges of long thermal relaxation times and excessive thermal loading encountered when scaling conventional thermal LF techniques down to micro-scales.

In 2007, Ocana *et al.* [15] detailed the LS μ F of micro-scale components. Bend angles of up to 3.5° were achieved on $1000 \times 300 \mu\text{m}$ AISI 304 stainless steel actuator style arms with a thickness of $50 \mu\text{m}$. A pulsed Nd:YVO₄ laser operating at 1064 nm wavelength, 10 Hz repetition rate and 9 ns pulse length was used in the investigation, with the micro-scale deformation measured by confocal microscopy. Water was used as a confining layer, restricting the expansion of the laser ablation induced plasma and thereby increasing the pressure of the subsequent shockwave.

The mechanism of deformation was investigated using numerical methods. A one dimensional analytical model of the laser generated shockwave was coupled into a 3D FE model developed in ABAQUS, which subsequently simulated the shockwave propagation throughout the component.

A follow up publication by Ocana *et al.* [92] reported an increase in the magnitude of deformation when shorter wavelengths were used. In this instance, the 1064nm fundamental output wavelength from the Nd:YVO₄ laser was frequency tripled to 355 nm, increasing the coupling of laser radiation into the substrate and therefore increasing the pressure of the subsequent shockwave.

Bechtold *et al.* [93] demonstrated the applicability of femtosecond pulsed laser systems in the LS μ F of micro-scale components. Actuator style arms were fabricated out of copper, stainless steel and silicon as these materials are likely candidates for use in MEMS components. The dimensions of the components, however, were far from MEMS scales at 6 mm in width and 0.5 mm thick.

Out of plane bending away from the beam of up to 0.03° in magnitude was reported using 800 nm wavelength, 100 fs pulse duration and 1 kHz repetition rate. Consideration was given to the surface quality of the irradiated zone after forming as the process involved the ablation

of the substrate itself, leaving approximately 60 μm deep craters along the scan path, as shown in Figure 21.

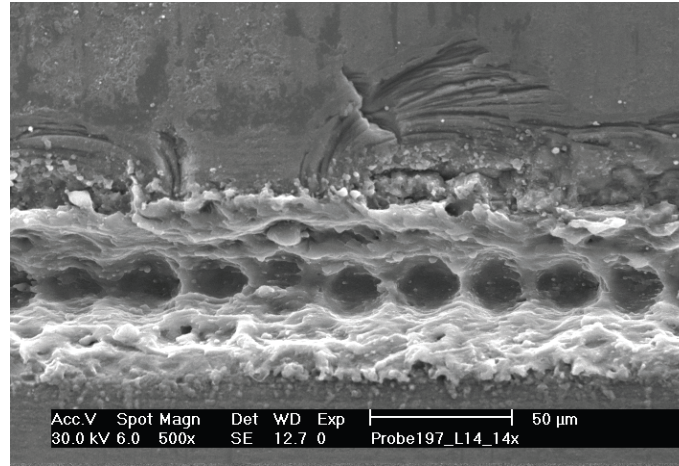


Figure 21 – SEM image of grinding pattern in silicon after 14 irradiations (25 mm/s, 910 mW) [93].

It was observed that the bend angle decreases drastically with decreasing traverse speed. The author attributed this to a localized accumulation of heat on the top surface of the component as a result of the increased laser interaction time, resulting in thermally induced deformation. As this thermal deformation was towards the beam in a TGM style process, it had the effect of negating the negative bending achieved by the non-thermal LS μ F process, reducing the net bending angle. However, no results were presented to support this hypothesis. Specific mention was given to the potential for application of sub-10 ps pulse durations in order to generate localized heating on the surface of micro-scale components, which is particularly pertinent to the contents of Chapter 7 of this thesis.

Edwards *et al.* [94] conducted an empirical study into the mechanism of the LS μ F in order to ascertain the magnitude of influence that thermal aspects of the process had on the amount of deformation. Thermocouples were attached to the underside of 30 x 30 x 0.075 mm AISI 1010 steel coupons, with forming conducted using a Q-switched Nd:YAG operating at 1064 nm wavelength. A maximum temperature rise of just 10 degrees was measured directly beneath the irradiation path during multiple-pass LS μ F, suggesting that thermal aspects have little or no influence on the process.

The LS μ F of aluminium sheet was investigated numerically by Hua [95] using the FE package ANSYS. Analogous experiments were conducted for validation purposes. An Nd:YAG laser operating at 1064 nm with a pulse length of 7 ns was used to form aluminium sheet of 0.4 to 1.75 mm thickness with a confining layer of water. Bend angles of up to 3.2° were reported, forming the component in a concave or convex manner, with thicker section sheets (> 0.9 mm) bending away from the beam. The latter observation was attributed to non-uniform stress distribution throughout the thickness of the sheet during processing, as analyzed by transient simulation.

Laser induced shockwaves have also been used in micro-scale deep-drawing processes, allowing for the forming of smaller features in components when compared to the LS μ F process. Liu *et al.* [96] detailed a laser assisted shock embossing process which utilized the shockwave generated by the laser induced breakdown of an absorptive layer to emboss a 10 μ m thick foil into a mould. This was used to form micro-fluidic channels in the foil.

3.2 Thermal Processes

Hoving *et al.* [97] at Phillips conducted some of the earliest published work on L μ F, demonstrating how lasers could be used to thermally induce out-of-plane and in-plane adjustments in aluminium and stainless steel components.

One of the earliest applications of L μ F was the precise adjustment of magnetic head sliders in hard disk drives, the aim of which was to produce the tightest possible distribution of flying heights during manufacturing. A tight distribution would permit the specification of a lower mean flying height by reducing the risk of contact between the slider and the disk, thereby allowing for ever smaller data bits to be read accurately.

Tam *et al.* [98] at IBM developed one of the first commercially adopted applications of L μ F in laser curvature adjustment technique (LCAT) for the adjustment of magnetic head sliders in hard disk drives. The LCAT process involves inducing thermal stresses by scribing line patterns into the back of a magnetic slider, adjusting its curvature. An in-process monitoring system was integrated to allow for closed loop control of this adjustment to nanometre accuracy.

Another technique for the adjustment of magnetic head sliders in hard disk drives was developed by Singh [99]. Using a frequency doubled Q-switched Nd:YAG laser source with a pulse length of approximately 150 ns, Singh demonstrated the bi-directional adjustment of a stainless steel magnetic slider through control of the repetition rate. Bending away from the beam was conducted at low intensities and a repetition rate of 5 kHz by a process of annealing as a result of conduction limited heating throughout the thickness of the component. Bending towards the beam, however, was conducted at high intensities and with a relatively low repetition rate of 100 Hz. This lower repetition rate prevented the appreciable heating of the component required for annealing, instead inducing highly localized heating, resulting in melt and re-solidification of a micron scale layer on the surface. This melt and re-solidification increases the stress in this surface layer of the component, resulting in out of plane bending towards the beam.

Gartner [100] demonstrated the L μ F of silicon microstructural elements, designed to resemble actuator arms used in functional components. These elements were wet etched using KOH to a thickness of 50 μ m and were clamped at both ends.

Gartner identified two potential classifications of laser micro-adjustment; laser assisted and laser only processes. Laser assisted processes used the laser to heat the component, thereby reducing the flow stress of the material and making it easier to deform using additional tools or dies. Using an Nd:YAG operating in continuous wave mode at its fundamental wavelength (1064 nm) bend angles of up to 22° were achieved by a laser only process.

Wu *et al.* [101] further investigated the laser bending of brittle materials at small scales, focussing on mono-crystalline silicon, boro-silicate glass and Al₂O₃ ceramic. The components were 20 x 20 mm in dimension and 300 μ m thick. An Nd:YAG laser operating at 1064 nm wavelength, 40 Hz repetition rate and with a pulse duration of 0.2 ms was used to achieve bend angles of up to 20° in mono-crystalline silicon and Al₂O₃ ceramic. Additionally, a continuous wave CO₂ laser source was used to induce bends towards and away from the beam in boro-silicate glass through control of the traverse speed, suggesting that TGM and BM regimes operate at this scale, see Figure 22.

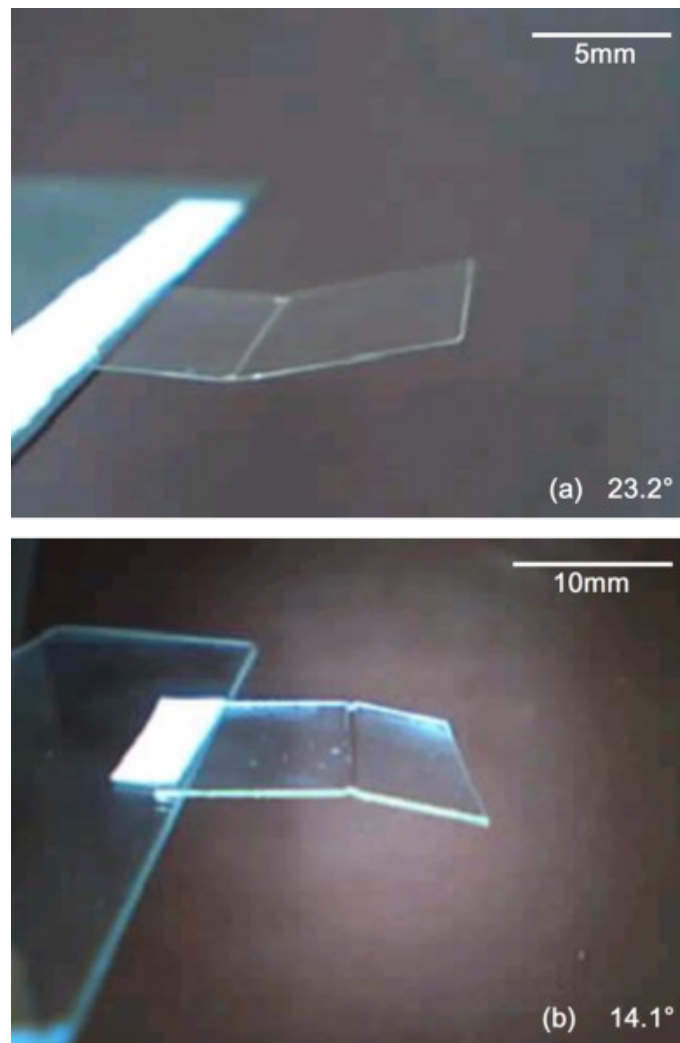


Figure 22 – Photograph of laser formed boro-silicate glass a) towards and b) away from the beam [101].

Shen [102-104] produced numerous experimental and numerical studies on the mechanism of L μ F in stainless steel bridge-style actuator arms, as depicted in Figure 23.

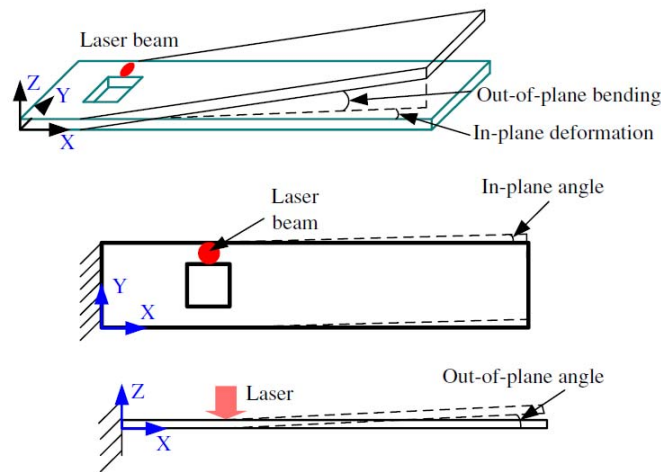


Figure 23 - Schematic diagram of laser micro-adjustment of a bridge-style actuator [104].

Using a 200 W fibre laser system operating at 1064 nm, out of plane bending of up to 0.28° was achieved experimentally. FE simulations of the process were used to analyse the deformation behaviour at constant peak temperature and laser power as well as the effect of heating position were conducted in ANSYS and showed both good qualitative and excellent quantitative agreement (± 3 micro degrees) with the experimental results.

Two actuator sizes were investigated; 30 x 6 mm and 60 x 12 mm. Additionally the effect of component thickness on the mechanism of forming was investigated by varying the thickness between 100 and 1000 μm .

Of particular relevance to the work in Chapter 7 of this thesis was the observation that the nature of bending (that is, in plane or out of plane) was dependent on sheet thickness, with out of plane TGM style mechanisms operating when the sheet thickness was greater than 200 μm , highlighting the limiting scaling effect for the TGM due to excessive thermal loading when using CW heat sources.

Liu *et al.* [96] investigated the thermal forming of 10 x 5 x 0.1 mm AISI 304 stainless steel sheet using a continuous wave CO₂ laser system operating at 10.6 μm wavelength, originally designed for marking applications. Specific emphasis was placed on the effect of varying beam diameter and laser power on the resulting bend angle.

The samples were annealed to remove any residual stresses and edge clamped in a cantilever arrangement beneath the beam. Negative bend angles of up to 10° were achieved, with deformation measured by CCD camera. It was reported that, through variation in process parameters, forming by the TGM was possible. Although a series of combinations of laser power, traverse speed and spot size were identified as being able to repeatedly produce bending towards the beam, it was necessary to induce a pre bend in conjunction with these. This suggests that the mechanism was in fact the BM with a mechanically induced pre-disposition for bending towards the beam.

It was also observed that large heat affected zones (HAZ) were evident for process parameter combinations which yielded large bend angles. In addition, the effect of heat accumulation at the leaving edge of the sheet, resulting in a larger HAZ, was also noted. This has been observed in macro-scale thermal forming experiments, as detailed in Section 5.3.2.

In a follow-up publication by Yanjin and Liu [105], the effect of laser polarization on the absorptivity of $10.6\ \mu\text{m}$ radiation in the same micro-scale components was investigated. The variation in reflectivity for AISI 304 stainless steel for s and p linearly polarized light is shown in Figure 24.

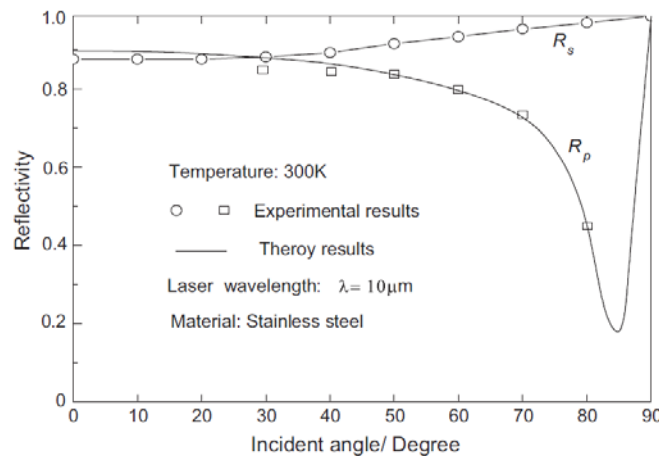


Figure 24 - Variation of the reflectivity of the polarized light with different incident angles [105].

The samples were edge clamped in a cantilever arrangement that could be adjusted to varying angles to alter the incident angle of the beam. For a single irradiation, positive bend angles of

up to 8° were achieved with the angle of incidence varied between 60° and 80° . It was found that, with an incident angle of 60° , 30° bend angles were possible in multi-pass forming, as opposed to just 4° when the incident angle was perpendicular to the sheet. It was noted that, by altering the incident angle, the beam impingent on the sheet became increasingly elliptical, as observed and investigated in Section 5.3.5 of this thesis.

Chapter 4

ANALYTICAL AND NUMERICAL MODEL DEVELOPMENT

In Chapters 1 to 3, the theoretical background of laser forming was introduced along with a summary of recent developments and techniques in modelling of the process. In this Chapter, the theory behind and application of the various analytical techniques and numerical methods used to model the LF process in this thesis are discussed in detail.

The following is a list of the models used to simulate the various aspects of the LF process presented in this thesis:

- (i) A full thermal-mechanical model of the LF process, solved using the finite element (FE) method implemented using COMSOL Multiphysics [106].
- (ii) A one dimensional model of solid-state carbon diffusion into the substrate surface from the absorptive graphite coating during laser heating, solved using the finite difference (FD) method implemented using MATLAB [107].
- (iii) A model of the ferrite to austenite phase transformation during laser heating solved analytically using MATLAB.

The following subsections detail the theoretical development of these models.

4.1 Finite Element Thermal-Mechanical Model Development

The basic principle of the FE method is to partition complex domains into smaller sub-domains, known as finite elements. Connected together by nodes, these elements constitute building blocks from which the parent domain, or mesh, is constructed. Figure 25 depicts the linear, planar or solid form which these elements take in 1D, 2D or 3D systems respectively.

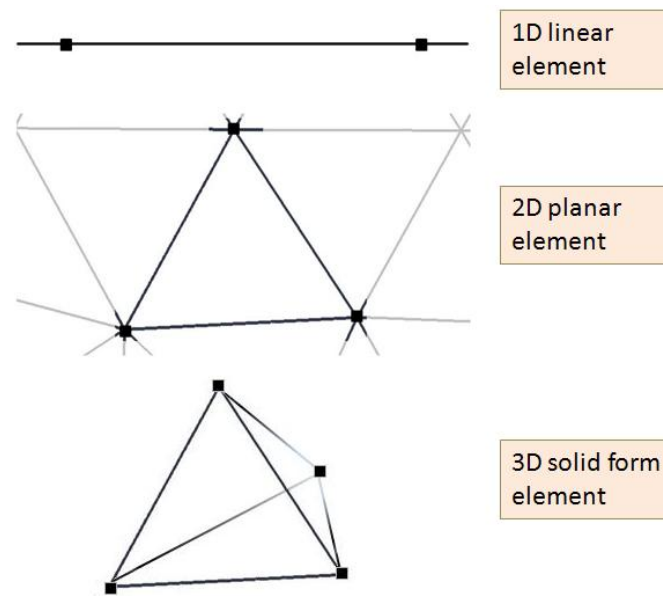


Figure 25 - Linear, triangular and tetrahedral elements as used in 1D, 2D and 3D FE simulations, respectively.

Solutions are obtained for every element in a given domain through formulation of discrete FE equations. In some numerical methods for solving PDEs, the PDE can be discretized directly (that is, written as a linear algebraic equation). A good example of this is the application of the finite difference method to the solution of the one dimensional conduction and diffusion problems detailed in Section 4.2. However, in the FE method the following three components are required for the formulation of discrete equations; the strong form, weak form and approximation functions. The strong form consists of the governing equations and boundary conditions and is essential in all numerical methods. The weak form is the strong form restated in an integral form, and is therefore equivalent to the governing equations and boundary conditions. Combination of the weak form with element specific approximation functions yields discrete FE equations. It is this requirement for the formulation of a weak solution that distinguishes the FE method from other numerical techniques. This relative complexity, however, allows for the specification of highly complex geometries, essential to the modelling of real world engineering problems.

As the FE method is based on numerical integration, the accuracy of the approximate solution obtained improves as the number of nodes in the mesh increases. Therefore mesh density is an important consideration in FE simulations, with thousands of nodes typically required for

in order to obtain a reasonably accurate solution. It should be noted that the mesh density is often varied across a domain depending on the requirements for accuracy in specific regions. For instance, in simulations of laser processes the mesh density is typically highest along the irradiation path (see Section 5.2.2).

The large number of nodes required for FE simulations necessitates the use of computers for solution the discrete equations for each element. As a result, numerous commercial and open source FE software packages have been developed. This investigation into the mechanism of the LF process was conducted through the use of COMSOL Multiphysics, a general purpose FE software package capable of simulating the effects of various physical phenomena within a single model simultaneously in order to solve complex engineering problems. The multi-physical nature of COMSOL makes it particularly useful in the modelling of real world applications. Using the work presented in this thesis as an example, the strain within a component can be strongly affected by or predominantly dependent upon thermal input, requiring a model which is capable of simultaneously simulating both structural mechanics and heat transfer phenomena.

The programming of models into COMSOL can be achieved either directly through a graphical user interface, as in this thesis, or using script language implemented through MATLAB. Analysis types include stationary and time-dependent, linear and non-linear and eigenfrequency/modal analysis. All simulations presented in this thesis use time-dependent (or ‘transient’) linear analysis.

The following subsections detail the theory behind both the heat transfer and structural mechanics phenomena that form the basis of the thermal-mechanical simulations presented in this thesis. Further details on the FE method as applied in COMSOL Multiphysics can be found in the Users Guide [106].

4.1.1 Heat transfer

The heat transfer module supports the fundamental mechanisms of heat transfer; convective, conductive and radiative. Whilst the basic COMSOL package also supports these mechanisms, an added degree of support is provided by the module, particularly for radiative heat transfer (which is extensively encountered in this particular investigation).

4.1.1.1 Conductive heat flux

The governing equation for conduction in a solid is the Fourier heat equation:

$$\rho C_p \frac{\partial T}{\partial t} = \nabla \cdot (k \nabla T) \quad (28)$$

where ρ is the density (kg/m³), C_p is the specific heat capacity (J/kgK), T is the temperature (K), t is the time (s) and k is the thermal conductivity (W/mK) [108]. The term ∇ is the differential or gradient operator (sometimes referred to as the Nabla operator) for three dimensional Cartesian co-ordinate systems:

$$\nabla = \begin{pmatrix} \frac{\partial}{\partial x} \\ \frac{\partial}{\partial y} \\ \frac{\partial}{\partial z} \end{pmatrix} \quad (29)$$

4.1.1.2 Convective and radiative heat flux at a boundary

The heat flux (q) at a given boundary is governed by Equation (30):

$$-n \cdot q = -n \cdot (-k \nabla T) = q_0 + h(T_{\text{inf}} - T) + \varepsilon \sigma_s (T_{\text{amb}}^4 - T^4) \quad (30)$$

where n is the normal vector of the boundary, h is the heat transfer co-efficient (W/m²K), T_{amb} is the ambient temperature (K), T_{inf} denotes a reference temperature (K), ε is the surface emissivity (1) and σ_s is the Stefan Boltzmann constant (5.67x10⁻⁸ W/m²K⁴).

Each of these terms is discussed in more detail in the following subsections.

4.1.1.2.1 Convection

Equation (31) is used to model the inward flux of heat from a user defined source and the outward, convective flux of heat to the surroundings.

$$-n.q = -n(-k\nabla T) = q_0 + h(T_{inf} - T) \quad (31)$$

where h is the heat transfer co-efficient ($\text{W/m}^2\text{K}$) and T_{inf} denotes a reference temperature (K), considered to be equivalent to the ambient temperature in all simulations presented in this thesis.

For thin section materials, the substrate can be considered as a barrier between the laminar flow of fluid on either side of it, as in a heat exchanger. Therefore the value of h for natural external laminar flow can be considered equivalent to the overall heat transfer co-efficient, Q , as determined by:

$$\frac{1}{UA} = \frac{1}{h_1 A} + \frac{s_0}{k} + \frac{1}{h_2 A} \quad (32)$$

where h_1 and h_2 are the heat transfer co-efficient of two fluids either side of a conductive and convective barrier, s_0 and k are the thickness (m) and thermal conductivity of this barrier respectively and A is the contact area (m). This can be rearranged to Equation (33) to give a value for U in free convection from a flat sheet:

$$U = \frac{1}{\frac{2}{h_f} + \frac{s_0}{k}} \quad (33)$$

where h_f is the heat transfer co-efficient of the fluid, which in the case of LF is typically air.

4.1.1.2.2 Radiation

Another mechanism of heat transfer considered in the model is radiative heat transfer at a boundary, in which the outer surface of the substrate exhibits radiative heat transfer. Equation (34), the Stefan Boltzmann law, describes this irradiation in terms of total energy radiated (W/m^2) or radiosity, J , for ideal black bodies:

$$J = \sigma_s T^4 \quad (34)$$

where σ_s is the Stefan Boltzmann constant. Equation (34) makes two simple assumptions. The first is that the ambient temperature remains constant at the user defined value (298.15 K). The second is that the ambient surroundings are entirely transparent and the substrate

absorbs all electromagnetic radiation incident upon it (that is, their transmissivity and absorptivity are equal to one). The relationship between transmissivity, absorptivity and reflectivity is described by Equation (35).

$$reflectivity = 1 - (transmissivity + absorptivity) \quad (35)$$

In order to accurately model radiative heat transfer at a boundary both the net inward radiation (G) and net outward radiation (J) must be considered. Both of which are determined by the Stefan Boltzmann law. The radiosity is the sum of both the reflected radiation (ρG) and the emitted radiation ($\varepsilon\sigma_s T^4$) as depicted in Figure 26.

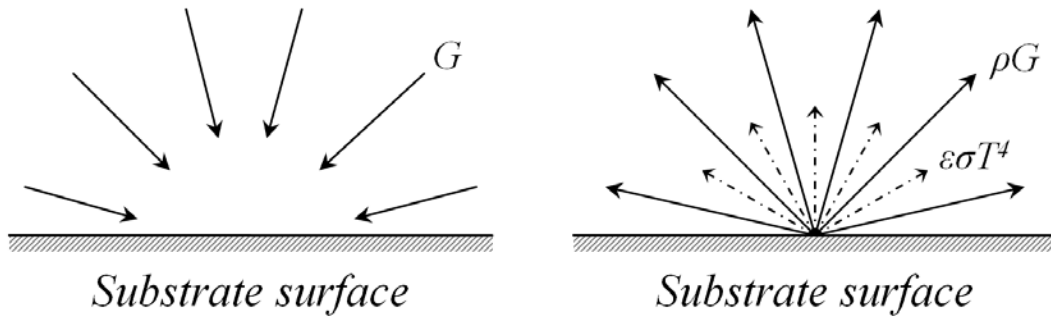


Figure 26 - Inward (left) and outward (right) radiative heat flux at a boundary.

The radiosity can thus be expressed as:

$$J = \rho G + \varepsilon\sigma_s T^4 \quad (36)$$

where ρ is the surface reflectivity and ε is the surface emissivity. The latter is a value between 0 and 1 and acts as a relative measure of a surfaces ability to emit heat by radiation, 0 being entirely reflective and 1 being a perfect black body. Therefore, for given values of G and J , the total net flux of radiation (q) can be described by Equation (37).

$$q = G - J \quad (37)$$

Since absorptivity can be considered equal to emissivity in entirely transparent ambient surroundings, q can be expressed as in Equation (38).

$$q = \varepsilon(G - \sigma_s T^4) \quad (38)$$

Since $G = \varepsilon \sigma_s T_{amb}^4$, Equation (38) can be expressed as Equation (39).

$$q = \varepsilon \sigma_s (T_{amb}^4 - T^4) \quad (39)$$

4.1.2 Structural mechanics

The Thermal Structural Interaction module in COMSOL provides a continuum application mode for the solution of physics phenomena involving solid stress/strain with thermal expansion, achieved through a one-way coupling of the heat transfer and structural mechanics modules. The solution proceeds in a sequential manner where the temperature distribution is calculated prior to performing stress-strain analysis.

The degrees of freedom in the solid stress strain model are the displacements u , v and w in corresponding Cartesian dimensions x , y and z , respectively.

4.1.2.1 The stress-strain relationship

During LF the substrate expands as a result of thermal loading. This thermal strain (ε_{th}), along with initial strain (ε_0) and elastic strain (ε_{el}) induced by deformation combine to give the total strain (ε), as in Equation (40).

$$\varepsilon = \varepsilon_{el} + \varepsilon_{th} + \varepsilon_0 \quad (40)$$

For isotropic materials, a temperature rise results in uniform thermal strain, the magnitude of which depends on the thermal expansion co-efficient of the material, as approximated by:

$$\varepsilon_{th} = \alpha_{th}(T - T_{ref}) \quad (41)$$

where T_{ref} is a reference temperature (K), considered equal to T_{amb} (298.15 K). In order to calculate ε_{th} the normal and shear strain in x , y and z as a result of deformation must be approximated. The normal strain (that is, the strain field perpendicular to the boundary or element face) in x , y and z and its relationship to the deformation in u , v and w is described in Equations (42) to (44):

$$\varepsilon_x = \frac{\partial u}{\partial x} \quad (42)$$

$$\varepsilon_y = \frac{\partial v}{\partial y} \quad (43)$$

$$\varepsilon_z = \frac{\partial w}{\partial z} \quad (44)$$

whereas the shear strain (that is, the strain field along a boundary or element face) in x , y and z and its relationship to the deformation in u , v and w is described by Equations (45) to (47):

$$\varepsilon_{xy} = \frac{\gamma_{xy}}{2} = \frac{1}{2} \left(\frac{\partial u}{\partial y} + \frac{\partial v}{\partial x} \right) \quad (45)$$

$$\varepsilon_{yz} = \frac{\gamma_{yz}}{2} = \frac{1}{2} \left(\frac{\partial v}{\partial z} + \frac{\partial w}{\partial y} \right) \quad (46)$$

$$\varepsilon_{xz} = \frac{\gamma_{xz}}{2} = \frac{1}{2} \left(\frac{\partial u}{\partial z} + \frac{\partial w}{\partial x} \right) \quad (47)$$

where ε_{xy} , ε_{yz} and ε_{xz} represent shear strain in tensor form and γ_{xy} , γ_{yz} and γ_{xz} represent the engineering shear strain. These values can be used to form the symmetric strain tensor for an isotropic material, Equation (48).

$$\boldsymbol{\varepsilon} = \begin{bmatrix} \varepsilon_x & \varepsilon_{xy} & \varepsilon_{xz} \\ \varepsilon_{xy} & \varepsilon_y & \varepsilon_{yz} \\ \varepsilon_{xz} & \varepsilon_{yz} & \varepsilon_z \end{bmatrix} \quad (48)$$

The corresponding symmetric stress tensor ($\boldsymbol{\sigma}$), which defines the stress at a given point, is shown in Equation (49), consisting of three normal stresses (σ_x , σ_y , σ_z) and three shear stresses (τ_{xy} , τ_{yz} , τ_{xz}).

$$\boldsymbol{\sigma} = \begin{bmatrix} \sigma_x & \tau_{xy} & \tau_{xz} \\ \tau_{xy} & \sigma_y & \tau_{yz} \\ \tau_{xz} & \tau_{yz} & \sigma_z \end{bmatrix} \quad (49)$$

For an elastic-plastic material, that is a material which exhibits both elastic and plastic behaviour, the relationship between stress and strain is calculated by:

$$\sigma = D\varepsilon_{el} + \sigma_0 = D(\varepsilon - \varepsilon_p - \varepsilon_{th} - \varepsilon_0) + \sigma_0 \quad (50)$$

where ε , ε_p , ε_{th} , and ε_0 are the total, plastic, thermal and initial strain in column vector form and D is a 6-by-6 elasticity matrix, the composition of which is a function of both Young's modulus (E) and Poisson's ratio (ν), Equation (51).

$$D = \frac{E}{(1+\nu)(1-2\nu)} \begin{bmatrix} 1-\nu & \nu & \nu & 0 & 0 & 0 \\ \nu & 1-\nu & \nu & 0 & 0 & 0 \\ \nu & \nu & 1-\nu & 0 & 0 & 0 \\ 0 & 0 & 0 & \frac{1-2\nu}{2} & 0 & 0 \\ 0 & 0 & 0 & 0 & \frac{1-2\nu}{2} & 0 \\ 0 & 0 & 0 & 0 & 0 & \frac{1-2\nu}{2} \end{bmatrix} \quad (51)$$

The stress-strain relationship in Equation (50) can therefore be expressed in matrix form as Equation (52).

$$\begin{bmatrix} \sigma_x \\ \sigma_y \\ \sigma_z \\ \sigma_{yz} \\ \sigma_{xz} \\ \sigma_{xy} \end{bmatrix} = \frac{E}{(1+\nu)(1-2\nu)} \begin{bmatrix} 1-\nu & \nu & \nu & 0 & 0 & 0 \\ \nu & 1-\nu & \nu & 0 & 0 & 0 \\ \nu & \nu & 1-\nu & 0 & 0 & 0 \\ 0 & 0 & 0 & \frac{1-2\nu}{2} & 0 & 0 \\ 0 & 0 & 0 & 0 & \frac{1-2\nu}{2} & 0 \\ 0 & 0 & 0 & 0 & 0 & \frac{1-2\nu}{2} \end{bmatrix} \begin{bmatrix} \varepsilon_x \\ \varepsilon_y \\ \varepsilon_z \\ 2\varepsilon_{yz} \\ 2\varepsilon_{xz} \\ 2\varepsilon_{xy} \end{bmatrix}_{el} \quad (52)$$

4.1.2.2 Hardening

In all simulations documented in this thesis an elastic, linear hardening stress-strain relationship is specified [109]. Using this method hardening is simulated through specification of three key parameters; the Young's modulus (E), yield stress point (σ_{ys}) and the isotropic tangent modulus (E_{TISO}). Together they form a bi-linear approximation of a stress strain curve, as depicted in Figure 27. A bi-linear stress strain curve was used in order

to conserve computational resources, as it utilizes the same matrix and solver as a linear elastic analysis, changing only the modulus value if the yield stress point is surpassed.

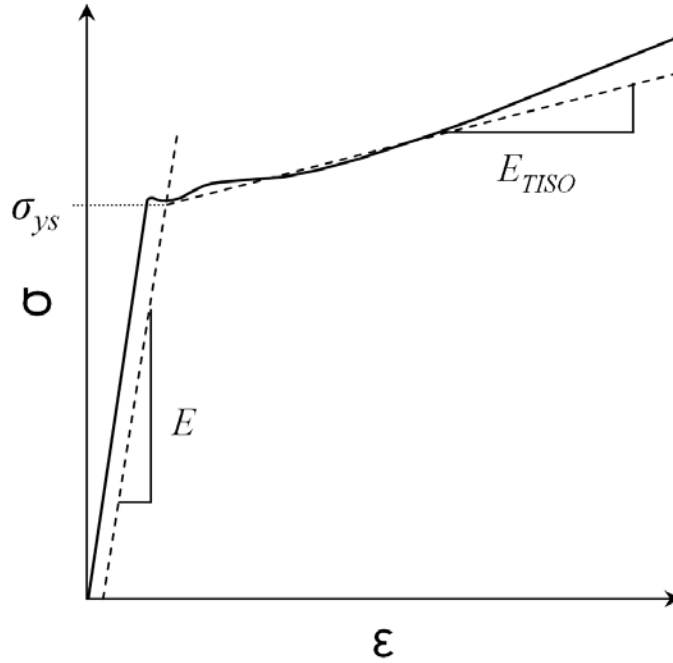


Figure 27 - Idealised stress-strain curve depicting Young's modulus E , yield stress point σ_{ys} and isotropic tangent modulus E_{TISO} .

Von Mises yield criterion is specified in all simulations documented in this thesis; in which yielding occurs if the strain energy *per* unit volume exceeds the strain energy *per* unit volume at the elastic limit. The Young's modulus defines the materials modulus of elasticity and is used to formulate the aforementioned elasticity matrix D when computing the corresponding stress from strain data. Similarly, the isotropic tangent modulus defines the modulus of plastic deformation, with the yield stress point determining the stress at which plastic deformation begins.

4.2 Finite Difference Diffusion Model Development

The finite difference (FD) method was applied to the solid-state diffusion of carbon from an absorptive graphite coating into the surface of the substrate during macro-scale LF [56]. Using transient surface temperature profiles obtained from the aforementioned thermal-mechanical finite element model of the LF process (see Section 4.1) the model was used to

predict depth to which carbon diffused in the substrate during the short duration of laser heating in single pass laser forming.

The model comprised two PDE's; the diffusion equation and heat equation, as detailed in the following subsections. The simulations were coupled so that the temperature distribution as approximated by the heat equation was used to calculate temperature dependant coefficient of diffusion for the diffusion equation.

A one-dimensional geometry was adopted, representing the section thickness (that is, perpendicular to the surface of the component). As carbon can only enter the steel by solid-state diffusion when austenitization occurs, the assumption was made that austenitization is completed prior to the substrate reaching the A_3 temperature (that is, between the A_1 and A_3 critical temperatures) [57].

4.2.1 The heat equation

The FDM can be used to approximate a solution for the one dimensional heat conduction within a domain of length equivalent to the sheet thickness (s_0) of the substrate in the FE simulations, one end of which (or 'boundary') is subject to a transient temperature q_0 , as depicted in Figure 28. The material is AISI 1010 mild steel and the bulk substrate temperature is set to room temperature (298.15 K).

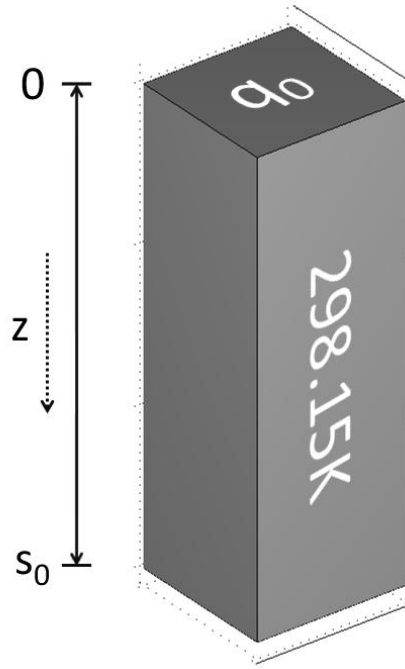


Figure 28 - Idealised depiction of geometry for the 1D heat equation.

The term q_0 has previously been used to refer to the inward heat flux which, in the case of LF, is typically approximated to a laser beam with a Gaussian intensity distribution. However, in the context of the FD models presented in this chapter it represents the transient temperature on the top surface at the centre of the sheet, as calculated by FE simulation. This is subsequently applied as a transient boundary condition in the FD solution of the heat and diffusion equations.

The heat equation, a parabolic PDE, can be used to solve for transient heat conduction in solids, as well as many other engineering problems such as time-dependant diffusion. The heat equation in one dimension can be expressed as:

$$\frac{\partial T}{\partial t} = \alpha \frac{\partial^2 T}{\partial z^2} \quad (53)$$

where α is the thermal diffusivity (m^2/s). The final step in creating a mathematical model is the definition of initial and boundary conditions. The initial conditions define the temperature of the subdomain at $t = 0$, as defined by the function:

$$T(z,0) = T_{amb}(z) \text{ for } 0 \leq z \leq s_0 \quad (54)$$

where T_{amb} is the temperature of steel at room temperature (298.15K). Both boundaries are set to insulating, with the left boundary also set to q_0 in temperature, as described by Equations (55) and (56).

$$T(1,t) = q_0(t) \quad (55)$$

$$T(s_0,t) = T_{amb} \quad (56)$$

In order to solve, the physical domain is partitioned at constant spatial intervals (Δz). In addition, the temporal domain is partitioned at constant time intervals (Δt), as depicted in Figure 29.

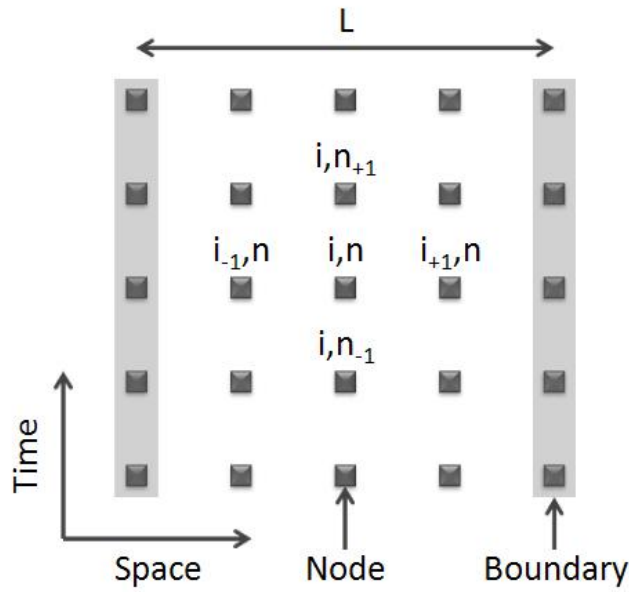


Figure 29 - Spatial and temporal distribution of nodes used for the 1D heat equation.

The central finite difference scheme can be used to solve for temperature at a given time and space within a domain, $T(z,t)$. An explicit method for solving the heat equation on one dimension, the central finite difference scheme is composed of the forward and backwards Euler schemes, Equations (59), (57) and (58), respectively.

$$\left(\frac{d^2T}{dz^2}\right)_{i,n} \approx \lim_{L \rightarrow 0} \frac{T_{i+1}^n - T_i^n}{\Delta z} \quad (57)$$

$$\left(\frac{d^2T}{dz^2}\right)_{i,n} \approx \lim_{L \rightarrow 0} \frac{T_i^n - T_{i-1}^n}{\Delta z} \quad (58)$$

$$\left(\frac{d^2T}{dz^2}\right)_{i,n} \approx \lim_{L \rightarrow 0} \frac{(T_{i+1}^n - 2T_i^n + T_{i-1}^n)}{\Delta z^2} \quad (59)$$

Where i is the spatial location and n is time step number (see Figure 29). The left hand side of the heat equation corresponds to the rate of change of temperature and can be expressed as:

$$\frac{\partial T}{\partial t} \approx \frac{T_i^{n+1} - T_i^n}{t^{n+1} - t^n} = \frac{T_i^{n+1} - T_i^n}{\Delta t} \quad (60)$$

whereas the right hand side of the heat equation is the spatial derivative (also referred to as the residual). This is replaced by the second order central finite difference approximation to give Equation (61).

$$\frac{\partial^2 T}{\partial z^2} = \frac{\partial}{\partial z} \left(\frac{\partial T}{\partial z} \right) \approx \frac{\left(\frac{T_{i+1}^n - T_i^n}{\Delta z} \right) - \left(\frac{T_i^n - T_{i-1}^n}{\Delta z} \right)}{\Delta z} = \frac{(T_{i+1}^n - 2T_i^n + T_{i-1}^n)}{\Delta z^2} \quad (61)$$

Combining Equations (61) and (60) with Equation (53) gives us:

$$\frac{T_i^{n+1} - T_i^n}{\Delta t} = \alpha \frac{T_{i+1}^n - 2T_i^n + T_{i-1}^n}{\Delta z^2} \quad (62)$$

Rearranging to give us known quantities only on the right hand side yields Equation (63).

$$T_i^{n+1} = T_i^n + \alpha \Delta t \frac{T_{i+1}^n - 2T_i^n + T_{i-1}^n}{\Delta z^2} \quad (63)$$

4.2.2 Fick's second law

The same approach as detailed in Section 4.2.1 was applied to the solution of Fick's second law, a parabolic PDE analogous to the heat equation.

$$\frac{\partial C}{\partial t} = D \frac{\partial^2 C}{\partial z^2} \quad (64)$$

Where C is the percentage weight concentration of carbon and D is the diffusion co-efficient (m^2/s) which can be calculated using:

$$D = D_0 e^{-\left(\frac{Q}{RT}\right)} \quad (65)$$

where D_0 is the proportionality constant (m^2/s), Q is the activation energy of diffusion (J/mol), T is the temperature (K) and R is the universal gas constant (8.3 J/mol/K). It should be noted that the diffusion co-efficient D actually varies with carbon content, the effect of which is not considered in this model [110]. The initial conditions define the temperature of the domain at $t = 0$, as defined by the function:

$$C(z,0) = C_0(z) \text{ for } 0 \leq z \leq s_0 \quad (66)$$

where C_0 is the carbon concentration of the steel at the start of the process (%wt). The boundary conditions are described by Equations (67) and (68).

$$C(1,t) = C_s(t) \quad (67)$$

$$C(s_0,t) = C_0 \quad (68)$$

Where C_s is the known carbon concentration on the surface of the substrate (%wt), see Figure 30.

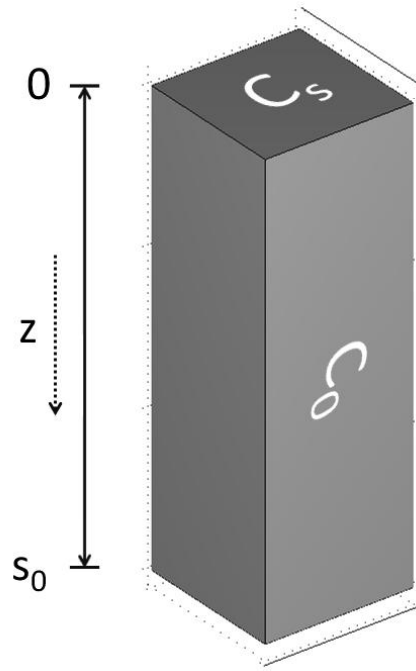


Figure 30 - Idealised depiction of geometry for the 1D solution of Fick's second law

Applying the central finite difference scheme to Fick's second law yields Equation (69).

$$C_i^{n+1} = C_i^n + D\Delta t \frac{C_{i+1}^n - 2C_i^n + C_{i-1}^n}{\Delta z^2} \quad (69)$$

4.2.3 Solving in MATLAB

Equations (62) and (68) were solved sequentially for each iteration of an FDM transient simulation through use of a MATLAB routine (see Appendix C). The solution for the temperature distribution at each time step was used to calculate the temperature dependant value of D for every node in the domain. This one-way coupling is depicted in Figure 31.

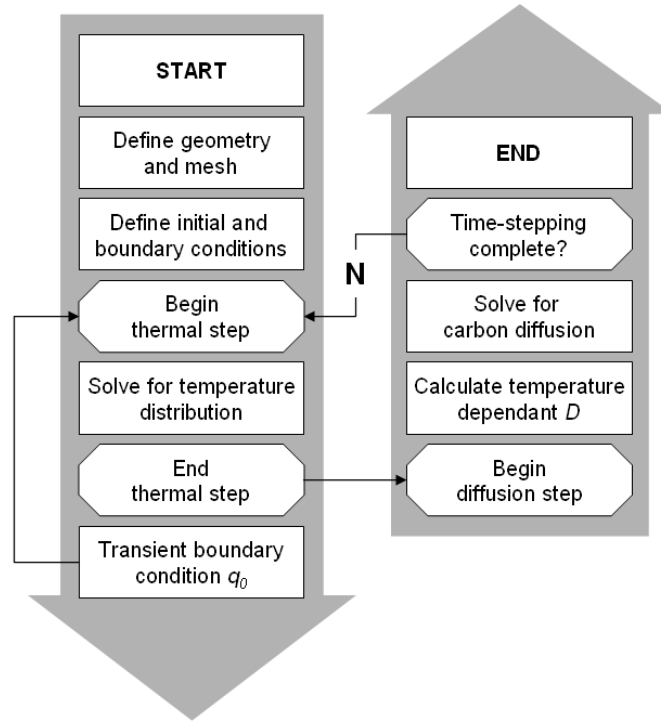


Figure 31 - Flow chart of coupled FD numerical simulation.

4.3 Analytical Phase Transformation Model

An analytical solution was applied to the prediction of phase transformation during the LF process, with a particular emphasis placed on the potential for martensitic transformation.

4.3.1 The ferrite to austenite transformation

Time and temperature data from a single pass FE simulation of laser heating at various traverse speeds was used to model the ferrite to austenite ($\alpha_{\text{fe}} \rightarrow \gamma$) transformation, the kinetics of which is controlled by nucleation and growth mechanisms [68]. It has been shown that, for the $\alpha_{\text{fe}} \rightarrow \gamma$ phase transformation, the volume fraction of transformed product as a function of time and temperature can be described by the kinetic Johnson-Mehl-Avrami (JMA) equation [111]:

$$1 - \alpha_{\text{fe}} = f = \exp - (k(T)t)^n \quad (70)$$

where f is the volume fraction of austenite transformed at time t and $k(T)$ is the temperature dependant rate constant for this transformation. The JMA time exponent n is a temperature

independent constant whose value is determined by the nucleation and growth mechanism. The JMA equation can be applied to non-isothermal heating. A modified version of the JMA equation was used to predict the $\alpha_{\text{Fe}} \rightarrow \gamma$ phase transformation for the non-isothermal conditions predicted by FE simulations [79]:

$$f(t_{(T_m)}) = 1 - \exp \left[- \left\{ \sum_{i=1}^m k(T_i) \Delta t \right\}^n \right] \quad (71)$$

where m is the number of time steps. The rate factor k is calculated by the Arrhenius equation:

$$k(T_i) = k_0 e^{-\left(\frac{Q}{RT_i}\right)} \quad (72)$$

where Q is the activation energy of the $\alpha_{\text{Fe}} \rightarrow \gamma$ transformation, k_0 is the pre-exponential constant and R is the universal gas constant. Equation (71) was solved by an iterative MATLAB routine (see Appendix C). This routine used time/temperature data from COMSOL as the non-isothermal temperature data. The assumption is made that the stress induced by volume change associated with phase transformation is small and therefore negligible. This is considered reasonable on the basis of small predicted transformed volume fractions and good agreement between experimental and numerical results (see Section 5.3). This assumption has also been made in previous numerical investigations into microstructural effects in LF [74,79].

Values for the constants Q , n and k_0 can be determined experimentally by Spatially Resolved X-Ray Diffraction (SRXRD) using synchrotron radiation [112]. However, due to the complexity of this method, these values were sourced from literature (see section 5.3.2).

4.3.2 Martensitic transformation

Whilst the JMA equation can be used to model the ferrite to austenite ($\alpha_{\text{Fe}} \rightarrow \gamma$) transformation upon heating (it can also be used to similar transformations upon cooling, as discussed in Section 4.2.1) it cannot be applied to diffusionless displacive transformations which result from high cooling rates.

As discussed in Section 4.3.1, peak temperature and time at elevated temperature control austenite formation during LF. The formation of non-equilibrium microstructures such as martensite is dependent upon cooling rate. In particular, the likelihood of martensite formation is a key consideration when selecting process parameters in the LF process, as discussed in Section 2.2.3.

As detailed in Section 1.3.2, there is a critical cooling rate (CCR) above which austenite transforms to martensite. Therefore, the volume fraction of martensite present after cooling could be predicted based on the percentage conversion to austenite and the calculated cooling rate. It is assumed that the cooling rate must exceed the CCR at the A_1 temperature for martensite to form. The volume fraction of transformed austenite at this point as predicted by the JMA equation is taken as initial condition for phase transformation upon cooling. The volume fraction of martensite present after cooling was considered to be equal to that of austenite at either the martensite finish temperature (M_f) or the point at which the cooling rate dropped below the critical cooling rate required for the formation of martensite, after which it is considered to be constant.

Chapter 5

FACTORS AFFECTING BEND ANGLE PER PASS IN MACRO SCALE LASER FORMING

In order for LF to fulfil its promise in a manufacturing environment the process must have a high degree of controllability, which can be achieved through a better understanding of its underlying mechanisms. One area of limited understanding is that of the variation in bend angle per pass observed during multi-pass laser forming along a single irradiation track, notably the decrease in bend angle per pass after many irradiations which is common to LF of all metallic substrates. Finite element (FE) modelling can be used to ascertain which of the various factors identified (such as graphite burn-off, geometrical effects, variation in absorption, etc.) contribute towards this phenomenon and subsequently the magnitude of their contribution.

5.1 Introduction

During multiple-pass LF, whilst the bend angle *per* pass is fairly constant initially (typically over the first 15 to 20 passes) there is a fall off in the angle of bending achieved with successive irradiations after this. A number of factors have been identified as contributing to this; strain hardening and section thickening, variation in absorption, thermal effects, and geometrical effects [19]. In turn, each of these factors depend on the complex interrelation of process parameters and substrate thermal-mechanical properties.

In order for laser forming to realize its potential as a fully controlled process in a manufacturing environment an understanding of this variation in bend angle *per* pass is essential. The research presented in this chapter focuses on attaining a higher degree of controllability through numerical and analytical modelling as a means of process development. The development of a full thermal-mechanical simulation of the LF process is

detailed and subsequently utilized both to identify factors contributing the fall-off in bend angle *per* pass and the magnitude of their contribution.

5.2 Experimental Set-up and Model Development

5.2.1 Experimental set-up

An experimental study was conducted on graphite coated 80 x 80 x 1.5 mm normalized AISI 1010 steel coupons using a 1.5 kW CO₂ TEM₀₀ fast axial flow laser (Electrox Ltd.) with a 3-axis CNC beam delivery system (Galil Motion Control Ltd.), custom written control software and operating in CW mode with a wavelength of 10.6µm. The mode structure of the beam was determined from a print of the raw unfocussed beam in perspex, as shown in Figure 32. The beam print was imported into MATLAB for analysis using a laser scanning system (3D Laser Scanner, NextEngine Ltd.). [113]

Element	Content (%)
Carbon, C	0.08-0.13
Iron, Fe	99.18-99.62
Manganese, Mn	0.30-0.60
Phosphorus, P	≤0.04
Sulphur, S	≤0.05

Table 2 – Chemical composition of AISI 1010 carbon steel [113].

The deformation induced was measured between laser passes using a laser range finder (M5, MEL Mikroelektronik GmbH.) with a range of 100 mm. Operating on the principle of triangulation between a laser diode and a photo-sensitive diode, the range finder produced a +/-10 V signal which corresponded to the 100 mm range of deformation, with a stand-off distance of 220 mm.

The M5 laser range finder was used for all measurements detailed in this Chapter with the exception of the empirical study into edge effects (Section 5.3.5), in which the deformation was measured off-line using a more accurate laser range finder (M20, MEL Mikroelektronik

GmbH.), which had a range of 20 mm. The M20 range finder produced a ± 10 V signal which corresponded to the 20 mm range of deformation, with a stand-off distance of 40 mm.

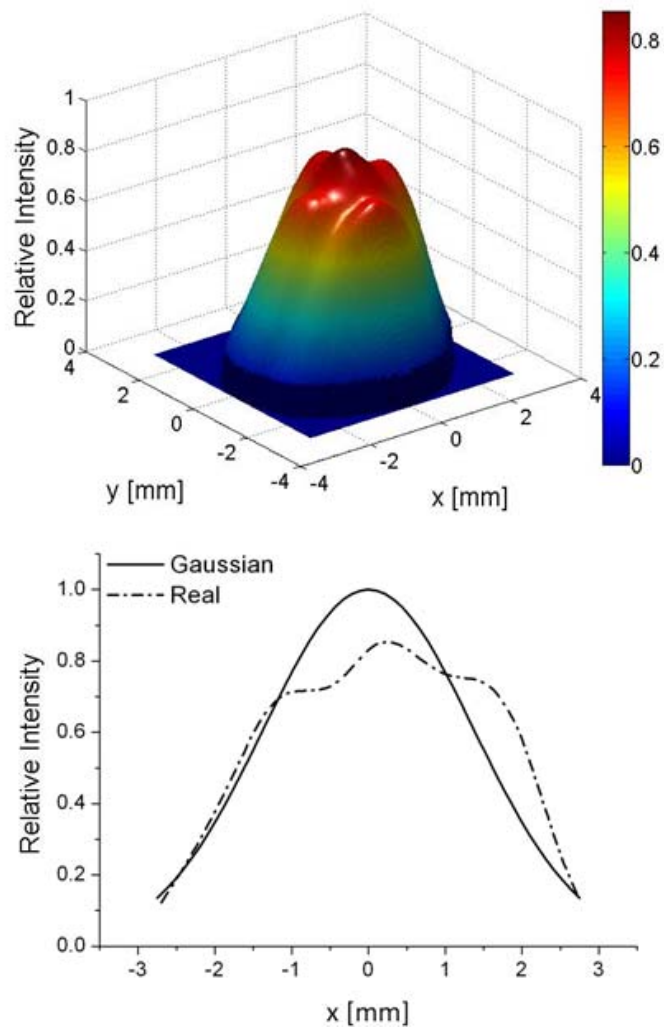


Figure 32 - Electrox intensity distribution as obtained by 3D laser profiling of a perspex beam print (top) and 2D profile through centre of the beam compared with an ideal Gaussian intensity distribution (bottom).

A cantilever clamp arrangement was used for processing, with the coupons being clamped at one edge, as depicted in Figure 33.

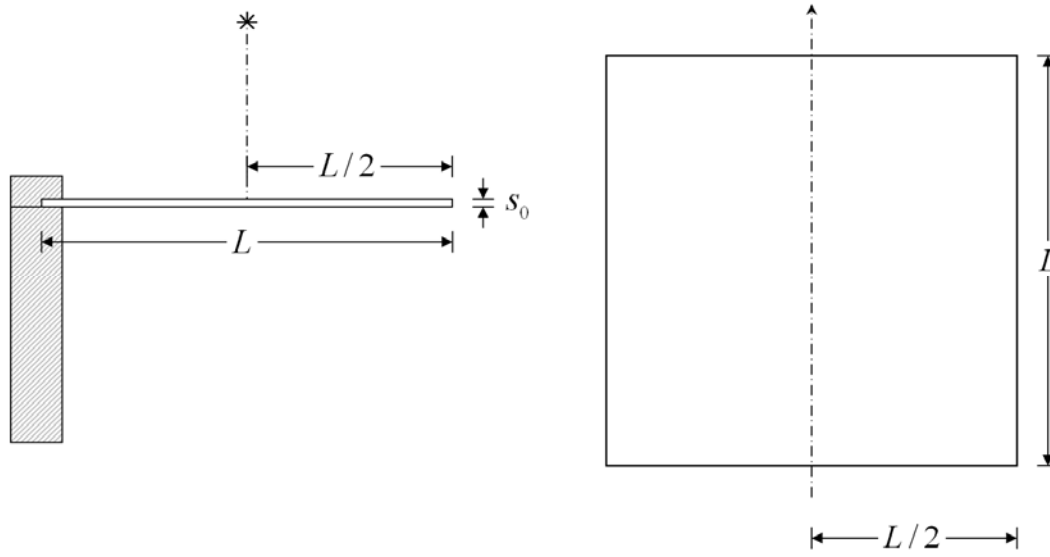


Figure 33 – Schematic diagram of edge clamped cantilever arrangement with component length (L) and sheet thickness (s_0). Dashed-dot lines represent irradiation path and direction.

α_{th}^* [1/K]	C_p^* [J/kg.K]	E^* [Pa]	E_{TISO} [Pa]	h [W/m ² .K]	k^* [W/m.K]	ρ^* [kg/m ³]	σ_{ys}^* [Pa]	ν^* [1]
$1.15e^{-5}$	442.50	$2.14e^{11}$	$1.09e^9$	25	64.55	7850	$3.5e8$	0.2891

Table 3 -AISI 1010 material properties at 298.15K (* denotes properties which are considered temperature dependant in the simulations, see Appendix B for values) [113].

5.2.1.1 Custom software

Custom software was developed using Visual Basic in order to manipulate the CNC workstation. Of particular note was the program created as part of an investigation into edge effects in LF (see Section 5.3.5). This utilized linear interpolation in order to split the irradiation path into four sections, each of which could be assigned a different traverse speed, see Figure 34. This linear interpolation was calculated based on a specified acceleration and deceleration, with an example of the G-code output provided in Appendix C.

During the rest time between passes, the deformation at 8 positions along the edge of the workpiece, spaced at 10 mm intervals, was measured using the laser range finder, the average of which was used to determine the bend angle.

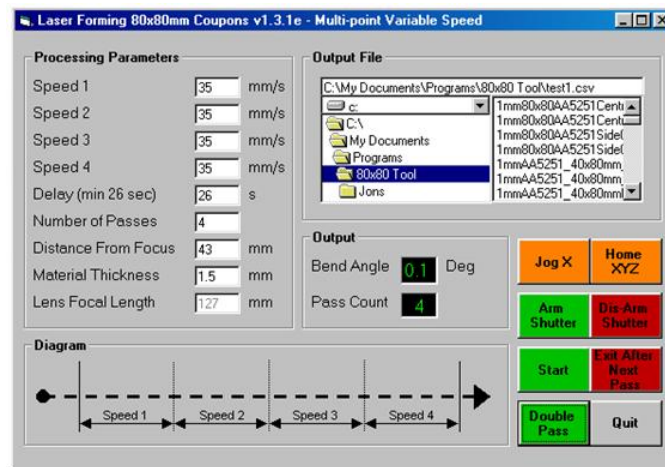


Figure 34 -Screenshot of custom software used in edge effects investigation.

5.2.1.2 Metallurgical study

The centre portion of the steel coupon was sectioned by water cooled mechanical saw and carefully ground in order to assess the metallurgical effects of laser heating during LF. These sections were subsequently mounted in resin and polished to a grain size in the order of microns. After polishing the samples were stored in a dessicator to avoid oxidation.

In order to see the grain structure under a microscope the sections were etched with Nital (1%). The Nital solution was composed of 1 ml nitrous acid (HNO_2) in 100 ml ethanol (99%) [113]. A microscope (Nikon-Epiphot, Nikon Ltd.) with a camera (Nikon Infinity 2, Nikon Ltd) was used to visualize the grain structure. The software used to process the images was Lumenera Infinity Capture (Version 5.0.2, Lumenera Corporation).

A Vickers micro hardness tester with the specification HV 0.1/10 was used to measure the hardness of the sectioned samples. The method involves forcing a diamond pyramid into the surface of the sample, where HV 0.1/10 refers to the force and duration over which it is applied (100 N, 10 s). The mean diameter, $(d_1 + d_2)/2$, of the imprint made can be converted into a Vickers hardness value using Equation (73).

$$HV = \frac{0.1891F}{\frac{d_1 + d_2}{2}} \quad (73)$$

The measurements taken were spaced as far apart as possible within reason so as to avoid inducing strain hardening effects that might affect subsequent measurements. This often meant ‘staggering’ the measurements in a regular pattern to allow for measurements at sufficiently small intervals throughout the materials thickness.

In addition, it is worth noting that measurements at the edges of mounted samples were not possible due to induced deformation, which manifested itself in the form of low Vickers hardness values.

5.2.2 FE model development

To fully understand the thermal and mechanical aspects of the LF process an FE model was developed. A 2005 element thermal-mechanical simulation of the laser forming of 80 x 80 x 1.5 mm AISI 1010 steel, using multiple irradiations, was developed using COMSOL Multiphysics version 3.5a (see Figure 35).

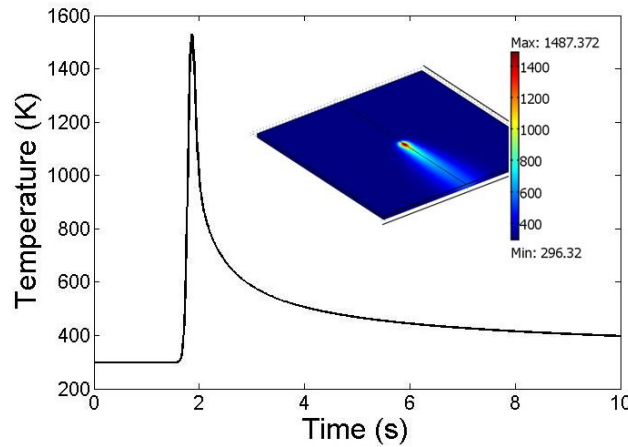


Figure 35 - COMSOL Multiphysics FE model output for the top surface directly on the laser scan line (80 x 80 x 1.5 mm mild steel AISI 1010, 760 W, 5.5 mm beam diameter, 35 mm/s, 80% absorption, edge clamped).

The thermal expansion coefficient (α_{th}), Young's modulus (E), Poisson's ratio (ν), specific heat capacity (C_p), thermal conductivity (k), density (ρ) and yield stress (σ_{ys}) were all

considered temperature dependant and validated against values quoted in literature and experimentation where possible. The incident laser beam was approximated by a Gaussian distributed heat source with an absorption coefficient of 0.8.

All material properties were sourced from the ASM Metals Handbook [113] or COMSOL's built in materials library, with the exception of the isotropic tangent modulus (E_{TISO}), which was obtained *via* experimentation, see Figure 36.

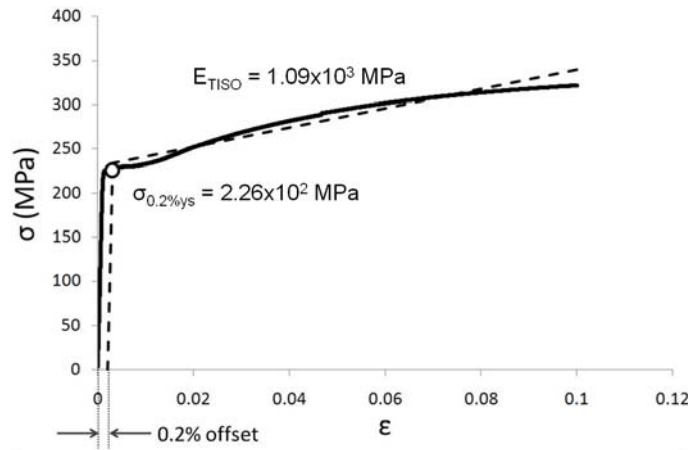


Figure 36 - Experimentally determined stress-strain curve for AISI 1010 mild steel.

In addition to determining the value of E_{TISO} , the experimental stress-strain curve was used to validate the value for the Young's modulus of 2.14×10^{11} MPa obtained from the COMSOL Multiphysics material library, as shown in Figure 37.

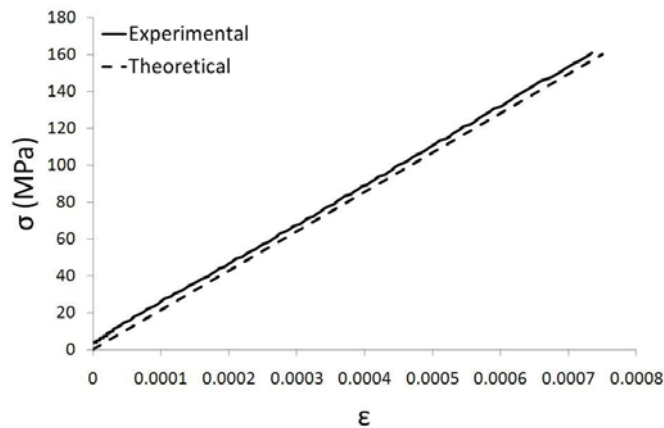


Figure 37 - Experimental and theoretical elastic portion of the stress strain curve (AISI 1010).

The global mesh element size was set to coarse and determined by an in-built algorithm in COMSOL. A suitable maximum element size for use along the irradiation path was determined by convergence study and found to be 0.1 mm. The meshed geometry is depicted in Figure 38.

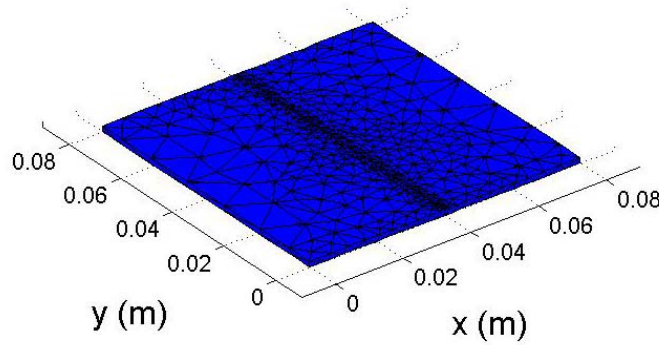


Figure 38 - Meshed geometry used in FE simulations.

5.2.2.1 Modelling the heat source

The spatial distribution of the inward heat flux q_0 is typically considered to be an ideal Gaussian distribution, although other distributions have been applied (see Section 5.3.5). As such the intensity reaches a maxima (I_0) at its centre and an effective minima (ω_0) when the intensity drops to $1/e^2$ (13.5%) of I_0 . The distribution is defined as in Equation (74).

$$I = I_0 e^{-\left(\frac{2 \left(\sqrt{(x-x_0)^2 + (y-y_0)^2} \right)^2}{\omega_0^2} \right)} \quad (74)$$

The relationship between intensity distribution and maximum intensity for a Gaussian beam is described by Equation (75).

$$I = I_0 e^{-\left(\frac{2r^2}{\omega_0^2}\right)} = \frac{2P}{\pi r^2} e^{-\left(\frac{2r^2}{\omega_0^2}\right)} \quad (75)$$

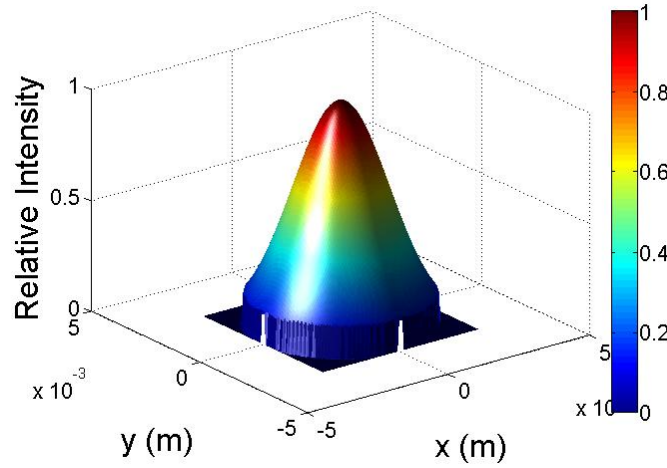


Figure 39 - 3D plot of Gaussian intensity distribution created in MATLAB.

The Gaussian equation (74) was applied in COMSOL using the following expression:

$$q_{laser1} = I_0 e^{-\left(\frac{2r_1^2}{\omega_0^2}\right)} \quad (76)$$

where:

$$r_1 = \sqrt{(x - x_1)^2 + (y - y_1)^2} \quad (77)$$

where x_1 and y_1 are the starting co-ordinates for the beam in x and y respectively. For the case of single line scanning with multiple irradiations, one of these values (in this case x_1) remains constant whilst the other is made time variant by multiplying by dI :

$$d_1 = v_0 t, d_2 = v_0 (t - 60), d_3 = v_0 (t - 120), etc... \quad (78)$$

Multiple IF statements were subsequently used to apply numerous heat sources sequentially at specified times, as in Equation (79).

$$if(t < 60, q_{laser1}, 0), if(t < 120, q_{laser2}, 0), if(t < 180, q_{laser3}, 0), etc... \quad (79)$$

5.2.2.2 Modelling temperature dependant material properties

The aforementioned temperature dependant material properties were applied to the simulations as interpolation functions, as depicted in Figure 40.

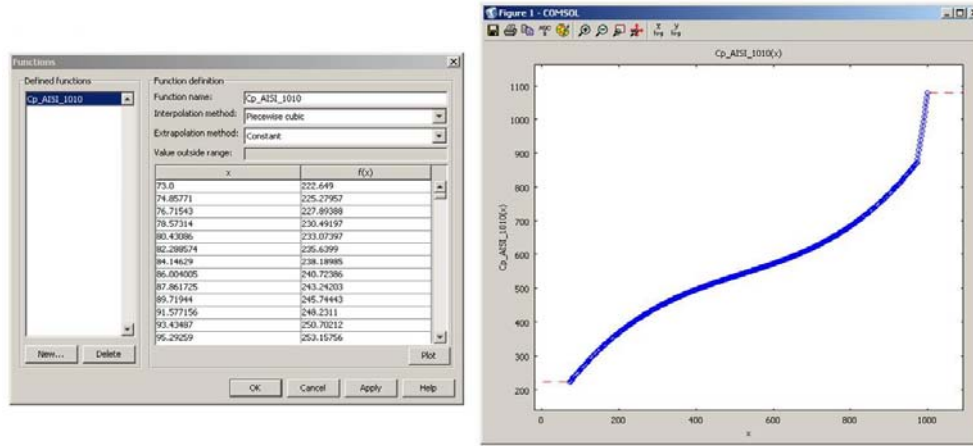


Figure 40 -Screenshot from COMSOL Multiphysics illustrating how interpolation functions can be used to apply temperature dependent material properties.

These functions consisted of a table of temperature values in ascending order with the corresponding material property values. The data could be interpolated to find material properties at non-specified higher temperatures or set to remain constant at the last specified value. Due to the transient nature of the temperature dependant data the interpolation functions were referenced *via* the Scalar Expressions, in which the units of the data were specified:

$$Cp_{scalar} = Cp_{AISI1010}(T[1/K])[J/kg.K] \quad (80)$$

The scalar variable Cp_{scalar} could then be directly referenced in the substrates Subdomain Settings. A full list of parameters considered temperature dependent is given in Appendix B.

5.2.2.3 Solver settings

The solver chosen for the following simulations is the Direct (SPOOLES) linear system solver. The SPOOLES solver is ideal for this investigation as it is able to make use of the

high degree of geometrical symmetry and the parabolic nature of the dominant PDE, the heat equation (27), to conserve computational resources.

Automatic (or ‘free’) time stepping is implemented in the simulations detailed in this chapter. This allows the solver to choose suitable time steps arbitrarily according to transient boundary conditions (that is, the traversing laser beam heat source).

During the approximately 2.5 s *per* pass in which the heat source is applied to the top boundary of the substrate, the time steps are reduced automatically by the solver to a suitable duration in order to resolve the phenomena. During the relatively extensive dwell time of 60s between passes the time steps are vastly increased as the solution reaches a steady state approximation. A maximum time step value can be specified if necessary to ensure that no transient boundary conditions are ‘overstepped’ by excessively large time steps during these intervals.

5.3 Results and Discussion

Numerical and experimental results and discussion on factors which influence the bend angle *per* pass in multi-pass LF are discussed in the following subsections.

5.3.1 Thermal effects

5.3.1.1 Effect of process parameters

With multiple irradiations an associated build up in temperature within the components occurs, which subsequently affects the bend angle *per* pass. Such elevated temperatures can be both beneficial and detrimental to the LF process. Therefore, a dwell time between passes must be used which best suits the specific application. Increased temperatures can reduce the flow stress of the component, making it easier to plastically deform. Conversely, the temperature gradient achievable between the top and bottom surface of the component along the irradiation line can be diminished which would reduce the net bending angle.

The magnitude of the influence that temperature effects have on LF is most apparent during the early stages of the process, in this case within the first six passes. After this point thermal equilibrium between energy input from the laser heat source and conductive, convective and radiative heat transfer during the dwell time between irradiations is established, as shown in

Figure 41. The number of passes prior to reaching this equilibrium is both material and process parameter dependent.

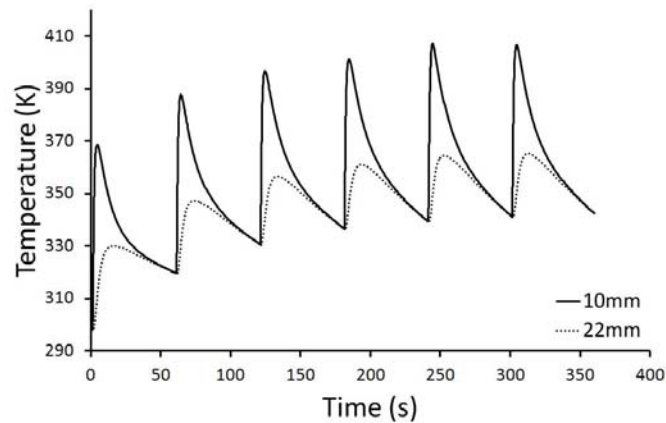


Figure 41 - FE simulation of temperature at 10mm and 22mm from the irradiation path over the first six passes (80 x 80 x 1.5 mm mild steel AISI 1010, 760 W, 5.5 mm beam diameter, 35 mm/s, 80% absorption).

The bend angle *per* pass for both the experiment and simulation over the first six passes reveals an initial increase prior to the fall off associated with the LF process, as shown in Figure 42. This can be attributed to the increase in temperature in the bulk material with increasing number of passes shown in Figure 42. This leads to an increase in peak temperature in the irradiated region with successive passes which, when coupled with the reduced flow stress of the component as a result of elevated temperature, leads to a larger bend angle *per* pass.

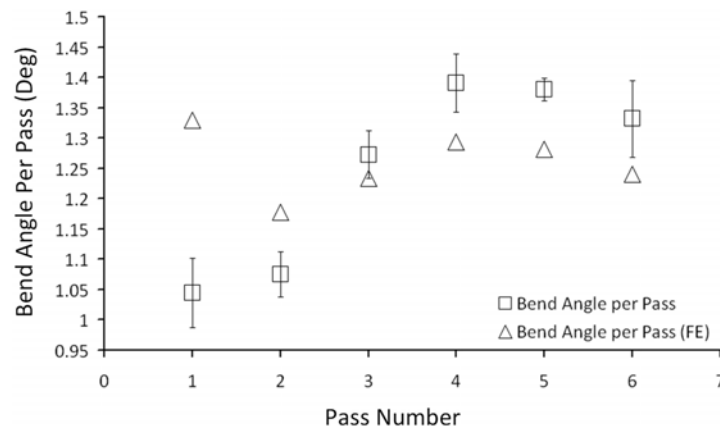


Figure 42 - FE Experimental and simulated bend angle per pass over the first six passes (80 x 80 x 1.5 mm mild steel AISI 1010, 760 W, 5.5 mm beam diameter, 35 mm/s, 80% absorption).

In this instance, the beneficial effects of a build up in temperature appear to last up to the fourth pass before the temperature gradient is adversely affected and the bend angle per pass is reduced.

5.3.1.2 Effect of material property variation

An FE simulation of the first six passes was conducted in which three material thermal properties were varied within $\pm 20\%$ of their initial value. These were the thermal conductivity, specific heat capacity and thermal expansion coefficient, with their effect on the cumulative bend angle after six passes studied (see Figure 43).

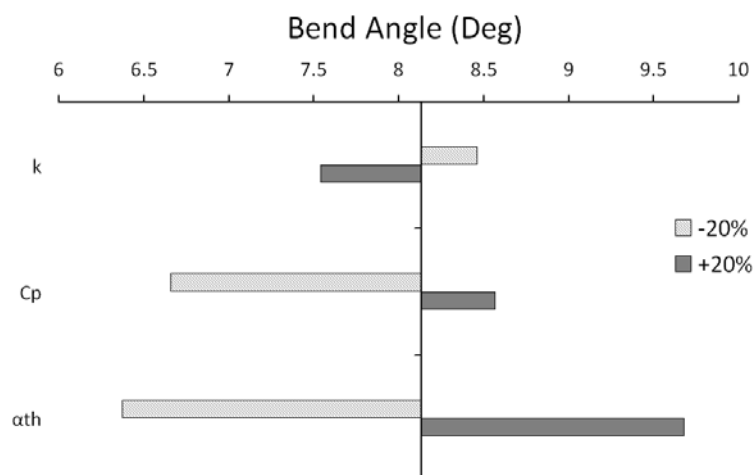


Figure 43 - Effect of varying k , C_p and α_{th} on the cumulative bend angle after six passes (80 x 80 x 1.5 mm mild steel AISI 1010, 760 W, 5.5 mm beam diameter, 35 mm/s, 80% absorption).

From Figure 43 it is clear that the thermal expansion coefficient has the largest influence on bend angle. An increase in thermal expansion subsequently increases the amount of plastic compression in the heated area, resulting in more plastic deformation.

In assessing the effect of varying the values of k and C_p the thermal diffusivity (α) is a useful parameter to consider, Equation (81).

$$\alpha = \frac{k}{\rho C_p} \quad (81)$$

The higher the value of α , the more rapidly a substrate can adjust to changes in temperature and return to thermal equilibrium with its surroundings. Figure 44 depicts the effect on α when k and C_p are varied within +/-20% of their initial value, calculated from Equation (81) using temperature dependant data, presented in Appendix B.

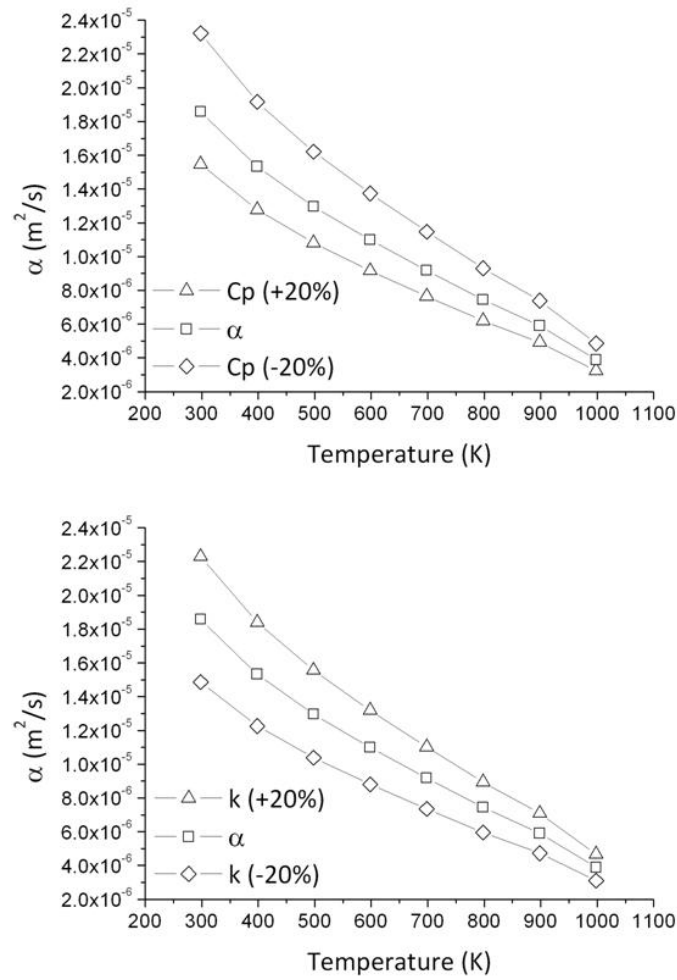


Figure 44 - The effect of varying C_p (top) and k (bottom) on α .

From Figures 43 and 44 it would appear as though in the early stages of the LF process a lower value of α is beneficial to the efficiency of the LF process.

5.3.2 Microstructural effects

Microstructural change due to transient thermal cycles has the potential to be a contributing factor to the fall off in bend angle *per* pass. Whilst process parameters can be chosen which avoid excessive heating, non-ferritic microstructures in the HAZ may result from a combination of peak temperature, time at peak temperature and subsequent cooling rate. Such microstructures could adversely affect the ductility of the substrate by increasing the flow stress, making it more difficult to deform [74,114].

Time and temperature data from a single pass FE simulation of laser heating at various traverse speeds was used to model the ferrite to austenite ($\alpha_{\text{fe}} \rightarrow \gamma$) transformation. The transformation, which involves the nucleation of γ phase from the α_{fe} matrix and subsequent growth of the γ phase by diffusion, can be described by the Johnson-Mehl-Avrami (JMA) equation:

$$f(t_{(T_m)}) = 1 - \exp \left[- \left\{ \sum_{i=1}^m k(T_i) \Delta t \right\}^n \right] \quad (82)$$

where m is the number of time steps and f is the volume fraction of austenite. The JMA time exponent n is a temperature independent constant whose value is determined by the nucleation and growth mechanism. The assumption is made that the stress induced by volume change associated with phase transformation is small and therefore negligible, as discussed in Section 4.3.1. The rate factor, k , is calculated by the Arrhenius equation:

$$k(T_i) = k_0 e^{-\left(\frac{Q}{RT_i}\right)} \quad (83)$$

where Q is the activation energy of the $\alpha_{\text{fe}} \rightarrow \gamma$ transformation, k_0 is the pre-exponential constant and R is the universal gas constant. The values used in both the modified JMA and Arrhenius equations were for AISI 1005 steel and taken from literature [79]. The volume fraction of austenite was considered zero when the temperature was below the lower critical transformation temperature (A_1 , 996.15K).

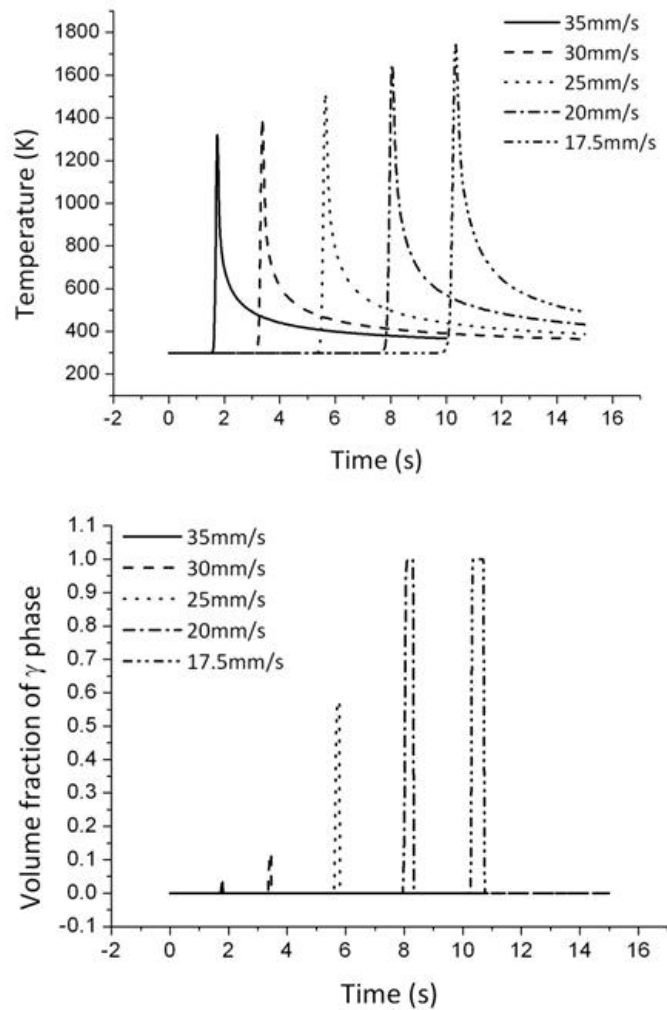


Figure 45 - Single pass FE simulation of peak temperature with different scan speeds (top) and volume fraction of austenite transformation on the top surface at the centre of the sheet (bottom) (80 x 80 x 1.5 mm mild steel AISI 1010, 760 W, 5.5 mm beam diameter, 80% absorption).

From Figure 45 it can be seen that the volume fraction of transformed austenite is related to peak temperature, which itself is process parameter dependent. Some sub-melting combinations of traverse speed and power, such as low speeds and high powers, can result in high volume fractions of austenite and therefore, depending on rate of cooling, martensite. The presence of martensite would increase the hardness of the heat affected zone (HAZ) and can thus be considered detrimental to the LF process; however, for the process parameters used in this investigation ($v_0 = 35$ mm/s, $P = 760$ W, $\omega_0 = 2.75$ mm) only a small volume fraction of austenite (0.02) was predicted.

The volume fraction of martensite can be predicted based on the percentage conversion to austenite and the cooling rate for a given spatial co-ordinate. A critical cooling rate for the martensite formation of 450 K/s was determined from a CCT diagram [54].

A MATLAB routine was developed which predicted volume fraction of martensite from time and temperature data exported from the FE simulations. Using the JMA equation as before, the volume fraction of γ increases cumulatively upon heating. However, in this instance, the volume fraction of γ is reset to zero upon cooling below the martensite finish temperature (M_f , 643 K) [54,115]. As detailed in Section 4.3.2, the volume fraction of martensite present after cooling was considered to be equal to that of austenite at either the martensite finish temperature (M_f) or the point at which the cooling rate dropped below the critical cooling rate required for the formation of martensite, after which it is considered to be constant.

Figure 45 shows significant conversion ($>20\%$) to γ -phase predicted at traverse speeds of 25 mm/s and below. The predicted volume fraction of non-ferritic phases after cooling for these traverse speeds is shown in Figure 46.

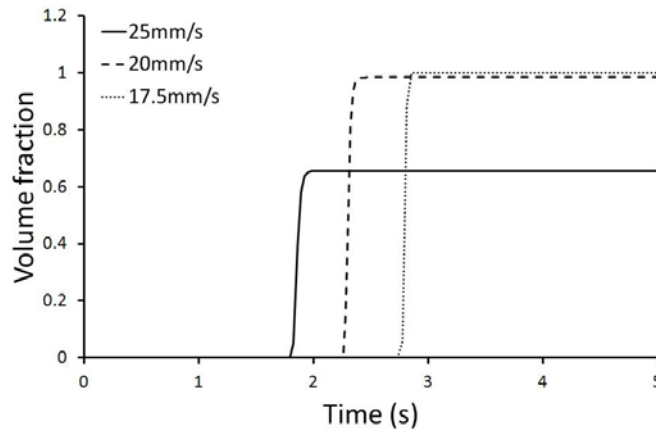


Figure 46 - Single pass FE simulation of volume fraction of non-ferritic phases on the top surface at the centre of the sheet (80 x 80 x 1.5 mm mild steel AISI 1010, 760 W, 5.5 mm beam diameter, 80% absorption).

The spatial extent to which this increase in non-ferritic phases with decreasing traverse speeds occurs is tempered by a corresponding reduction in cooling rates, shown in Figure 47.

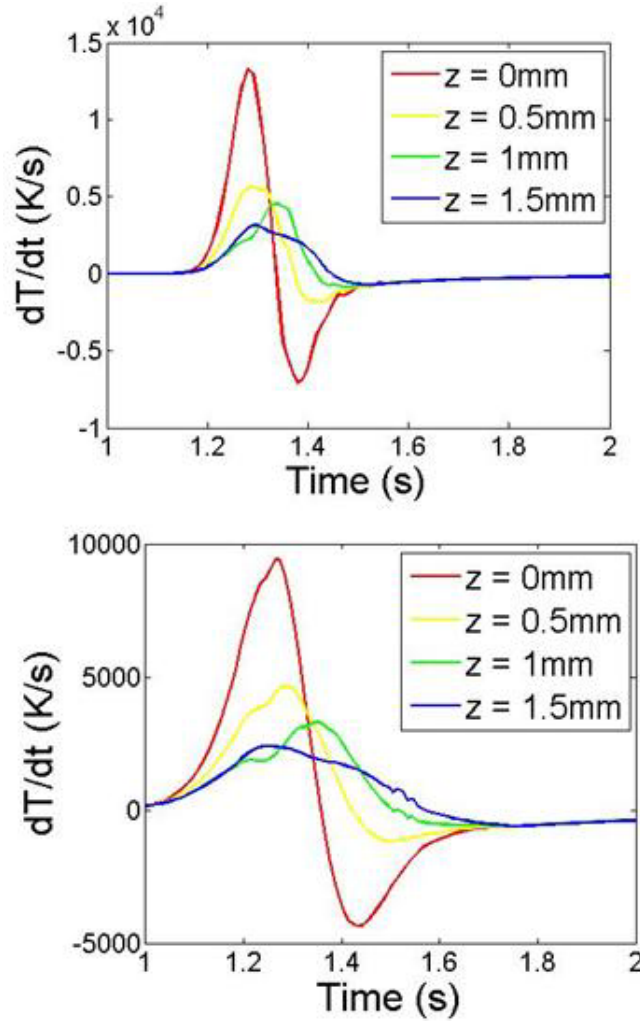


Figure 47 - Single pass FE simulation of temporal cooling rate on the top surface at the centre of the sheet for a) 35 mm/s and b) 17.5 mm/s (80 x 80 x 1.5 mm mild steel AISI 1010, 760 W, 5.5 mm beam diameter, 80% absorption).

It is worth noting that the volume fraction of austenite for the central parameter set used in this investigation ($v_0 = 35$ mm/s, $P = 760$ W, $\omega_0 = 2.75$ mm) increases significantly at the leaving edge of the sheet due to geometrical restrictions. At this edge, more heat accumulates relative to the central portion of the sheet as there no longer a bulk of substrate in advance of the beam to act as a heat sink. The predicted conversion to martensite is depicted in Figure 48.

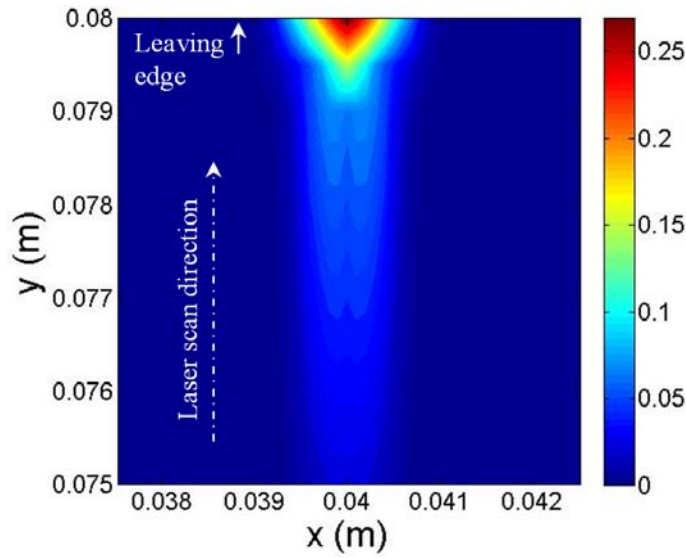


Figure 48 - Simulated martensite volume fraction on the surface of the substrate at the leaving edge after a single irradiation. (80 x 80 x 1.5 mm mild steel AISI 1010, 760 W, 5.5 mm beam diameter, 35 mm/s, 80% absorption).

The magnitude of heat accumulation effects on predicted microstructure can be reduced by varying the traverse speed during processing, specifically speeding up when approaching the leaving edge of the plate (see Section 5.3.5).

As discussed in Section 2.2.3, the net detrimental effect of microstructural change during LF was hardening, increasing the flow stress of the component and making it more difficult to deform. As such, solid-state diffusion of carbon from the absorptive graphite coating into the surface of the component is undesirable. The likelihood of solid-state diffusion of carbon into the surface of the component for the process parameters used in this investigation ($v_0 = 35$ mm/s, $P = 760$ W, $\omega_0 = 2.75$ mm) was investigated using the finite difference (FD) diffusion model detailed in Section 4.2. As detailed in Section 4.2.2, the transient diffusion of carbon from the graphite layer into the substrate surface is described by Fick's second law.

$$\frac{\partial C}{\partial t} = D \frac{\partial^2 C}{\partial z^2} \quad (84)$$

Where C is the percentage weight concentration of carbon and D is the diffusion co-efficient (m^2/s) which can be calculated using the following equation,

$$D = D_0 e^{-\left(\frac{Q}{RT}\right)} \quad (85)$$

where D_0 is the proportionality constant (m^2/s), Q is the activation energy of diffusion (J/mol), T is the temperature (K) and R is the universal gas constant (8.3 J/mol/K). Values for D_0 and Q were sourced from literature as $2.00\text{e}^{-5} \text{ m}^2/\text{s}$ and $1.42\text{e}^5 \text{ J/mol}$ respectively for austenite [116]. For the purposes of this simple model the assumption was made that austenitization is completed prior to the substrate reaching the A_3 temperature (that is, between the A_1 and A_3 critical temperatures). The boundary condition for maximum carbon concentration on the top surface of the component was set at a constant value of 0.8 %wt. This value was chosen from the iron-carbon phase diagram as suitable on the basis of peak temperatures typically encountered in LF of mild steels and the absence of melting from the process. Figure 49 shows the predicted additional carbon content with increasing distance from the surface after a single irradiation.

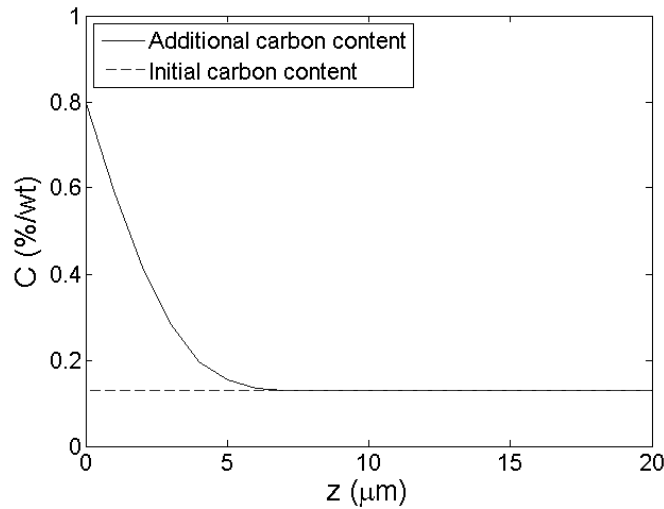


Figure 49 - Cumulative bend angle (80 x 80 x 1.5 mm mild steel AISI 1010, 760 W, 5.5 mm beam diameter, 35 mm/s, force cooled).

Figure 49 shows predicted additional carbon concentration at distances from the surface of up to approximately 6 μm . However, the model assumes austenitization is completed prior to the substrate reaching the A_3 temperature, whereas microstructure modelling suggests that this would not be the case in this instance. For solid-state diffusion of carbon into the surface of the component from the graphite layer to occur austenite must be formed in the HAZ during

laser heating. Figure 45 shows a predicted volume fraction of austenite on the top surface of the component of just 0.02 for the central parameter set used in this investigation ($v_0 = 35$ mm/s, $P = 760$ W, $\omega_0 = 2.75$ mm) and as carbon solubility in ferrite is very low it is predicted that any carbon diffusion under these conditions will be negligible. A single scan laser formed component was cross-sectioned, mounted in resin, polished and subsequently etched to reveal its grain structure along the irradiation path (see Figure 50).

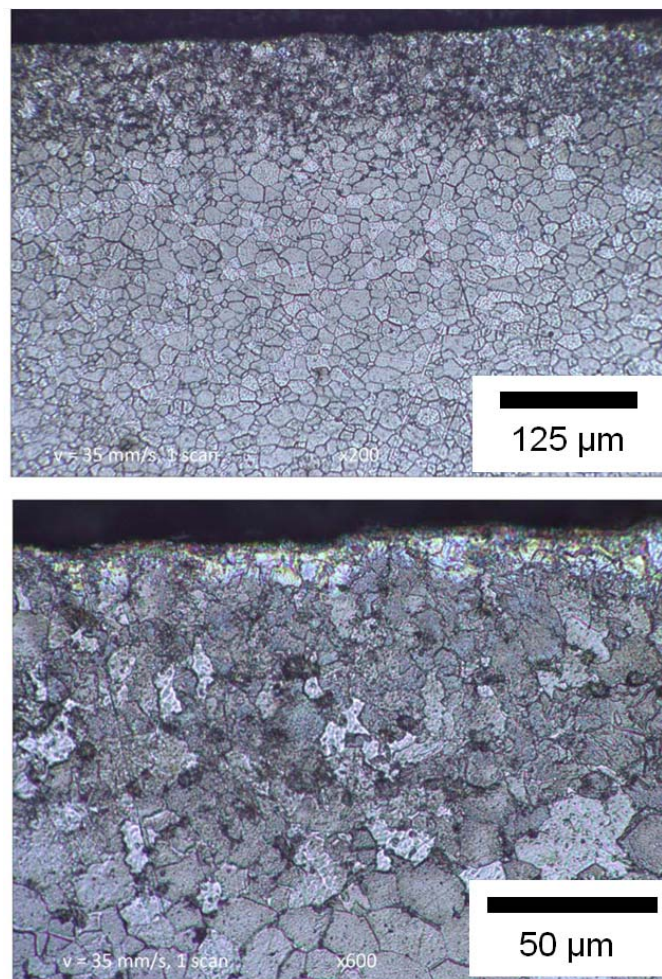


Figure 50 - Microscope image of heat affected zone (80 x 80 x 1.5 mm mild steel AISI 1010, 760 W, 5.5 mm beam diameter, 35 mm/s, 1 scan, 200x).

Figure 52 reveals no martensite grains present in the HAZ, despite the fact that FE simulated cooling rates were well in excess of the critical cooling rate required for martensitic transformation. This is concordant with the microstructure modelling prediction in Figure 45

of an austenite volume fraction of just 0.02 during laser heating. Smaller ferrite and pearlite grains than those in the base material were observed in the HAZ which could possibly be attributed to residual stresses affecting how the material was etched.

Figure 51 presents micro-hardness measurements taken throughout the cross-section of the component along the centre of the irradiation path after 60 irradiations. The initial hardness refers to hardness values that were measured in the cross section of a non-processed sample. The initial hardness was averaged over five measurements and found to be 122 HV, consistent with previously reported hardness values of 125 HV for normalised AISI 1010 mild steel [117].

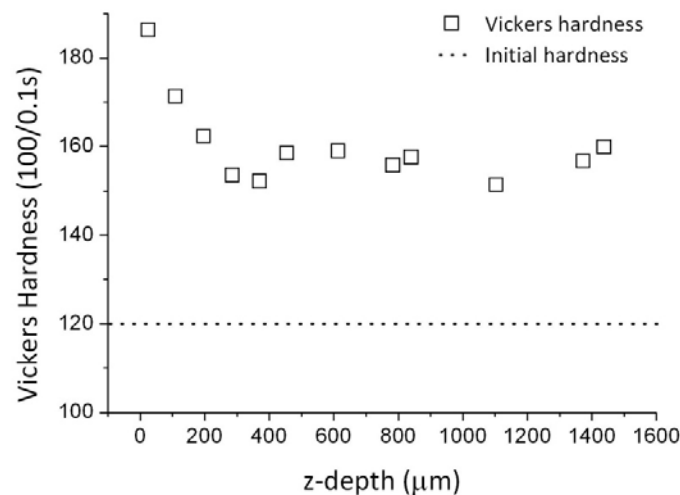


Figure 51 - Vickers hardness variation with increasing z-depth along irradiation path (80 x 80 x 1.5 mm mild steel AISI 1010, 760 W, 5.5 mm beam diameter, 35 mm/s, 60 scans).

A gradual increase in Vickers hardness is observed with increasing proximity to the component surface. This increase in hardness near the surface can be attributed to both phase constitution of the material and work hardening effects. The surface of the component was subjected to a higher peak temperature and significantly more plastic deformation during the forming process, leading to an increase in work hardening. In addition, the hardness values in this region are lower than could be expected for martensite in a plain carbon steel with 0.08 to 0.13 %wt C (approximately 300 HV) [116]. This is concordant with modelling predictions for phase transformations and carbon diffusion.

5.3.3 Variation in absorption

Absorption effects play a key role in the LF process and as such can have a large degree of influence on the bend angle *per pass*. Typically, a defocused beam is employed in order to achieve sub-melting temperatures on the top surface of the component. To aid the coupling of laser radiation into the component a graphite coating is applied. Previous research [118] has shown that, with successive irradiations, this coating is degraded or ‘burnt-off’, reducing the amount of energy coupled into the component with subsequent passes, detrimentally affecting the bend angle *per pass*. Figure 52 shows the cumulative bend angle and the bend angle *per pass* for both the experimental process and the analogous FE simulation.

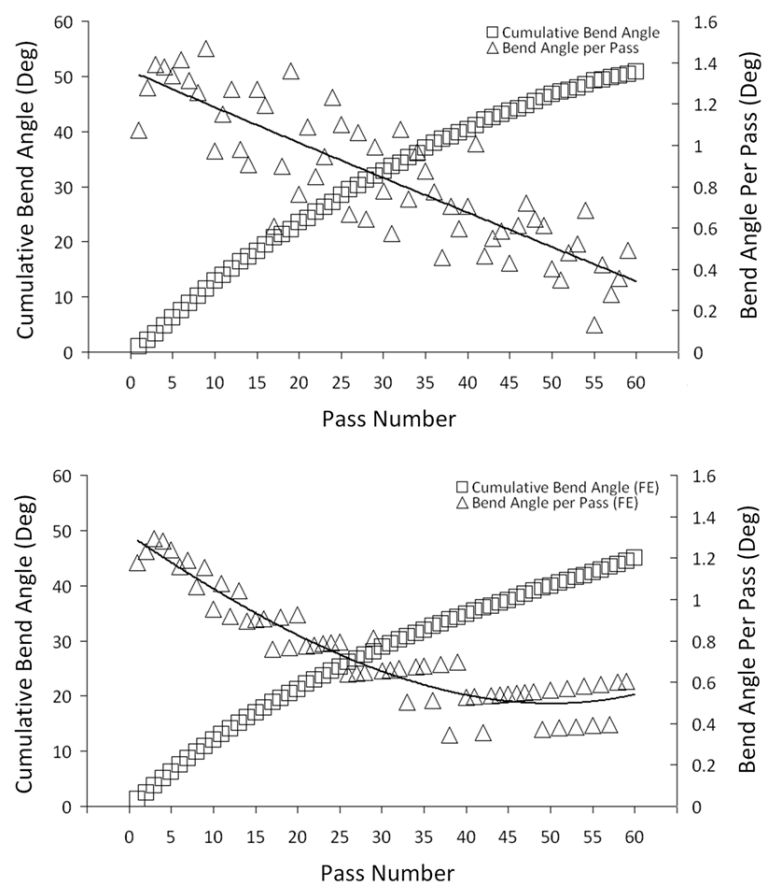


Figure 52 - Cumulative bend angle and the bend angle per pass for a) experimental and b) simulation of LF (80 x 80 x 1.5 mm mild steel AISI 1010, 760 W, 5.5 mm beam diameter, 35 mm/s, 80% absorption).

It is important to note that, in the FE simulation, the absorption coefficient is kept constant at 0.8. The simulated trend is similar to the experimental until around 35 passes, from which

point it stabilizes as the experimental trend continues to fall. This suggests that the observed graphite burn off becomes detrimental to the process only after a significant number of passes. This could be due to either less energy being coupled into the component as it becomes more reflective or the loss of the secondary heat source that the burning graphite provides.

To determine the magnitude of influence that graphite burn-off has on bend angle *per* pass a 60 pass experiment was conducted in which the graphite layer was removed with acetone and re-applied after thirty passes. A compressed air jet was applied to the underside of the workpiece in order to cool the substrate between passes. This ruled out any disparity in the thermal cycle between the recoated and non-recoated sample introduced as a result of time taken to clean off and re-apply the graphite layer.

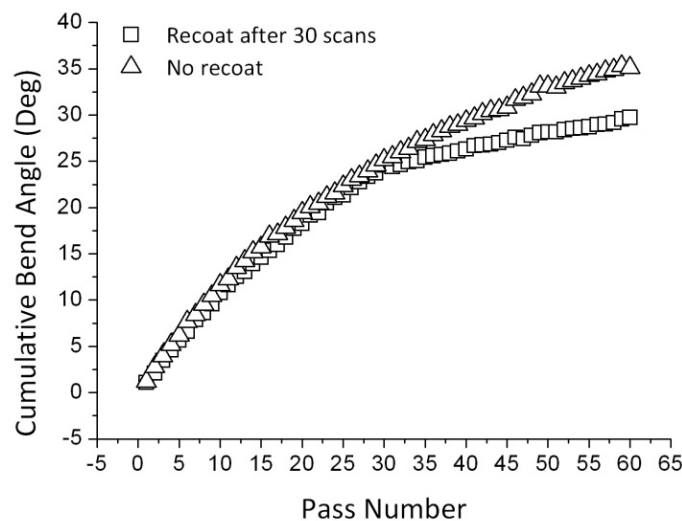


Figure 53 - Cumulative bend angle (80 x 80 x 1.5 mm mild steel AISI 1010, 760 W, 5.5 mm beam diameter, 35 mm/s, force cooled).

Figure 53 suggests that re-applying the graphite coating has a detrimental effect on the cumulative bend angle, in contrast to observations made by Edwardson *et al.* during the laser forming of Ti-6Al-4V [19]. In this instance, the reduction in cumulative bend angle for the recoated sample can be rationalized in terms of heat loss to the surroundings as the fresh graphite incandesces under irradiation. It is worth noting, however, that the standard deviation in bend angle *per* pass is lower for the recoated sample after the re-application of the graphite coating.

5.3.4 Geometrical effects

With increasing bend angle the initially circular beam incident on the components surface becomes more elliptical in shape [70], as depicted in Figure 54.

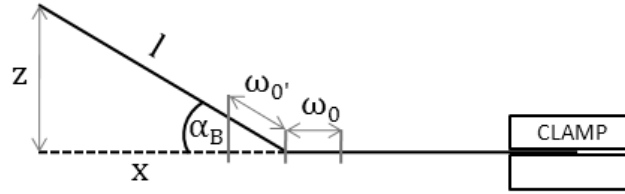


Figure 54 - The geometrical effect in LF for an edge clamped arrangement.

This has the effect of reducing the energy density of the beam, with a significant reduction (>20%) occurring at bend angles greater than 35°, this remaining the case regardless of spot size. The relationship between bend angle, initial beam radius and irradiation area A is described by Equation (86).

$$A = \frac{\pi\omega_0^2 + \pi\left(\frac{\omega_0}{\cos\alpha_B}\right)^2}{2} \quad (86)$$

A simulation was conducted in order to analyze the effect that such a corresponding decrease in energy density had on the initial bend angle, as depicted in Figure 55. A combination of both a Gaussian and modified Gaussian intensity distribution was applied to two separate boundaries either side of the irradiation path, Equation (87) and (88), respectively.

$$I = I_0 e^{\left[-\frac{2\left(\sqrt{(x-x_0)^2 + (y-y_0)^2}\right)^2}{\omega_0^2}\right]} \quad (87)$$

$$I = I_0 e^{\left[\left[-\frac{2\left(\sqrt{(x-x_0)^2}\right)^2}{\omega_0^2}\right]\left[-\frac{2\left(\sqrt{(y-y_0)^2}\right)^2}{\omega_0^{2i}}\right]\right]} \quad (88)$$

The modified Gaussian distribution used separate beam radius values in the x and y axis to give the elliptical shape associated with the geometrical effect.

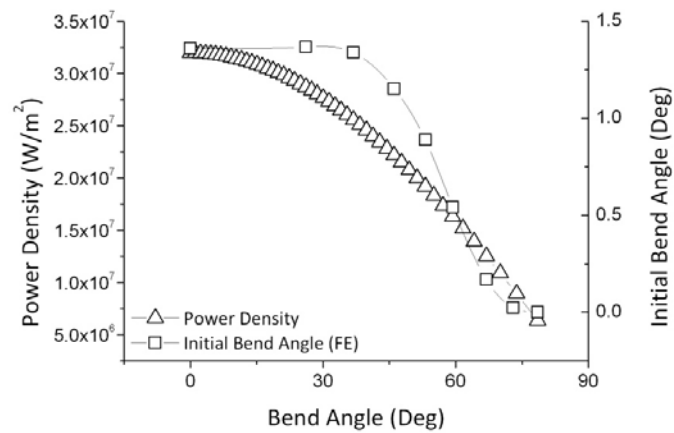


Figure 55 - Effect of reducing energy density on simulated initial bend angle (80 x 80 x 1.5 mm mild steel AISI 1010, 760 W, 5.5 mm beam diameter, 35 mm/s, 80% absorption).

From Figure 55 it can be seen that the reduction in energy density associated with the geometrical effect becomes highly detrimental at bend angles of approximately 35° or greater.

5.3.5 Edge effects

A single pass FE simulation of the LF process was conducted and the development of the resultant asymmetrical edge effect [119] was monitored. This effect consists of a relatively larger displacement at the leaving edge of the plate which can be attributed to less effective conductive cooling and thus a greater amount of plastic compression. Such asymmetrical edge effects are undesirable.

Cheng *et al.* [120] also noted the effects of heat accumulation at the leaving edge of the sheet, proposing the use of compressed air jets applied to both the top and bottom surface of the workpiece to achieve greater uniformity in thermal cycles across the length of the component. This approach was successful in reducing the radius of curvature of the formed part. Whilst applicable to the straight line forming of flat sheets, such an experimental set-up would prove difficult to implement for larger and more complex geometries. Therefore, a solution utilizing readily variable process parameters (such as power, traverse speed and spot size) is preferable.

In the FE simulation conducted, the traverse speed was varied to reduce the line energy after the beam reaches the halfway point of the sheet, the results of which are shown in Figure 56.

This had the effect of reducing the amount of heat which the leaving edge was required to dissipate.

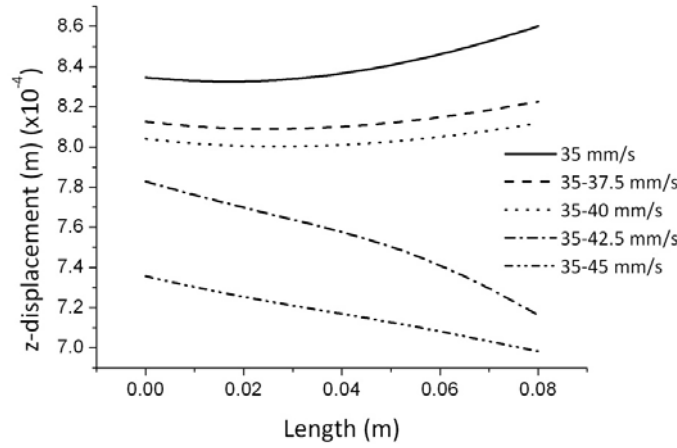


Figure 56 - Single pass FE simulation of edge effects with different scan strategies (80 x 80 x 1.5 mm mild steel AISI 1010, 760 W, 5.5 mm beam diameter, 80% absorption).

From the simulation results the optimum combination of traverse speeds was found to be 35 mm/s (v_1) and 40 mm/s (v_2). This was determined by calculating the radius of curvature (R) and the difference in magnitude of displacement between either edge ($D_{(max-min)}$).

$$R = \frac{\left\{ 1 + \left(\frac{dx}{dy} \right)^2 \right\}^{\frac{3}{2}}}{\frac{d^2 y}{dx^2}} \quad (89)$$

Analogous experimentation was conducted which also found this combination of traverse speeds to be optimal, as detailed in Table 4.

v_1 (mm/s)	v_2 (mm/s)	FE			Experimental		
		R	$D_{(max-min)}$ (mm)	α_B (Deg)	R	$D_{(max-min)}$ (mm)	α_B (Deg)
35	35	92.524	0.011	1.205	3.921	0.131	1.162
35	37.5	104.597	0.01	1.165	26.822	0.222	1.260
35	40	116.932	0.008	1.152	95.243	0.144	1.068
35	42.5	98.271	0.067	1.08	44.221	0.0725	0.932
35	45	17857.14	0.037	1.027	274.125	0.198	0.794

Table 4 - R , $D_{(max-min)}$ and α_B for both experimental and simulated single pass LF of 80 x 80 x 1.5 mm mild steel AISI 1010, 760 W, 5.5 mm beam diameter, 80% absorption.

Chapter 6

NUMERICAL SIMULATION OF LASER FORMING FOR FEASIBILITY STUDY

Numerical modelling has the potential to replace extensive and time consuming empirical studies into investigating the applicability of lasers for the forming of specific geometries. In this chapter a feasibility study of the LF of square-section mild steel tubes for the automotive industry is detailed, with specific emphasis on numerical simulation as part of the process.

This investigation was conducted in conjunction with Honda Engineering Europe Ltd.

6.1 Introduction

The chassis of a motor vehicle typically comprises a hollow tube, usually made of a high strength steel alloy. The use of steel provides the necessary rigidity and strength whilst its hollow structure keeps weight down.

During production, such tubes are formed into the required shape using press tools, with the components susceptible to ‘spring back’ effects associated with mechanical forming techniques. This makes achieving good manufacturing tolerances on the assembly line particularly difficult.

Laser forming has the potential to be used in the post-processing of such mechanically formed components, as demonstrated experimentally by Silve *et al.* [121]. For example, a closed loop system could be implemented in which the component is ‘tweaked’ to within desired tolerances using an iterative approach. Such an approach would profile the component after each application of laser radiation and increment towards the desired geometry.

Initially, however, the applicability of the LF process must be established, with consideration given to throughput time, subsequent component performance (effect on fatigue/corrosion

properties) and specific pre/post-processing requirements; that is absorptive coatings and subsequent coating removal.

In this chapter, the use of FE modelling in conjunction with analogous experimentation in a feasibility study into the applicability of LF for the forming of mild steel rectangular section tubes for the automotive industry is investigated. Since the aim of this investigation was solely to establish the viability of LF for the shaping of such components, mild steel was chosen as an alternative to high strength alloy steel.

6.2 Experimental Procedure

6.2.1 Experimental set-up

An experimental study was conducted on graphite coated 23 x 200 mm AISI 1010 square section steel tubes with a wall thickness of 1.5 mm and a seam weld along the base section. The tubes were formed using a 1.5 kW CO₂ TEM₀₀ fast axial flow laser (Electrox Ltd.) with a 3-axis CNC beam delivery system (Galil Motion Control Ltd.), custom written control software and operating in CW mode. Supplied by Honda Engineering Europe Ltd., the tubes were clamped using a rotary stage mounted on the *xy* table and controlled using a micro-controller (ITC6DCA, Micro-Controle Inc.), as depicted in Figure 57.

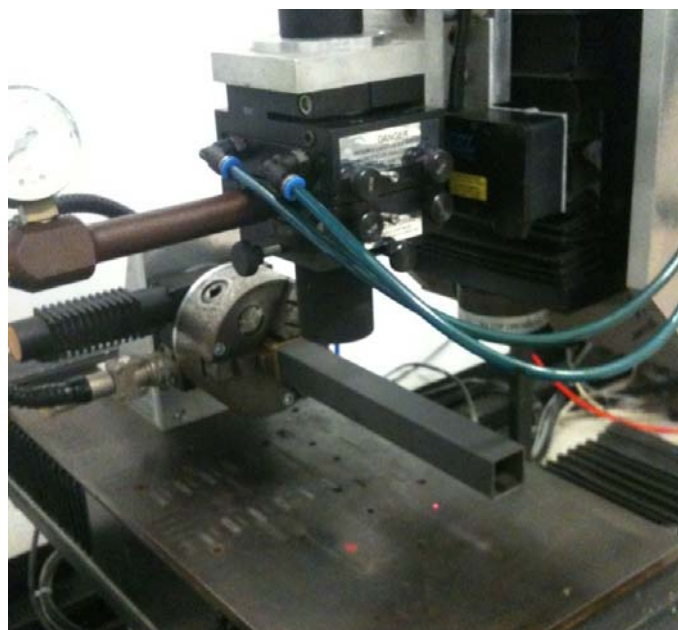


Figure 57 - Edge clamped rotation stage arrangement.

The deformation was measured off-line using a Faro arm 3D profiling system, as shown in Figure 58.

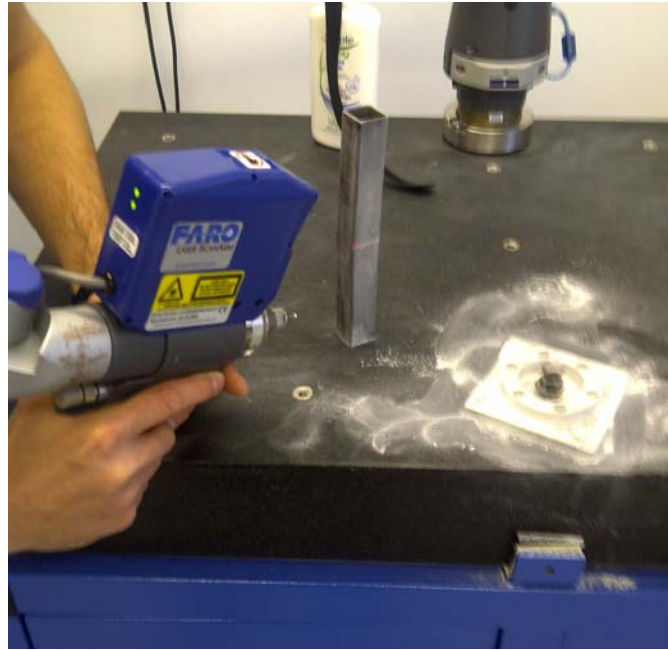


Figure 58 - Faro Arm 3D profiling system.

Both the CNC workstation in the laboratory and the beam in the simulations were manipulated by a custom developed MATLAB GUI, Irradiation Path Draw (IP_Draw), created specifically for this investigation. A screenshot of the GUI is shown in Figure 59.

Using IP Draw, the movement of the beam over a specified 2D geometry could be described by a series of co-ordinates in any combination of two Cartesian axes. Once the basic beam path is plotted and visualised, linear interpolation by a user specified factor can be carried out if desired, smoothing the path. The GUI outputted both COMSOL compatible interpolation files (which describe the movement of the beam in x , y or z relative to time) and G-code for the manipulation of the CNC workstation in the laboratory.

An important feature utilized in this investigation is the ability to specify both a start and finish traverse speed for a given scan path. This allows for the linear variation of traverse speed along the scan path which can be desirable, for example, when speeding up on approaching the edges of a geometry in order to avoid excessive heating.

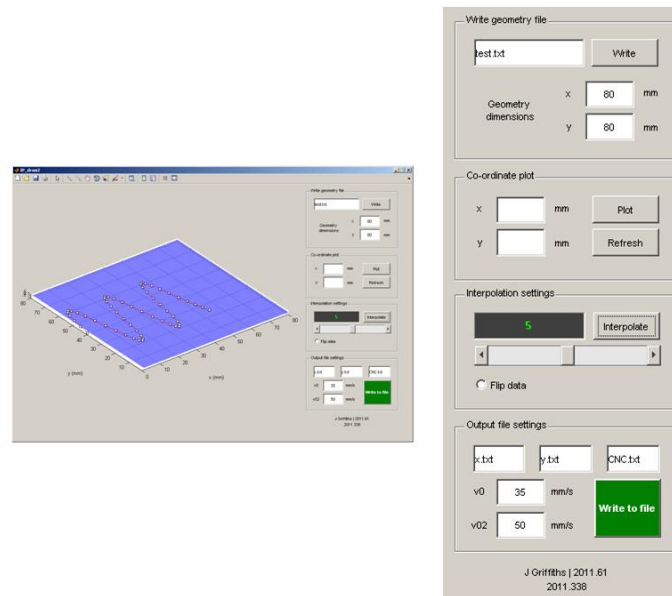


Figure 59 - Screenshot of the IP_Draw GUI.

The MATLAB generated G-code was implemented via a GUI based terminal, shown in Figure 60, on the ElectroX system. The terminal, created in Visual Basic, can also be used as a jog controller to move the stages ‘manually’. The decision to use G-code rather than develop a custom GUI (as used in Chapter 5) in this instance was due to the flexibility it offered in developing novel scan strategies during the investigation. The various scan strategies coded for are described in results section whilst an example of the G-code generated by IP_Draw is included in Appendix C.

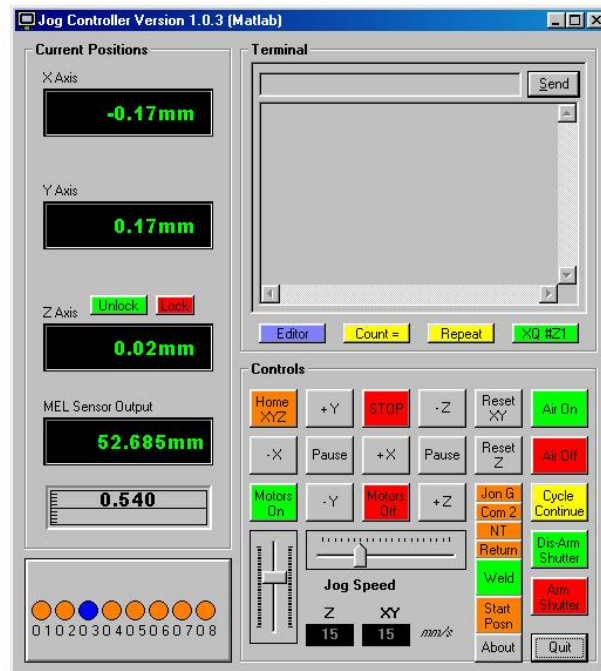


Figure 60 - Screenshot of the Jog Controller and terminal.

6.2.2 FE model development

A full thermal-mechanical model of the LF of rectangular section mild steel tubes was developed in COMSOL Multiphysics, using the same method as detailed in Section 5.2.2. The geometry used in the simulations is shown in Figure 61.

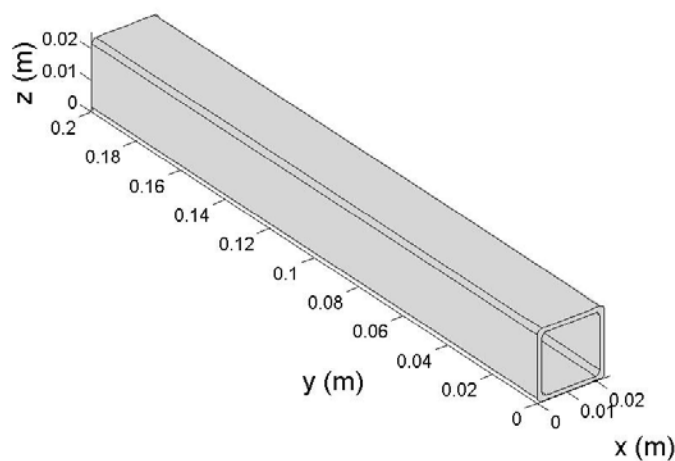


Figure 61 - Geometry used in FE simulations.

The global mesh element size was set to coarse and determined by a built-in algorithm in COMSOL. A suitable maximum element size for use along the irradiation path was determined by convergence study and found to be 0.1 mm. The meshed geometry is depicted in Figure 62.

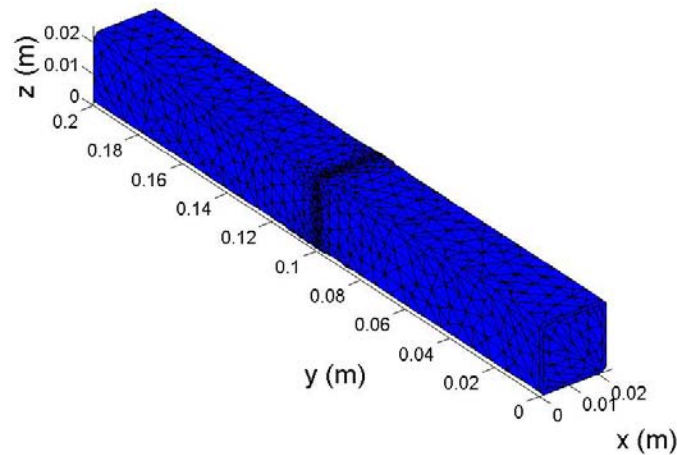


Figure 62 - Meshed geometry used in FE simulations.

The laser beam was approximated to an ideal Gaussian intensity distribution and applied to model using the method detailed in Section 5.2.2.1.

6.3 Axial Bending

6.3.1 Applicability of the temperature gradient mechanism

Initially, experimental and numerical parametric studies were conducted in order to find suitable process parameters. 80 x 30 x 1.5 mm AISI 1010 steel coupons were used for this investigation, which involved measuring the bend angle *via* laser triangulation after a single irradiation at all combinations of power, traverse speed and spot size within a suitable range available using the Electrox CO₂ laser system (see Table 5).

Power (W)	Traverse speed (mm/s)	Distance from focus (mm)
300	30	20
500	50	40
800	80	60

Table 5 - Processing parameters used in parametric study.

The results of the parametric study are shown in Figure 63.

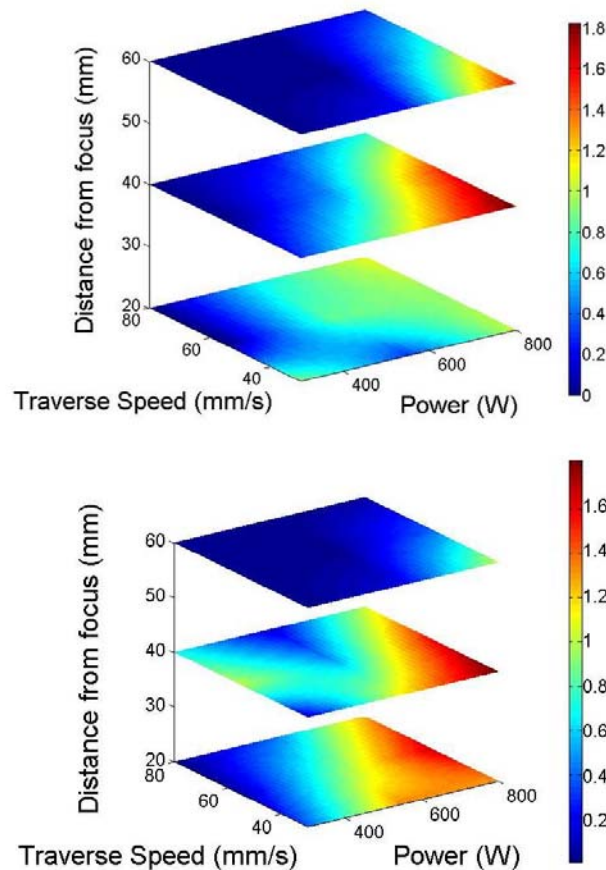


Figure 63 - Experimental (top) and simulated (bottom) initial bend angle in degrees as a function of traverse speed, power and distance from focus.

Figure 63 shows good agreement between both experimental data and simulation results. The focal distances of 20, 40 and 60 mm were found to equate to approximately 4, 6 and 8 mm beam diameters. These were measured using Perspex beam prints.

Optimum process parameters were found to be 800 W average power, 50 mm/s traverse speed and 6 mm beam diameter. The choice was made on the basis of HAZ appearance (that is, no evidence of melting).

Utilizing the numerically and empirically determined optimum process parameters, FE simulations were used to predict the applicability of the TGM to the axial bending of square

section tubes. Simulations were conducted using two truncated versions of the square section geometry; a horizontally sectioned half tube and one with just the central portion of one face removed, as depicted in Figure 64.

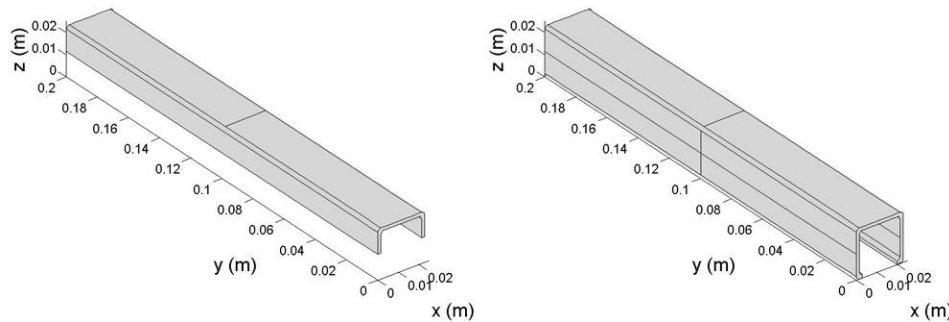


Figure 64 - Two geometries used in the FE simulations.

Use of these truncated geometries allowed for the visualization of the limits of applicability for the TGM in forming of full square section tubes. In the TGM relatively more shrinkage occurs on the upper surface of the irradiated region compared to the bottom surface during cooling. This can be attributed to plastic compression of the surface layer undergone during heating (see Section 1.2.1). For flat sheets this difference in degree of shortening throughout the component thickness results in out-of plane bending towards the beam.

As is evident from Figure 65, the results of the simulations suggested that the component was geometrically constrained from being formed by the TGM. In the case of the half-section tube shown in Figure 68, the bending moment resulting from differential shrinkage throughout the wall thickness along the scan path was sufficient to cause out-of-plane bending towards the beam. However for the tube with the central portion of one face removed, the relatively larger moment of inertia of the component constrained this out-of-plane deformation.

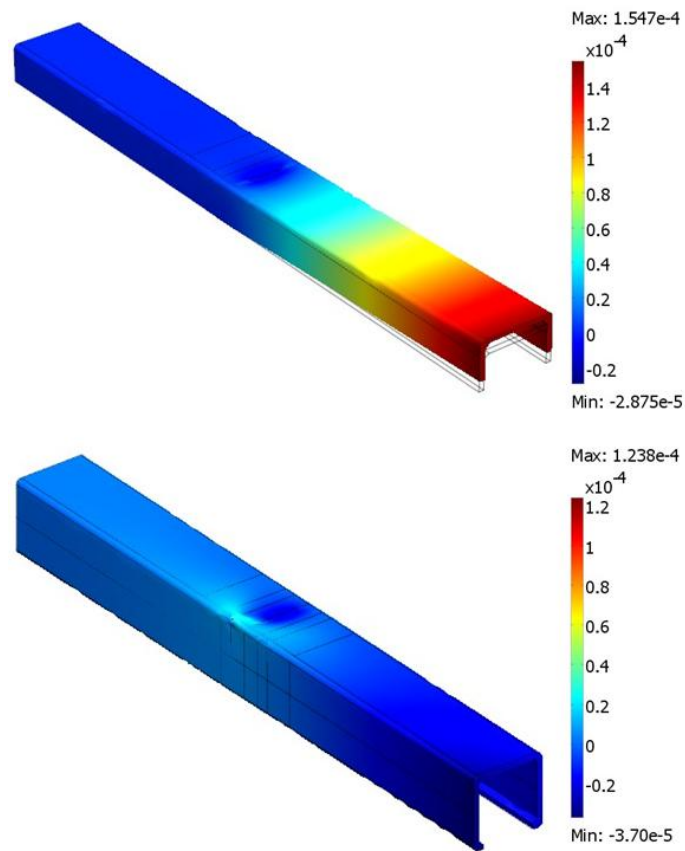


Figure 65 - FE simulated z -displacement in metres for two geometries using TGM process parameters (mild steel AISI 1010, 800 W, 6 mm beam diameter, 50 mm/s, 80% absorption).

An experimental study using full square section tubes and utilizing the same numerically and empirically determined optimum process parameters for the TGM used in the simulations resulted in no appreciable deformation, thereby validating the numerical predictions and confirming the unsuitability of the TGM for the axial bending of the component.

6.3.2 Applicability of the upsetting mechanism and in plane shortening

Having established the unsuitability of the TGM for out of plane bending, a series of scan strategies were devised with the intention of inducing in plane shortening around the central portion of the tube, as illustrated in Figure 66.

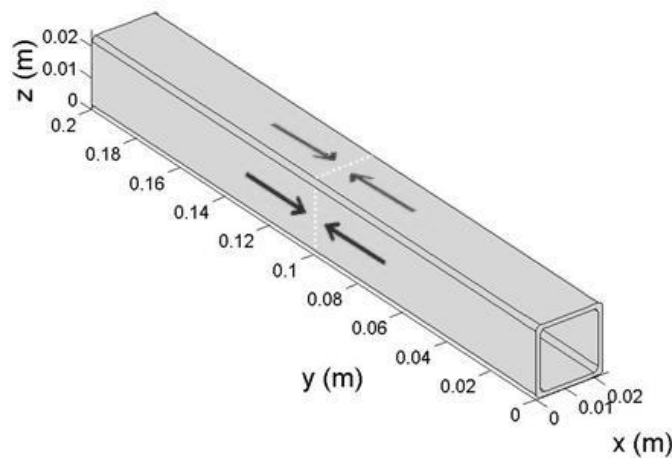


Figure 66 - Depiction of in-plane shortening of component.

To achieve this, process parameters typical of the buckling mechanism (BM) or upsetting mechanism (UM) were chosen (see Section 1.2.2 and 1.2.3 on the BM and UM for more detail on these mechanisms). Through use of process parameters in the UM regime (see Table 1) it was possible to induce a near uniform temperature distribution throughout the thickness of the irradiation zone. Compressive stresses develop in the irradiated region due to restriction of thermal expansion by the surrounding material. For flat sheets with thicknesses in the order of the wall thickness of the square section tubes used in this investigation (1.5 mm) such parameters would result in the formation an instability (or ‘buckle’) across the workpiece as a result of the near homogeneous thermal expansion in the irradiated area. However, in this instance buckle formation is prevented due to the large moment of inertia for the component. Therefore, the shortening in the irradiated region causes the component to bend towards the beam.

The un-predictable nature of the BM made a full parametric study less useful in selecting process parameters than for the TGM. Therefore, initial process parameters were chosen arbitrarily on the basis of a brief empirical investigation using a limited number of process parameter combinations. The investigation again comprised of 2D out of plane bending of 80 x 30 x 1.5 mm AISI 1010 components.

A parameter set of 500 W power, 10 mm/s traverse speed and an approximately 8 mm spot size was selected on the basis of net bending angle and HAZ appearance; that is, no evidence of melting having occurred.

6.3.2.1 Numerical simulation

FE simulations were conducted to assess the applicability of both in-plane shortening as a mechanism for out of plane deformation and the experimentally determined process parameters. Initially, scan strategy A was implemented, involving the sequential irradiation of three sides of the component as shown in Figure 67. It should be noted that the directions of the individual scans depicted in Figure 67 were chosen so as to allow the beam to traverse in alternate directions for ease of experimental implementation.

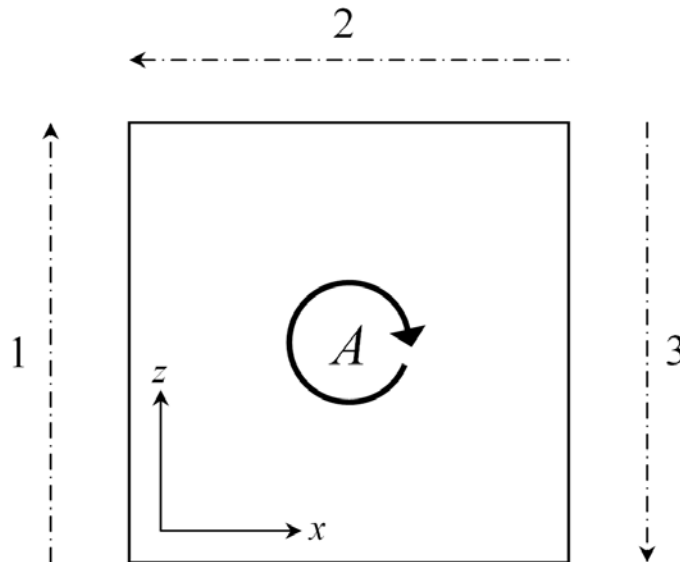


Figure 67 – Scan strategy A. Dashed-dot lines represent irradiation path and direction.

A simulation using scan strategy A was conducted in which the displacement in x , y and z was monitored, the results of which are shown in Figure 68. The overall solution time was set to 32 s to allow for cooling of the component and no rest time between irradiations was specified.

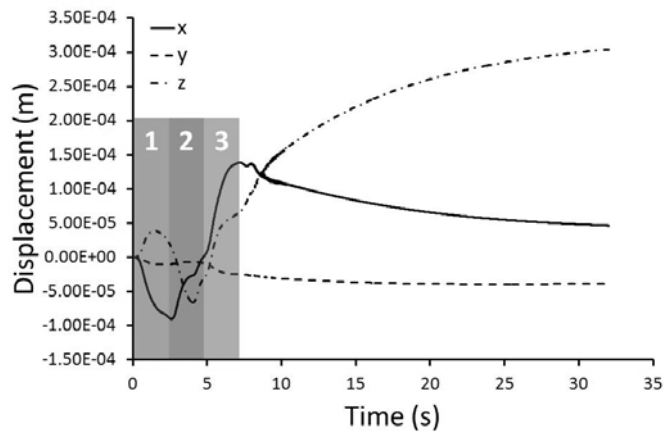


Figure 68 - Simulated x , y and z displacement (500 W, 8 mm beam diameter, 10 mm/s, 80% absorption).

As a result of scan 1 the component bends towards the beam, with no appreciable counterbend observed. The absence of counterbending can be attributed to the high stiffness of the component, the bulk of which is at room temperature at this stage in the process. A relatively small amount of deformation is also observed in the z -axis due to heat accumulation effects at the leaving edge of the scan path. This can be likened to the development of edge effects in straight line LF of flat sheets (see section 5.3.5).

Scan 2 initially causes the component to bend away from the beam due to counterbending, which is now possible as a result of the increase in temperature along one side of the component making it more ductile. During the post-heating stage, in-plane shrinkage of the top side of the component causes it to bend towards the beam.

Scan 3 proceeds in much the same manner as scan 1, resulting in bending towards the beam. However, the reduction in flow stress along two sides of the component allows for increased lateral deformation in this instance. As such, whilst the majority of out of plane deformation is in the z -axis, a significant portion of the deformation is in the x -axis which is highly undesirable, as shown in Figure 69.

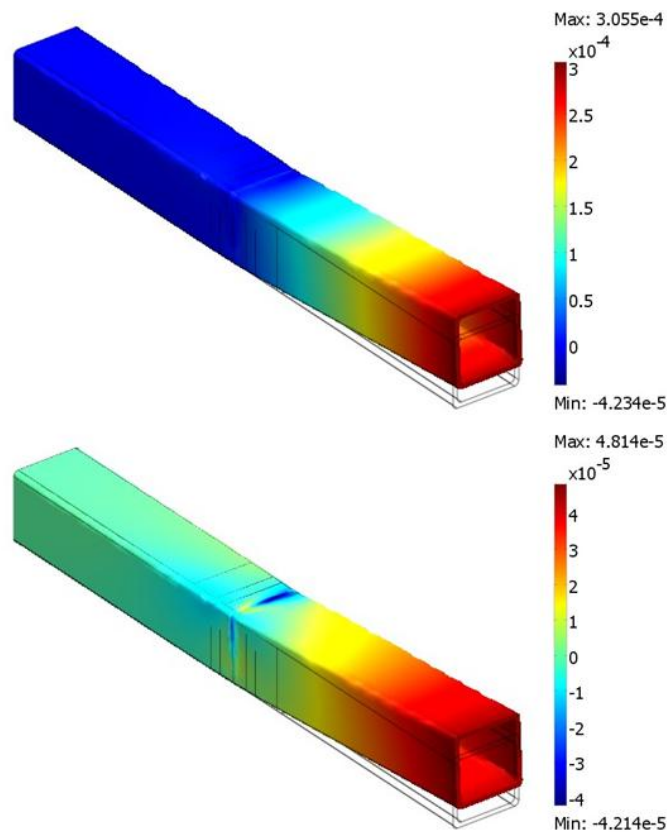


Figure 69 – FE simulated z and x -displacement in metres, top and bottom respectively (mild steel AISI 1010, 500 W, 8 mm beam diameter, 10 mm/s, 80% absorption, 20x deformation scale factor).

This undesired x -displacement can be attributed to both the asymmetric nature of the scan strategy and, to a lesser extent, the inherent asymmetry of the LF process itself. Safdar [85] noted that scanning in alternate directions across the circumference of the circular section tubes at their half way point reduced the undesired lateral deformation considerably when compared to circumferential scanning in the same direction due to alternating of the lateral bending for each scan. With this in mind scan strategy B, shown in Figure 70, was devised with the aim of reducing the amount of residual lateral deformation by addressing the asymmetry of the laser heating.

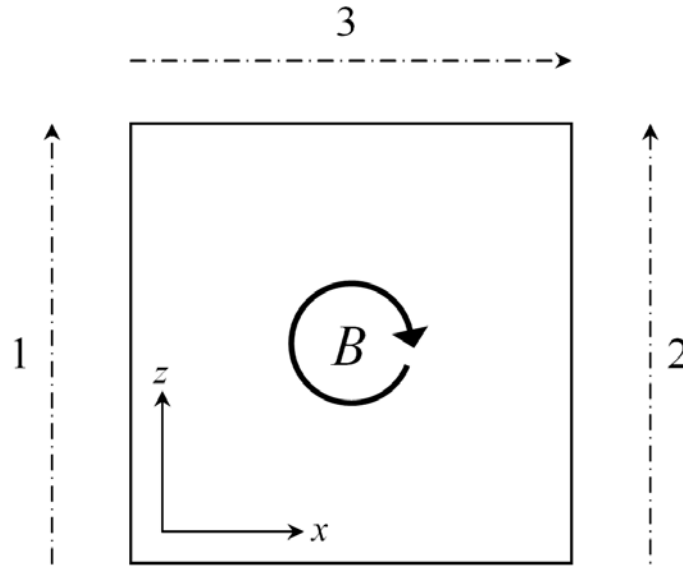


Figure 70 - Scan strategy B. Dashed-dot lines represent irradiation path and direction.

A simulation using scan strategy B was conducted, revealing a reduction in undesirable x -displacement whilst maintaining the magnitude of z -displacement when compared with scan strategy A, as shown in Figure 71.

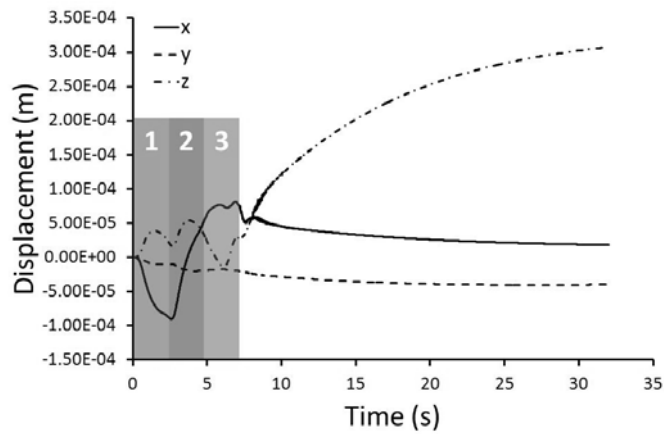


Figure 71 - Simulated x , y and z displacement (500 W, 8 mm beam diameter, 10 mm/s, 80% absorption).

As is the case for strategy A, scan 1 causes the component to bend towards the beam. This also results in deformation in the z -axis due to heat accumulation effects at the leaving edge of the scan path.

Scan 2 of strategy B is equivalent to scan 3 of strategy A, with both resulting in bending towards the beam. There is also an increase in lateral deformation observed when compared to the initial scan due to the elevated temperature of the central portion of the component. However, the magnitude of lateral deformation, whilst greater than for the initial scan, is reduced when compared to scan 3 of strategy A. This can be attributed to higher component stiffness as only one side of the component has been heated prior to irradiation in this instance.

6.3.2.2 Experimental study

LF of rectangular section tubes with scan strategy B was subsequently conducted experimentally. Due to the slow speed of rotation on the experimental set-up, significant dwell times were required to allow for the accurate positioning of the component, as detailed in Figure 72.

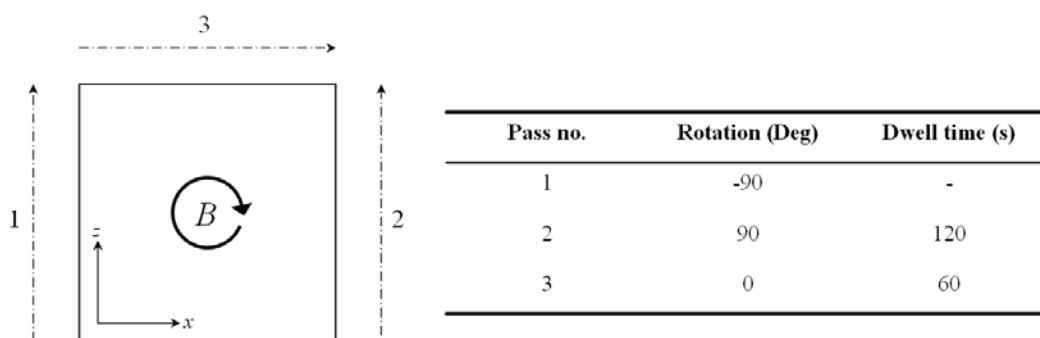


Figure 72 - Experimental scan strategy B. Dashed-dot lines represent irradiation path and direction.

Due to the incremental nature of the process and small angles achieved per iteration of scan strategy, scan strategy B was repeated ten times. A 3D profile of the formed component was obtained through use of a Faro Arm 3D profiling system.

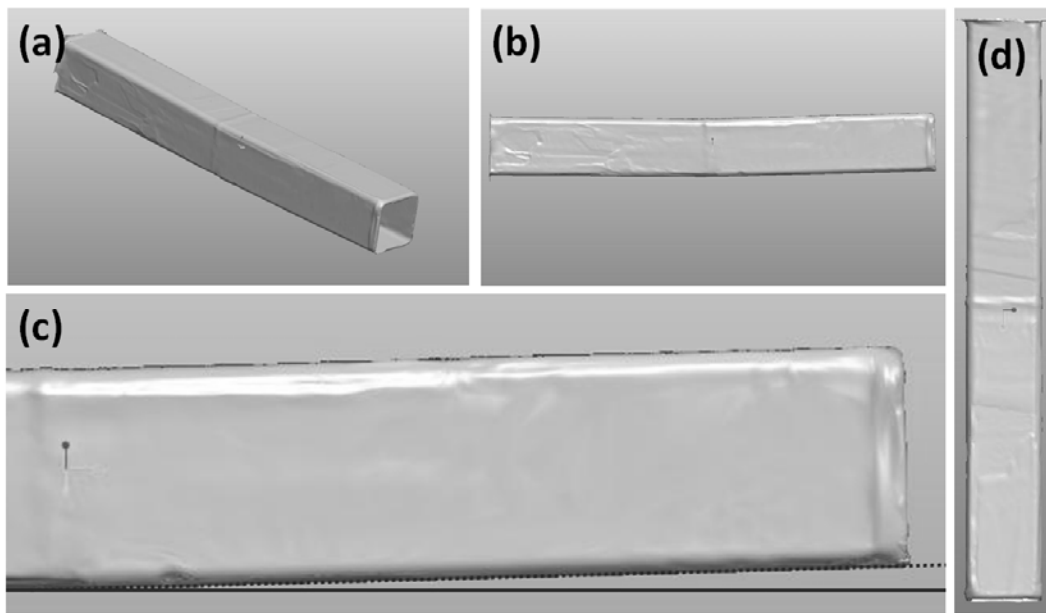


Figure 73 - 3D profile of a) formed component, b) side on view revealing significant z -displacement, c) close up of side on view and d) top down view revealing minimal x -displacement.

Figure 73 reveals significant deformation in z and whilst no appreciable lateral deformation is evident, thereby validating the numerical predictions. However, evidence of melting was observed along the HAZ after processing, suggesting the use of excessively high energy densities.

As discussed in Section 2.2.3, microstructural changes, specifically martensitic transformation upon cooling, can be detrimental to the LF process as the flow stress of the component is increased with increasing hardness. The experiment was repeated at 400 W and 300 W, with the effect on both the appearance of the HAZ and the net bending angle monitored, as shown in Figure 74 and Figure 75 respectively.

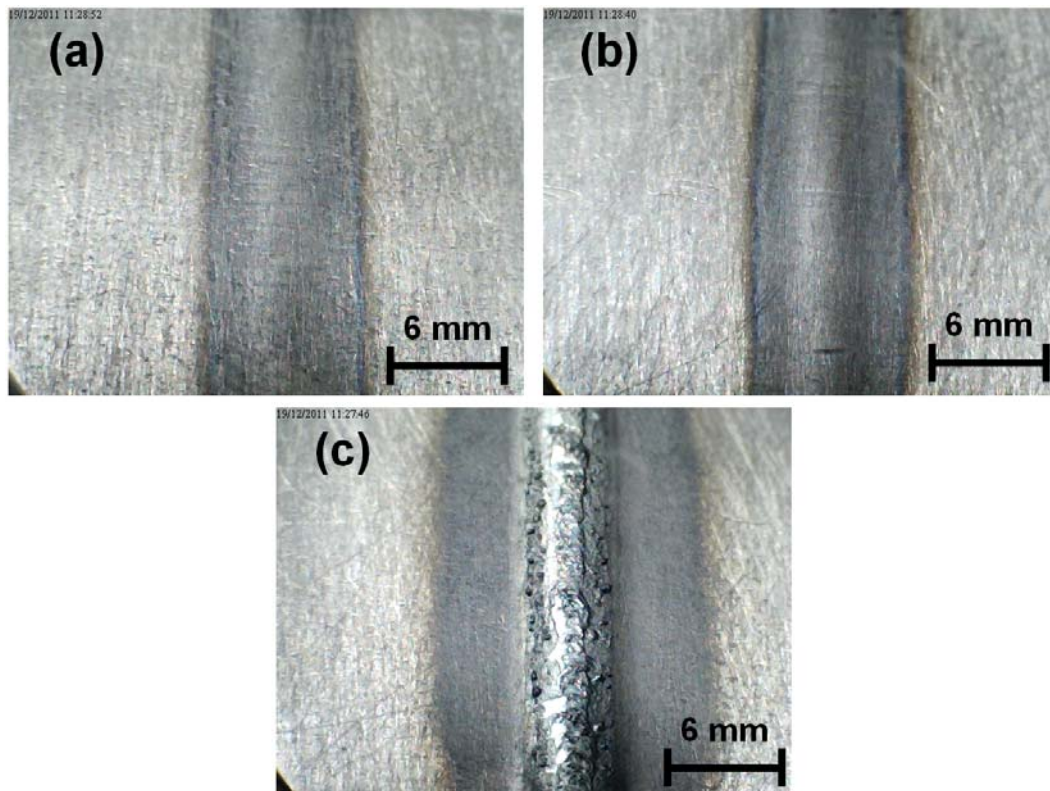


Figure 74 – Appearance of HAZ after ten iterations of scan strategy B at powers of (a) 300 W, (b) 400 W and (c) 500 W (8 mm beam diameter, 10 mm/s).

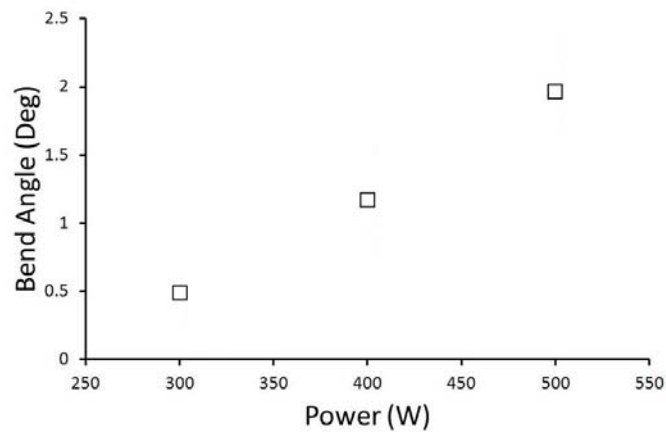


Figure 75 - Bend angle after ten iterations of scan strategy B at various powers (8 mm beam diameter, 10 mm/s traverse speed).

Process parameters of 400 W, 10 mm/s and 8 mm spot size were chosen as the best compromise between bend angle and appearance of HAZ. Using these parameters, an experiment was conducted in which the bend angle was monitored every second iteration of

the scan strategy after significant enough deformation was achieved (in this instance from 6 iterations onwards), the results of which are shown in Figure 76. The bend angle was determined from the z-displacement at the end of the tube, measured by ruler. It should be noted that a ruler was in preference to the laser range finder on the ElectroX system (M5, MEL Mikroelektronik GmbH.) due to its limited accuracy over the small range of deformation encountered in this investigation.

Due to the relatively crude nature of this technique, the measurements were validated using the Faro arm. Restricted access, remote location and long processing time (approximately 30 mins *per* sample) made taking all measurements on the Faro arm impractical.

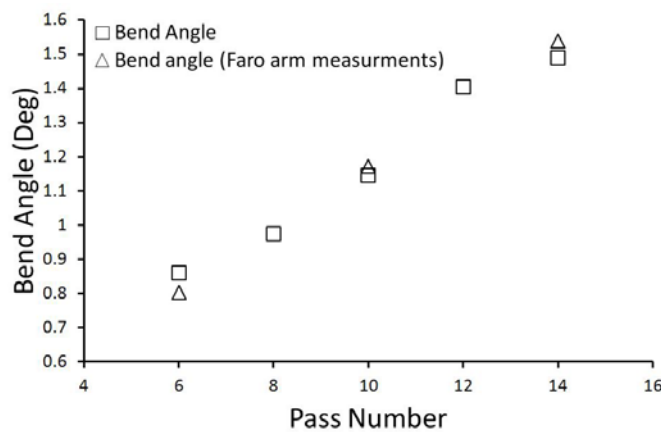


Figure 76 - Cumulative bend angle for multiple iterations of scan strategy B (400 W power, 8 mm beam diameter, 10 mm/s traverse speed).

Figure 76 highlights the incremental nature of the LF process, vital for its potential application in closed loop, iterative processes. Over the range of scan iterations investigated, the bend angle is linearly proportional to iteration number.

6.4 In-plane Twisting

6.4.1 Numerical simulation

The same principle of in-plane shortening applied to axial bending was subsequently used to achieve in-plane twisting of the tubes. Initially, a simulation was conducted which employed a ‘spiral’ scan strategy (strategy C), as depicted in Figure 77a. Scan strategy C consisted of four sequential irradiations, each on a different face of the square section tube. Half of the

tubes total length of 200 mm was divided into four sections of 25 mm in length, with each sequential irradiation traversing diagonally across its surface as shown in Figure 77b.

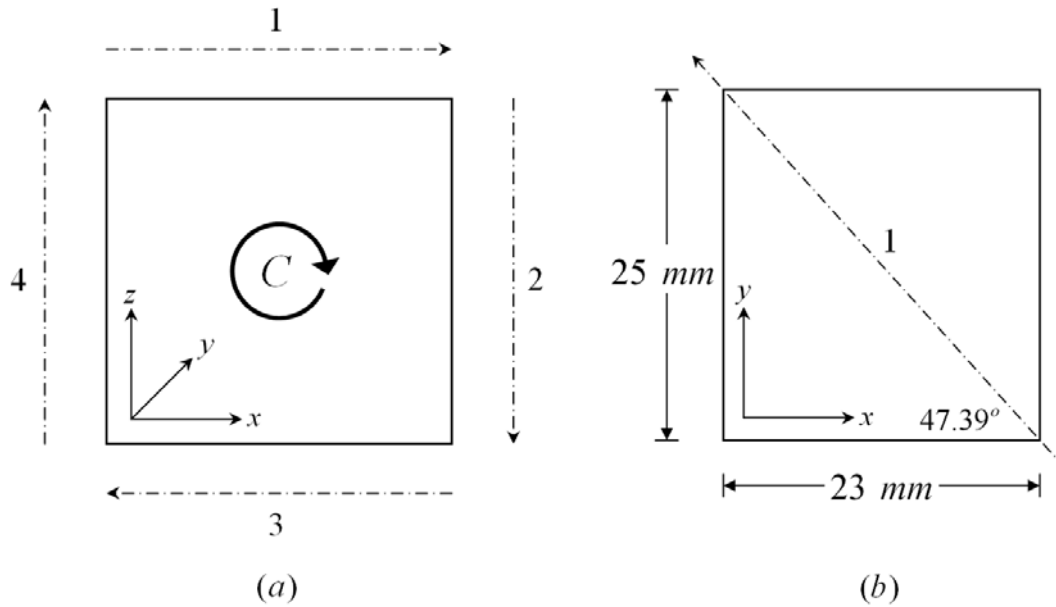


Figure 77 – Schematic diagram depicting (a) scan strategy C and (b) irradiation path for initial scan. Dashed-dot lines represent irradiation path and direction.

Using experimentally optimized process parameters from the axial bending investigation, a simulation was conducted in which scan strategy C was applied, resulting in a twisting of the component, as shown in Figure 78.

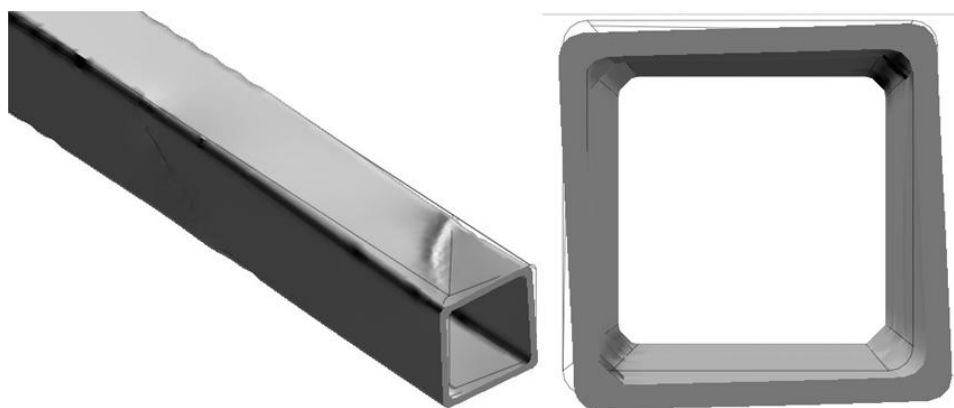


Figure 78 - Simulated overall displacement (400 W, 8 mm beam diameter, 10 mm/s, 80% absorption, 20x deformation scale factor).

It is worth noting that post-processing revealed the off-axis nature of the twist, as shown in more detail in Figure 79. This can be attributed to the inherent asymmetry of laser heating in the LF process and is similar in nature to the residual lateral deformation encountered in axial bending (see Section 6.3.2.1). In the case of in-plane twisting, a relative increase in the magnitude of out of plane deformation with each successive irradiation results in the development of an off-axis twist. This is due to the increasing temperature of the component with each successive irradiation, reducing the flow stress and making it easier to plastically deform.

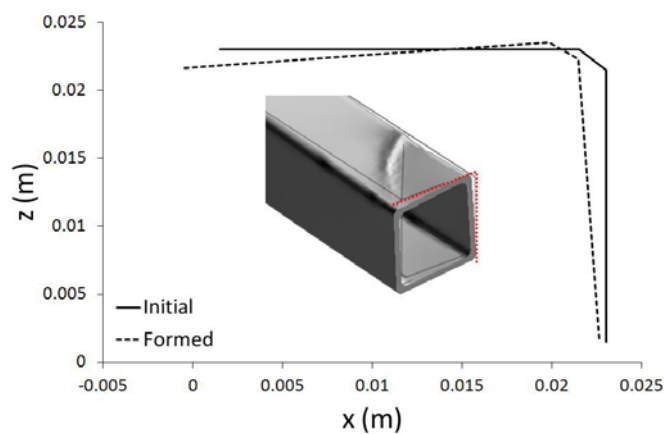


Figure 79 - Simulated overall displacement at the end of the component with FE post-processing image superimposed (400 W, 8 mm beam diameter, 10 mm/s, 80% absorption, 20x deformation scale factor).

6.4.2 Experimental study

Scan strategy C was implemented experimentally to validate the simulation results. As in the previous experimental investigation into axial bending, ten iterations of the strategy were applied. The 90° rotation required necessitated a dwell time of 60 s between irradiations. During this dwell time the stage was translated 25 mm in the y-direction, as detailed in Figure 80.

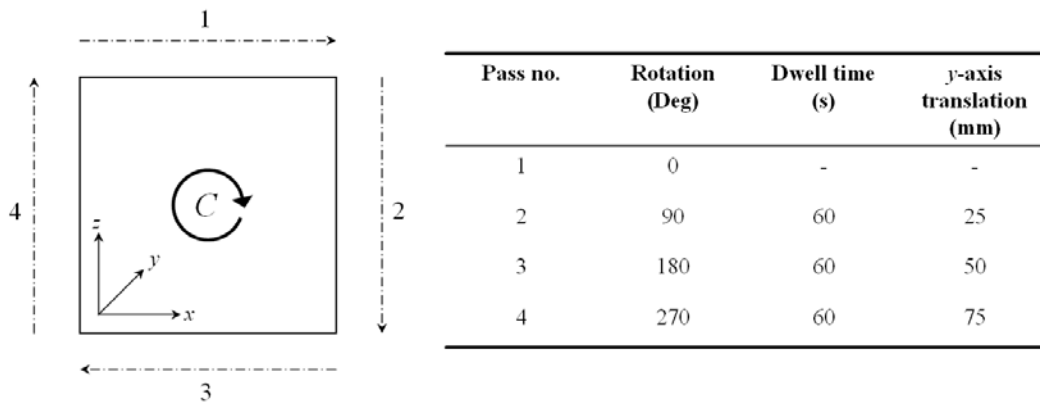


Figure 80 - Experimental scan strategy C. Dashed-dot lines represent irradiation path and direction.

A 3D profile of the formed component was obtained through use of a Faro Arm 3D profiling system, confirming the numerically predicted off axis twist in the component, as shown in Figure 81.

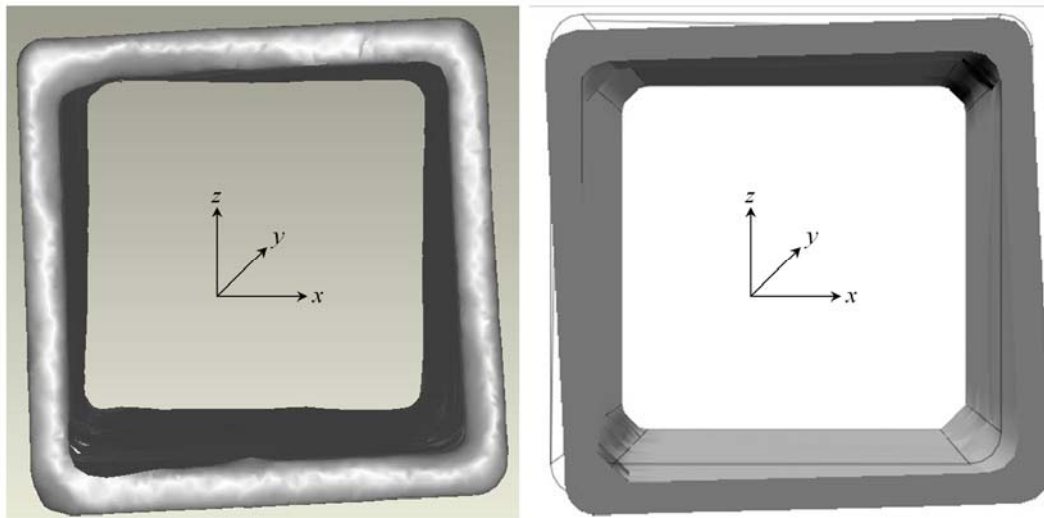


Figure 81 - Experimental (left) and simulated (right) total displacement at the end of the component (400 W, 8 mm beam diameter, 10 mm/s, 80% absorption).

It is worth noting that, in Figure 81, the experimental component was subject to 10 iterations of scan strategy C whereas in the FE simulation the strategy was applied only once. A deformation scale factor of 20x has therefore been applied to the simulated result for the purposes of comparison and in order to visualize the nature of the deformation more clearly.

Chapter 7

LASER MICRO-ADJUSTMENT USING SHORT AND ULTRA-SHORT PULSES

Microelectromechanical systems (MEMS) manufacturing requires accurate positioning and high reproducibility. Lasers can be utilised in accurate post-fabrication adjustment, allowing for manufacturing processes with relatively large tolerances. Laser micro forming (L μ F) is a process for the precision adjustment, shaping or correction of distortion in micro-scale metallic components through the application of laser irradiation without the need for permanent dies or tools. The non-contact nature of the process is also useful in accessing specific micro-components within a device which may be highly sensitive to mechanical force. As such it has potential for widespread application in both the manufacturing and microelectronics industry. Presented in this chapter is a novel technique for thermal L μ F involving picosecond duration pulses.

7.1 Introduction

When scaling down the LF process, limits to conventional thermal forming techniques become evident, such as excessive, non-localized heating of the substrate and long thermal relaxation times. Research has been conducted on non thermal L μ F techniques, such as laser shock micro-forming (LS μ F). Utilizing shockwaves generated through the breakdown of an absorptive layer, the LS μ F process induces compressive stresses in the materials upper surface, typically using nanosecond pulsed laser systems [14-16]. High repetition rate femtosecond pulsed systems have also been applied to the LS μ F process, producing bending away from the beam when used in conjunction with a pre-bend induced by favourable clamping conditions [17,18].

Thermal laser micro forming (L μ F) is a process for the precision adjustment, shaping or correction of distortion in micro-scale metallic components through the application of laser

radiation, without the need for permanent dies or tools. Providing the fluence (Φ) is below or close to the ablation threshold (Φ_{th}) of the material, short pulse laser systems have the potential to be used to form materials in a thermal process, broadly analogous to that of the TGM at macro scales. When the pulse duration is shorter than the lattice interaction time, as is often the case with sub nanosecond pulses, there is little conductive heat transfer into the bulk material. This confines the heating effect to the surface layer of the material, thereby selectively inducing plastic compressive stresses and avoiding excessive thermal loading of the substrate.

In this chapter, the mechanism by which deformation occurs in thermal L μ F is investigated both numerically and experimentally, with a focus on the effect of pulse duration, pulse overlap, laser power, traverse speed and irradiation strategy on the amount of deformation achieved.

7.2 Experimental

The experimental work presented in this chapter focuses on: (i) the manufacture of micro scale actuator style components; (ii) the exposure of these components to short pulse laser radiation at levels close to the ablation threshold; and (iii) the measurement of degree of bend (α_B) of the component as a function of pulse overlap, power and traverse speed (v_0).

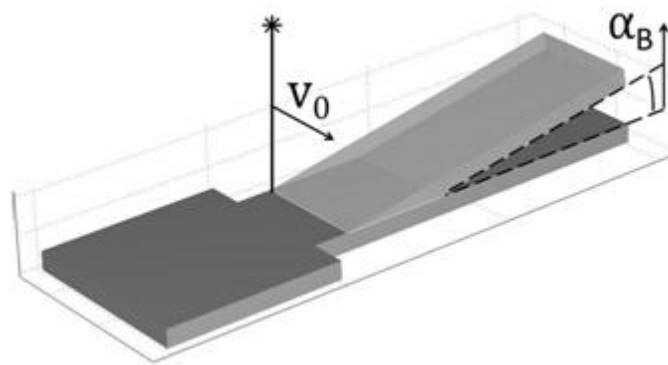


Figure 82 – Schematic illustration of the L μ F process.

7.2.1 Laser micromachining of actuator arms

MEMS-scale actuator arms were designed and micro-machined out of 50 and 75 μm thick AISI 302 stainless steel sheet (Table 6). Stainless steel was chosen as it is commonly used in micro-scale components [15,122]. As depicted in Figure 83, the actuator arms used in this study were 1000 x 300 μm in dimension.

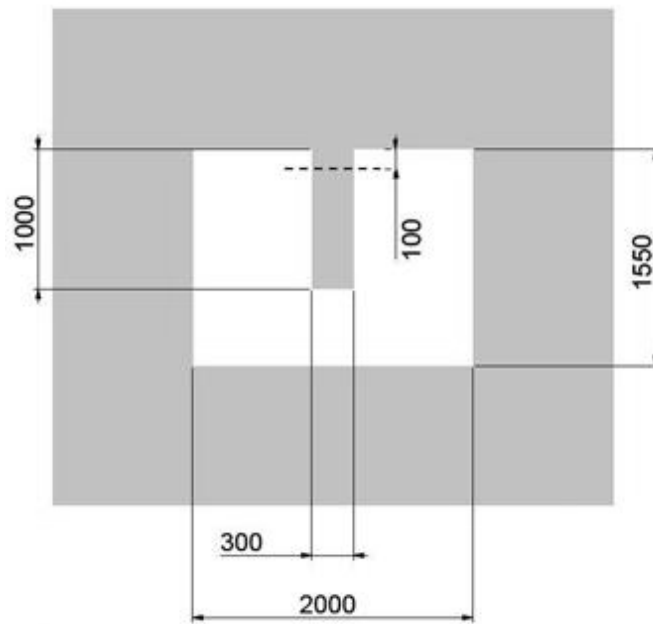


Figure 83 - Schematic of stainless steel AISI 302 actuator style arms, with dimensions in μm . The dashed line represents the irradiation path used in laser forming of the actuators.

α_{th}^* [1/K]	C_p^* [J/kg.K]	E [Pa]	E_{TISO} [Pa]	h [W/m ² K]	k^* [W/m.K]	ρ^* [kg/m ³]	σ_{ys} [Pa]	ν^* [1]
$17.2e^{-6}$	500	$1.93e^{11}$	3000	25	16.2	8000	$2.05e^8$	0.27

Table 6 - AISI 302 material properties at 298.15 K (* denotes properties which are considered temperature dependent in the simulations, see Appendix A for values).

The microactuator arms were fabricated using a High-Q IC-355-800 nm, 5 to 50 kHz laser operating at 1064nm. The laser parameters used were 5 kHz repetition rate, 300 mW average power, 50 mm/s traverse speed, 10 ps pulse length and a 35 μm spot diameter. A total of 600 and 800 overlapping scans were required for full penetration of the 50 and 75 μm thick steel sheets respectively. The degree of pulse overlap for this parameter set is illustrated in Figure 84.

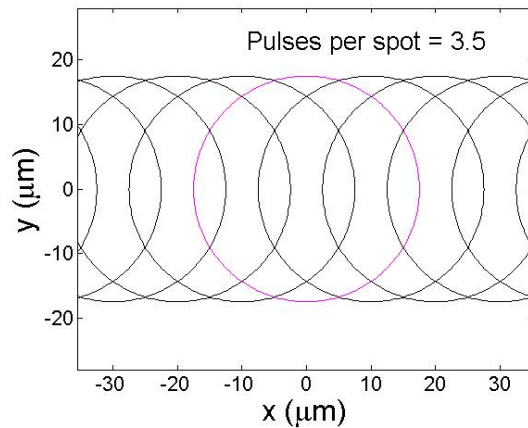


Figure 84 - Number of pulses per spot and degree of pulse overlap (35 μm beam diameter, 5 kHz repetition rate, 50 mm/s traverse speed).

The beam was expanded using a telescope then delivered to a scanning galvanometer with a 100 mm focal length f-theta lens, used to raster the beam over the workpiece. The beam was manipulated using SamLight (SCAPS GmbH) software, typically used in marking applications. In addition to the ability to raster the beam itself, the workpiece position could be manipulated using a 3-axis CNC stage (ATS115, Aerotech Ltd.), which had a resolution of 0.5 μm . The experimental set-up is depicted in Figure 85.

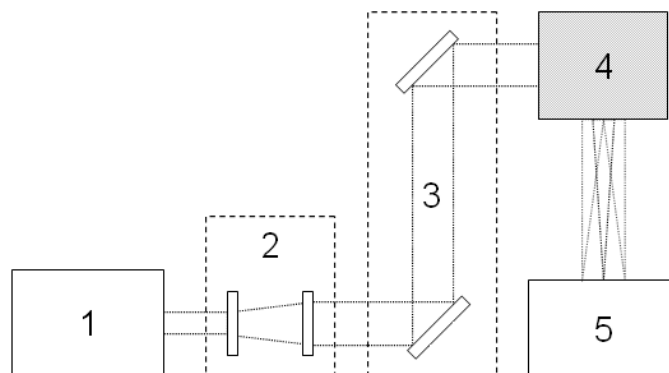


Figure 85 - The workpiece delivery set-up on the High-Q system: 1) laser source, 2) beam expander, 3) beam steering mirrors, 4) scanning galvanometer and 5) Aerotech 3-axis stage.

Twelve actuators were cut into each sample as four sets of three. Each set of three actuators was accompanied by a drilled hole of approximately 50 μm in diameter for alignment purposes (see Section 7.2.2).

The High-Q system was an ideal candidate for micromachining due to its ultra-short pulse length and low repetition rate. The short pulse length corresponds to a shorter heat diffusion depth (Equation 89, Figure 86) as well as a high intensity. Combined with a low repetition rate this ensures that any build up in temperature is highly localized and that micromachining proceeds predominantly by an ablative mechanism as opposed to melt and vaporisation.

7.2.2 Laser forming of actuators

An experimental study of L μ F was conducted using a 3W Fianium Yb-doped fibre TEM₀₀ laser with a pulse length of 20 ps, operating at between 1059 to 1069 nm wavelength and 500 kHz repetition rate. As depicted in Figure 83 the irradiation path was a straight line across the width of the actuator arm, 100 μ m from its base. The experimental set-up on the Fianium system was entirely analogous to that used on the High-Q system, as depicted in Figure 85. It should be noted that no absorptive coatings were used in this investigation.

The power was adjusted using an internal attenuator, controlled through the terminal software and measured using an external power meter which could be removed from the beam path when necessary.

The Fianium system was an ideal candidate for laser micro-adjustment due to its short pulse length and high repetition rate. The short pulse length corresponds to a low heat diffusion depth, Equation (90), in addition to a lower intensity when compared to the 10 ps High-Q system. Combined with a high repetition rate this ensures a significant yet highly localized build-up in temperature which is necessary for thermal micro-adjustment.

$$l = 2\sqrt{\alpha L_p} \quad (90)$$

Figure 86 shows that there is only a small penalty in terms of increased heat diffusion depth from approximately 30 to 40 nm when the pulse length is increased from 10 to 20 ps. However there is a relatively larger corresponding decrease in intensity.

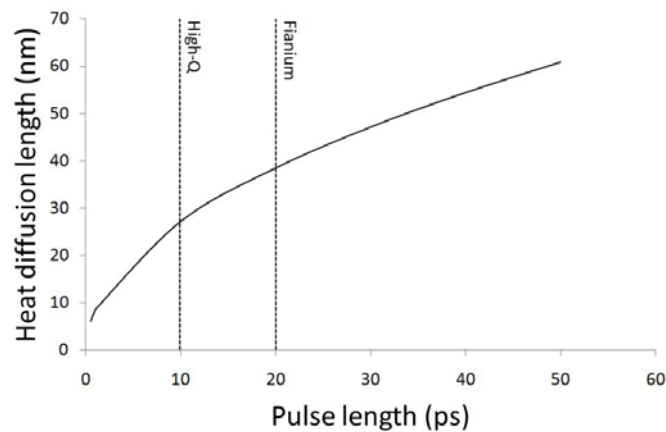


Figure 86 - Heat diffusion depth with increasing pulse length for AISI 302 stainless steel.

The actuators were clamped in place using a custom sample holder, consisting of two Aluminium framed Perspex grids which sandwiched the substrate between them, as shown in Figure 87. Perspex was chosen for the grid in order to rule out any conductive heat transfer from the substrate during processing. The sample holders' primary purpose was to aid in the alignment of the actuators for forming on the Fianium system. To this end, a ridge was included along one edge to ensure that the sample holder was identically aligned to the processing stage on both the High-Q and Fianium systems.

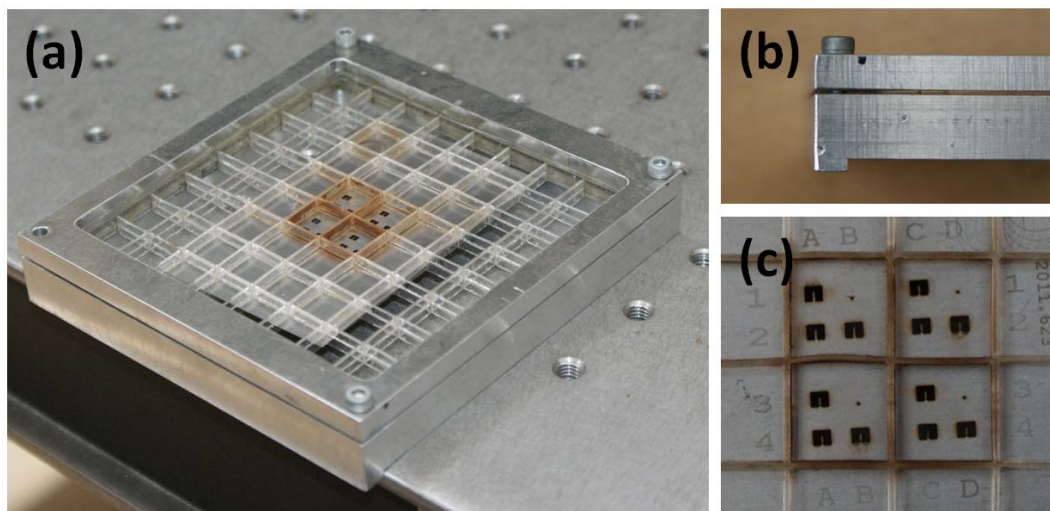


Figure 87 - Custom designed sample holder: (a) aluminium frame, (b) ridge used for alignment purposes and (c) Perspex grid and arrangement of actuator arms.

Accurate alignment was made possible due the aforementioned presence of holes drilled during fabrication of the micro-actuators on the High-Q system (see Section 7.2.1). With the laser power set to a minimum for plasma formation (approximately 300 mW) the software was set to drill mode and the shutter opened, producing a visible plasma on the substrate surface. By manipulating the stage in x and y until the small plasma produced by the laser was no longer visible (that is, the beam is focused over the hole) it was possible to align the workpiece by eye.

7.2.3 Measuring the deformation

The deformation induced was measured using a white light interferometer (WLI) (NT1100, Veeco Ltd.). The WLI produced z -height data for analysis either in the form of 2D cross sectional data or as a 3D visualisation, as shown in Figure 88.

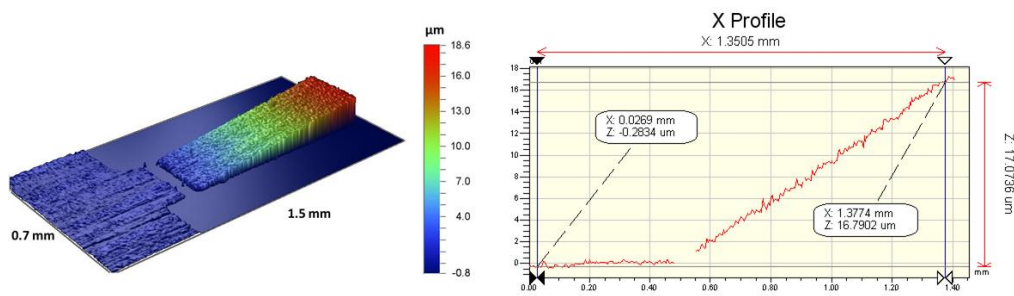


Figure 88 - Example output from Veeco NT1100 WLI.

This data was available for export in ASCII formatted data files. 2D cross-sectional z -height data was exported and post-processed through the use of a custom developed MATLAB graphical user interface (GUI) to determine the bend angle, a screenshot of which is shown in Figure 89.

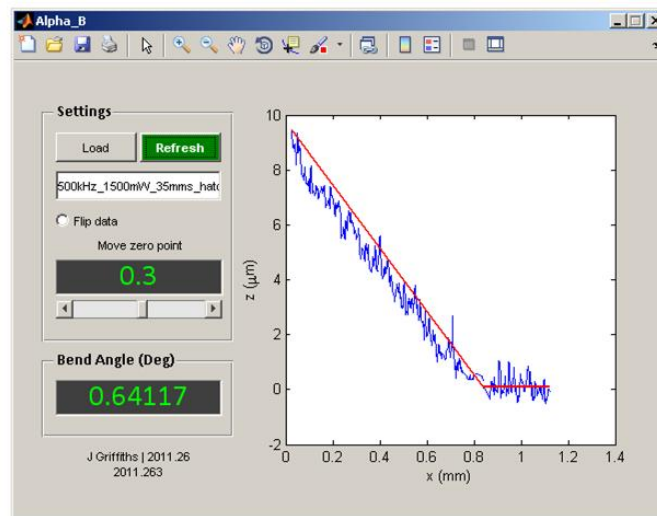


Figure 89 - Screenshot the Alpha_B MATLAB GUI.

7.2.4 FE model development

To fully understand the thermal aspects of the laser micro-adjustment process an FE model was developed. A 3256 element thermal simulation of the laser heating of $1000 \times 300 \times 50 \mu\text{m}$ AISI 302 stainless steel actuator arms, using a pulsed heat source was developed using COMSOL Multiphysics. The actual geometrical dimensions of the actuator were truncated to leave only the region of interest around the irradiation path as depicted in Figure 90. This was done in order to reduce the number of elements in the simulation, thereby reducing computational time.

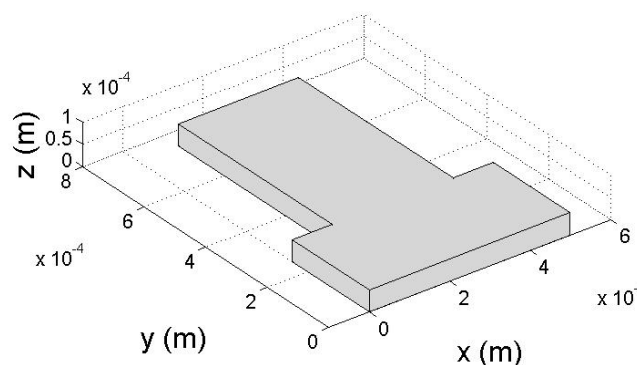


Figure 90 - Schematic of truncated stainless steel AISI 302 actuator style arms geometry used in FE simulations.

The mesh density was highest along the irradiation path, 100 μm from the base of the actuator arm, with the maximum element size being 10 μm . In addition, an even higher mesh density was assigned to the region of most interest at the centre of the irradiation path where most measurements were taken, in which the maximum element size was restricted to 2.5 μm , as shown in Figure 91.

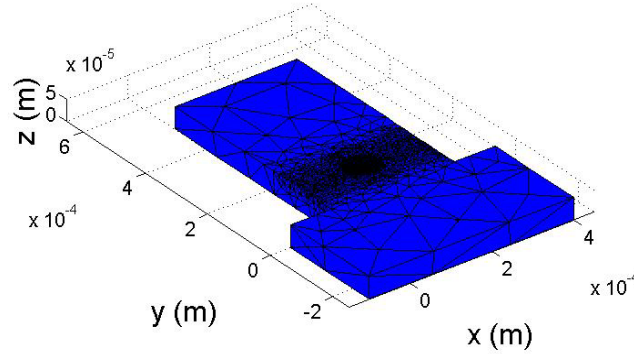


Figure 91 - Meshed geometry used in the FE simulations.

7.2.4.1 Modelling the heat source

The spatial distribution of the external heat source q_0 was considered to be an ideal Gaussian distribution (Equation 91), and was implemented in COMSOL as described in Section 5.2.2.1.

$$I = I_0 e^{-\left(\frac{2r^2}{\omega_0^2}\right)} = \frac{2E_p}{L_p \pi r^2} e^{-\left(\frac{2r^2}{\omega_0^2}\right)} \quad (91)$$

Where E_p is the pulse energy (J) and L_p is the pulse length (s). The intensity of the heat source was pulsed through the use of an interpolation function generated using a custom developed MATLAB GUI, shown in Figure 92. The GUI created a *.txt file in a directory which COMSOL read prior to each simulation. It consisted of a time-dependant Gaussian distributed pulse shape in which the relative intensity varied from 0 to 1, repeated at regular intervals as determined by the repetition rate of the laser. The intensity of the heat source in COMSOL was subsequently multiplied by these values.

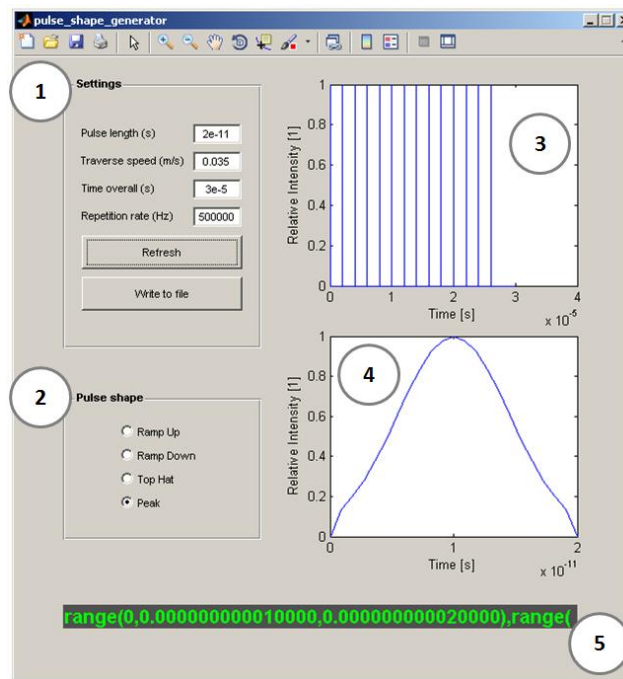


Figure 92 - Screenshot of the Pulse Shape Generator MATLAB GUI. 1) Laser process parameters, 2) Pulse shape settings, 3) Temporal pulsed relative intensity value plot, 4) Plot of individual pulse shape, 5) Initial section of MATLAB generated time list for use in COMSOL.

The MATLAB time list generated by the MATLAB GUI is discussed in detail in Section 7.2.4.3.

7.2.4.2 Modelling temperature dependant material properties

Temperature dependant material properties were modelled as described in Section 5.2.2.2. In addition the impact of phase change on the heat transfer analysis is considered due to the simulation of temperature cycles which exceed the melting temperature (T_m , 1693.15 K) of the steel substrate. During the phase transformation from solid to liquid during melting, energy from the laser heat source is imparted to the substrate. However, instead of creating a temperature rise, the energy alters the molecular structure of the material. To simulate this, the temperature dependant value for C_p can be approximated by:

$$\Delta C_p = \frac{\Delta H}{T} \approx C_p' = C_{p_{scalar}} + \frac{L_f}{T_m} H \quad (92)$$

where ΔH is change in enthalpy (J), L_f is the latent heat of fusion and H is a unit step function, applied when the local temperature is above that of T_m :

$$H = flc2hs(T - T_m, dT) \quad (93)$$

The term *flc2hs* refers to a built in COMSOL function for the smoothing of unit step functions. The term dT refers to half of the melting range of the material (27.5 K) and is the temperature range over which the step function is applied.

The temperature dependent absorption co-efficient was taken from literature (see Appendix B).

7.2.4.3 Solver settings

The solver chosen for the following simulations is the Direct (SPOOLES) linear system solver. The SPOOLES solver is ideal for this investigation as it is able to make use of the high degree of geometrical symmetry and the parabolic nature of the dominant PDE (the heat equation, Equation 28) to conserve computational resources.

Whereas the FE simulations previously documented in this thesis have used automatic time-stepping, in which the time steps are determined by the solver, the pulsed FE model required the implementation of manual time-stepping. Therefore the time steps taken by the solver are considered ‘strict’ and are predetermined by a time list, formatted as in the following example:

$$range(0,0.5,2) \quad (94)$$

where the simulation start time is 0, the step value is 0.5 and the overall solution time is 2. By selecting the strict time stepping option this simulation would have four time steps.

The strict time stepping is required in order to resolve phenomena that result from highly transient boundary conditions, in this case the pulsed laser heat source. If the solver were allowed to choose the time steps arbitrarily a change in the transient boundary condition could be ‘overstepped’ or skipped over.

One issue when manually inputting a time list is that the time step chosen in order to avoid overstepping a change in boundary condition may be excessively small (and therefore memory intensive) in the intervening period between, using this instance as an example, laser pulses. A 20 ps pulse duration requires approximately 1 ps time steps to resolve accurately. If the repetition rate is 500 kHz, however, the effective dwell time between pulses is 2×10^6 ps, necessitating a larger time step during these intervals. Therefore the time list must be composed of regions in which the time step is short (during the laser pulse) and relatively long (between pulses). This can be achieved through the application of multiple time lists:

$$\begin{aligned} & \text{range}(0, 1e-12, 2e-11), \text{range}(2e-11, 1e-6, 2e-6), \\ & \text{range}(2e-6, 1e-12, 2.0002e-6), \text{etc...} \end{aligned} \quad (95)$$

It is worth noting that whilst the time steps taken by the solver are strictly bound by the values in the time list, they represent the upper limit. Shorter time steps may be taken if deemed necessary by the solver, as shown in Figure 93.

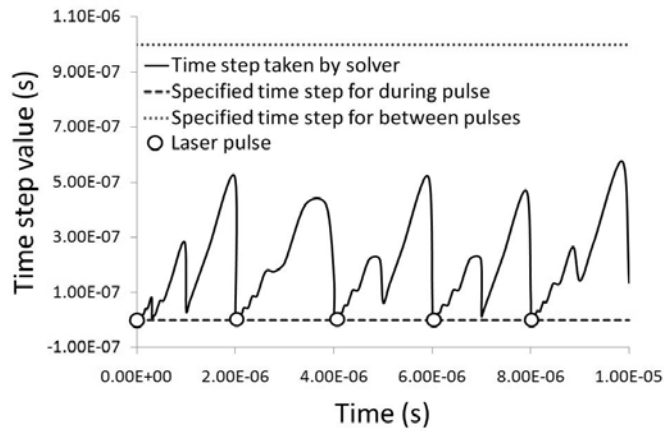


Figure 93 - Time steps taken by solver during pulsed laser simulation (500 kHz repetition rate).

7.3 Results and Discussion

7.3.1 Determination of ablation threshold

Prior to thermal L μ F being conducted the ablation threshold fluence (Φ_{th}) of the stainless steel substrate was determined experimentally [123] using the Fianium system, operating at 1059 to 1064 nm wavelength and 200 kHz repetition rate. The average power was varied in

50 mW intervals from 100 to 650 mW, with 12 holes drilled at each power. Dwell times of 2 ms and 3 ms were chosen to give 400 and 600 pulses per drilled spot respectively. The diameter D of the ablated craters was measured using WLI.

The beam radius ω_0 was determined from a plot of D^2 against E_p and found to be 14.7 μm . Using this value the fluence could be determined, and the x -intercept of a logarithmic trend line from a plot of D^2 against Φ_0 , plotted on a Log_{10} scale, was taken as Φ_{th} (see Figure 94). This was found to be 0.09 J/cm² and 0.08 J/cm² for 400 and 600 pulses, respectively. Equation 96 describes the relationship between peak fluence, Φ_0 , and E_p , whilst D is related to Φ_0 according to Equation 97.

$$\Phi_0 = \frac{2E_p}{\pi\omega_0^2} \quad (96)$$

$$D^2 = 2\omega_0 \ln \left[\frac{\Phi_0}{\Phi_{th}} \right] \quad (97)$$

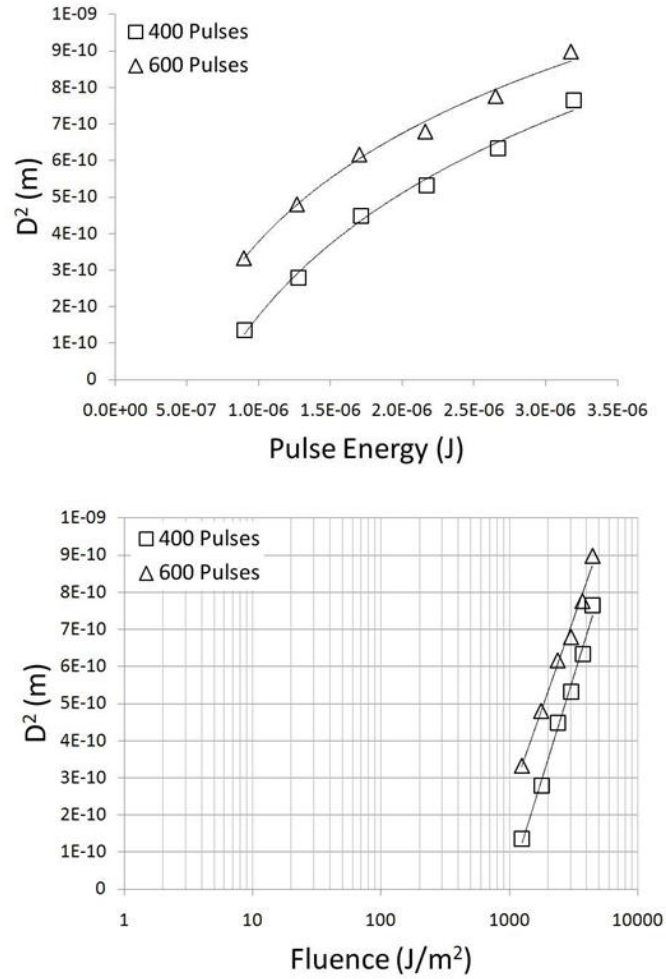


Figure 94 - D^2 against E_p (top) and D^2 against Φ_0 , plotted on a Log_{10} scale (bottom).

7.3.2 Effect of pulse duration

As previously mentioned, a pulsed laser source was chosen in order to limit the thermal loading of the bulk of the substrate. Due to the small size of the component and short processing time it is difficult to determine the transient thermal flux empirically in this

instance. To overcome this challenge, FE simulations were used. Figure 95 depicts the transient temperature at the centre of the irradiation path for a CW heat source.

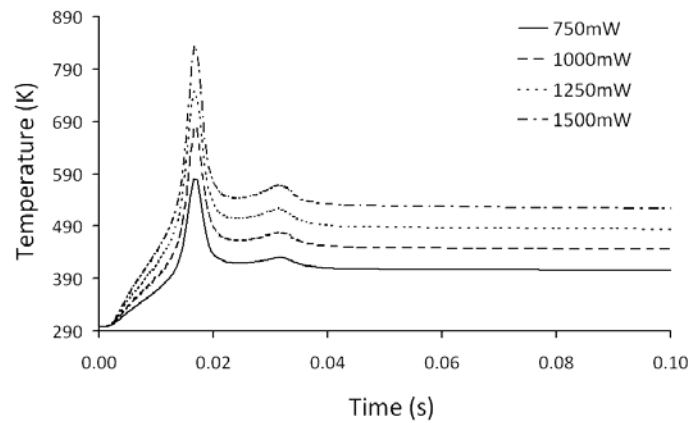


Figure 95 - Simulated temperature at the centre of the irradiation path and at four powers (1000 x 300 x 50 μm stainless steel AISI 302, 1500 mW, 35 μm beam diameter, continuous wave, 35 mm/s traverse speed).

The effectively constant temperature profiles observed after 0.04 s in Figure 95 reveal that, whilst peak temperatures at which deformation could occur are achieved, thermal loading of the bulk substrate restricts the ability of the substrate to dissipate heat away from the irradiation zone, cooling of which is essential for the establishment of a suitable temperature gradient upon subsequent irradiation. As discussed in Section 1.2.1, cooling of the irradiated area in LF proceeds predominantly by a process of self quenching, in which heat is transferred to the cold surrounding material by conduction. As the temperature gradient between the irradiated area and the cold surrounding material is reduced the self quenching ability of the component is diminished. The near homogeneous residual build up in temperature after a single pass for a CW heat source is depicted in Figure 96.

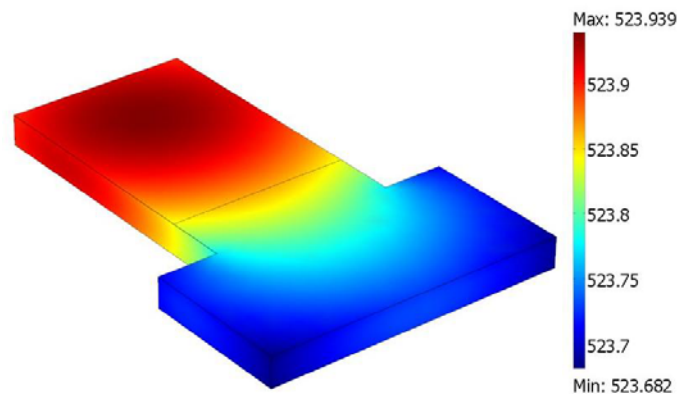


Figure 96 – FE simulated temperature (K) after a single irradiation of the geometry (1000 x 300 x 50 μm stainless steel AISI 302, 1500mW, 35 μm beam diameter, continuous wave, 10 mm/s traverse speed).

Depending on the duration of the rest time between irradiations, the build up in temperature in the bulk substrate shown in Figure 96 has the potential to significantly diminish the temperature gradient achievable between the top and bottom surfaces upon subsequent irradiation, key to the TGM mechanism. This requirement for relatively long rest times when compared with short and ultra-short pulsed laser sources (see Section 7.3.3) makes CW laser sources unsuitable for L μ F applications.

The application of femtosecond pulsed laser systems in the L μ F process was investigated using a Clark-MXR CPA2010 which had a central wavelength of 775 nm, fixed repetition rate of 1 kHz, maximum pulse energy of approximately 1 mJ and a temporal pulse length 240 fs. This system was capable of both fabricating and subsequently processing the actuators. However, it was found that due to ultra-short pulse duration the intensity was more than sufficient to ablate the substrate with minimal heat accumulation. Figure 97 reveals the machining of a deep ablation groove along the irradiation path and no appreciable deformation.

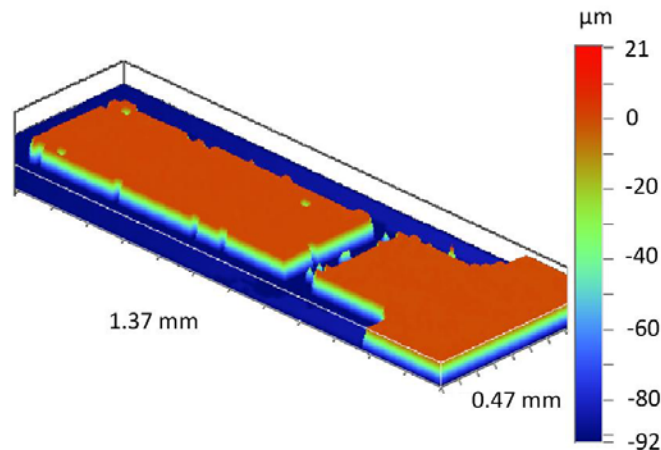


Figure 97 - WLI image showing deformation of an actuator arm after 10 irradiations (1000 x 300 x 50 μ m stainless steel AISI 302, 0.02 W average power, 30 μ m beam diameter, 1 kHz repetition rate, 10 mm/s traverse speed).

Whilst desirable during the fabrication process, the lack of heat accumulation makes femtosecond pulse duration laser systems unsuitable for use in the thermal L μ F process. It is worth noting however that high repetition rate (>100 kHz) femtosecond systems have been successfully applied to the LS μ F process, producing bending away from the beam, often requiring a pre-bend induced by favourable clamping conditions [17,18].

Low picosecond pulse durations close to the threshold between short and ultra-short pulse lengths (approximately 10 to 20 ps) have the potential to be utilized in thermal L μ F as they offer limited heat diffusion depths but still induce heat conduction into the lattice, resulting in localized heating of the component without excessive thermal loading, as detailed in the following subsections.

7.3.3 Effect of repetition rate

Multi-pass thermal L μ F was conducted using the Fianium system. As detailed in Section 7.2.2, the irradiation path was 100 μ m from the base of the arms. Ten successive irradiations were applied at repetition rates of 200 kHz and 500 kHz whilst keeping the pulse energy constant at 3 μ J, as shown in Figure 98.

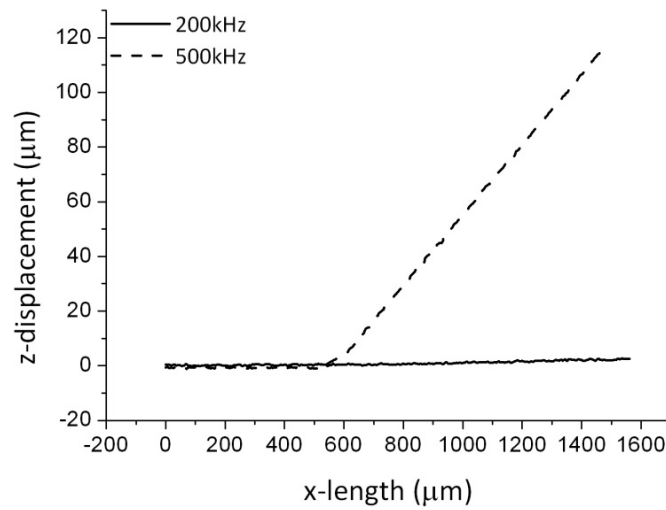


Figure 98 - Profile view of z -deformation after 10 irradiations at 200 and 500 kHz repetition rate and $3\mu\text{J}$ pulse energy ($1000 \times 300 \times 50\mu\text{m}$ stainless steel AISI 302, $35\mu\text{m}$ beam diameter, 10 mm/s traverse speed).

Figure 98 reveals little or no deformation at 200 kHz but significant deformation at 500 kHz, suggesting the latter is the more suitable repetition rate for the laser micro-adjustment process. This can be attributed to the relatively larger cumulative build up in temperature at higher repetition rates due to reduced dwell time between pulses, as shown in Figure 99.

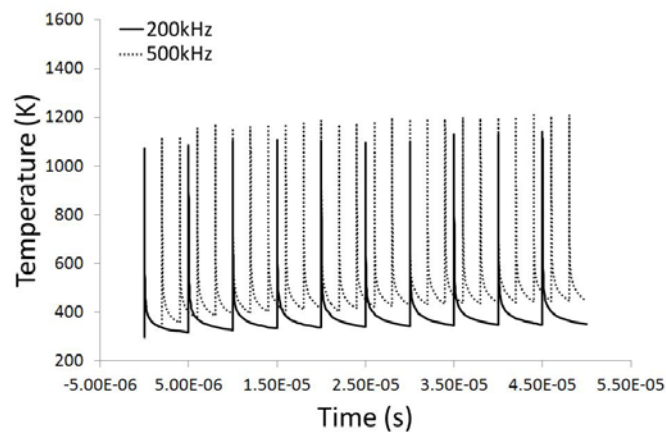


Figure 99 - FE simulation of temperature directly beneath the beam for a stationary laser heat source at 200 kHz and 500 kHz ($1000 \times 300 \times 50\mu\text{m}$ stainless steel AISI 302, $3\mu\text{J}$ pulse energy, $35\mu\text{m}$ beam diameter).

7.3.4 Laser micro-forming using picosecond pulse durations

Multi-pass L μ F was conducted using the Fianium system, operating at 1059 to 1064 nm wavelength and 500 kHz repetition rate with a spot diameter of approximately 35 μ m. With increasing multiple irradiations a cumulative increase in bend angle was observed, as shown in Figure 100.

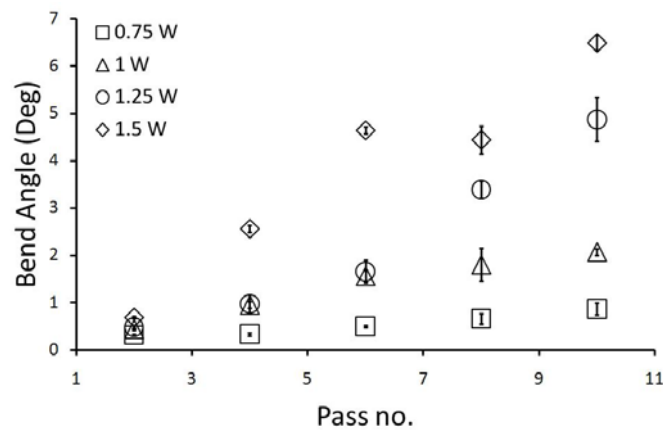


Figure 100 - Cumulative bend angle variation with successive irradiations (1000 x 300 x 50 μ m stainless steel AISI 302, 35 μ m beam diameter, 500 kHz repetition rate, 10 mm/s traverse speed).

In addition to a cumulative increase in bend angle, an ablated groove was also observed along the length of the scan path, the aspect ratio of which became too large to resolve the depth by WLI after multiple irradiations, as shown in Figure 101.

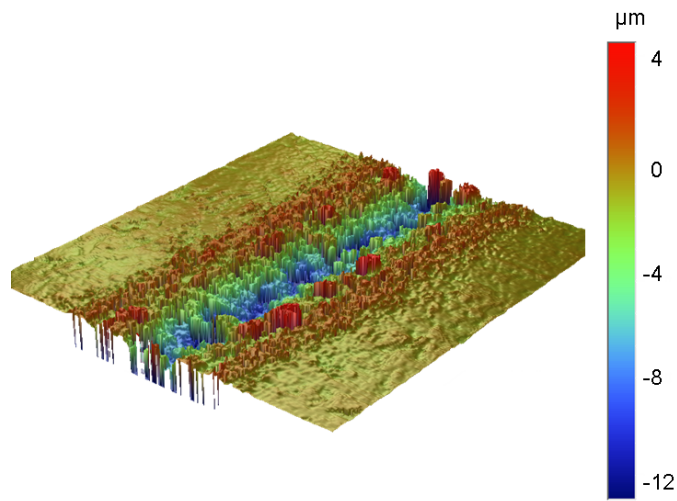


Figure 101 - WLI image of ablated groove after 6 irradiations (1000 x 300 x 50 μm stainless steel AISI 302, 1500 mW, 35 μm beam diameter, 500 kHz repetition rate, 10 mm/s traverse speed).

This ablated groove can be attributed to the use of multiple irradiations in conjunction with fluences above those of the experimentally determined values of Φ_{th} . An experiment was subsequently conducted in which the traverse speed was increased and the ablated groove depth and bend angle was monitored, the results of which are shown in Figure 102.

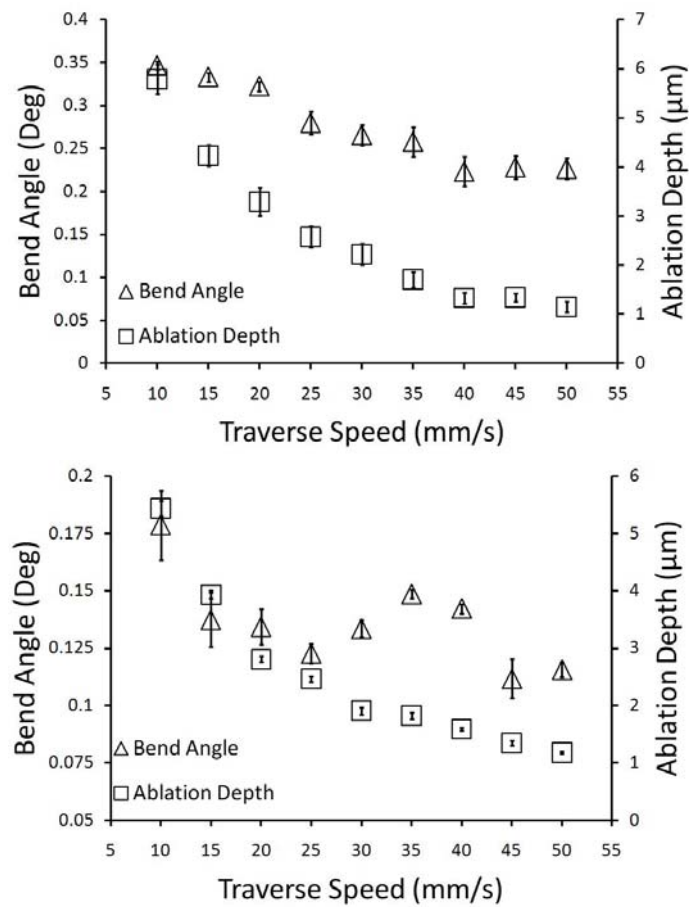


Figure 102 - Bend angle and ablation depth variation with increasing speed, 50 and 75 μm thickness top and bottom respectively (1000 x 300 μm stainless steel AISI 302, 35 μm beam diameter, 500 kHz repetition rate, 1.5 W average power).

From Figure 102 it is evident that the ablated groove has a detrimental effect on bend angle up to a point, in this instance when deeper than approximately 2 μm . The optimum traverse speed at which a suitable combination of bend angle and z-depth was achieved was found to be 35 mm/s, with the degree of pulse overlap illustrated in Figure 103.

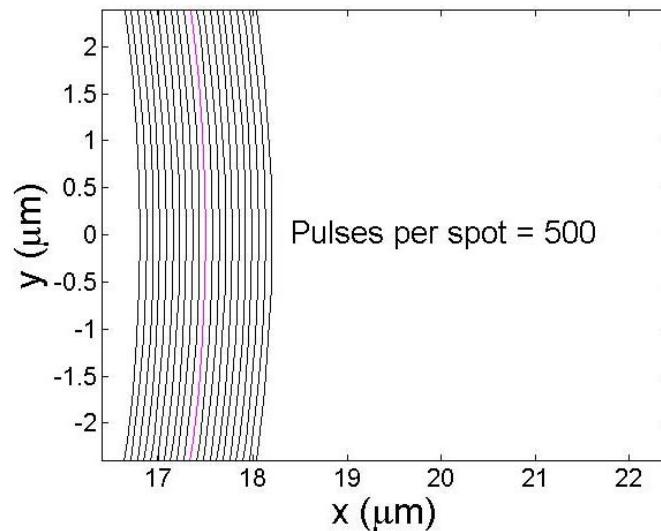


Figure 103 - Number of pulses per spot and degree of pulse overlap (35 μm beam diameter, 500 kHz repetition rate, 35 mm/s traverse speed).

Whilst it was possible to limit the ablation depth for single scans, multiple irradiations resulted in an increase in ablation depth. This phenomenon could be attributed to a conditioning of the irradiated surface after an initial irradiation [124], increasing the absorption for subsequent scans.

As highlighted in Figure 100, multiple irradiations were essential to achieving a large range of deformation. As such an alternative to multiple irradiations along a single path was required to obtain a variation in bend angle. One such method investigated involved a combination of varying power and a hatched scan strategy. The hatch consisted of four single irradiation paths, scanned sequentially in alternate directions. Each irradiation path was spaced 30 μm apart, allowing for little or no overlap, as shown in Figure 104.

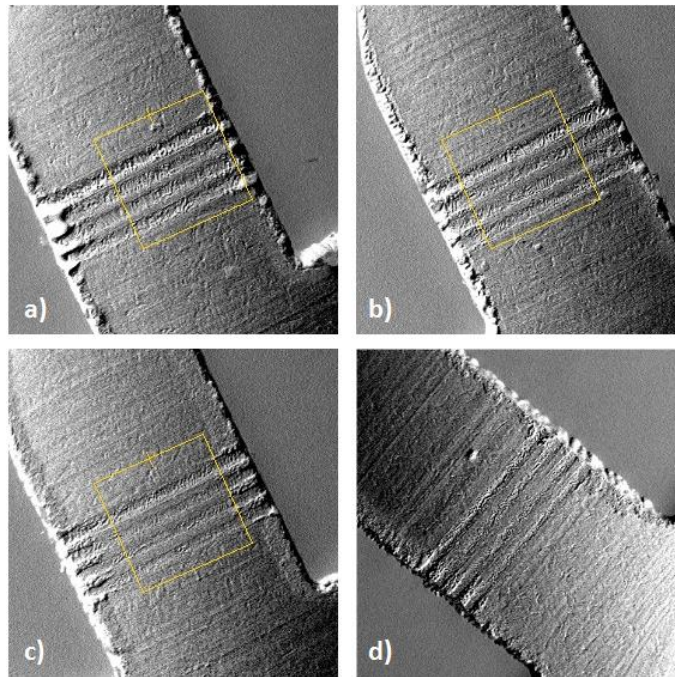


Figure 104 - Scanning electron microscope image of ablated groove after hatch irradiation strategy at a) 1500 mW, b) 1250 mW, c) 1000 mW and d) 750 mW (1000 x 300 x 50 μm stainless steel AISI 302, 35 μm beam diameter, 500 kHz repetition rate, 35 mm/s traverse speed).

From Fig 104 it is evident that melt and re-solidification has occurred in the irradiated areas, becoming more noticeable with increasing laser power. This has also been observed by Singh *et al.* [99,125] upon the application of high intensity, low repetition rate nanosecond pulsed radiation to magnetic sliders in hard disk drives. It should be noted that the stress induced by this melt and re-solidification has the potential to contribute to the net bending angle.

Through variation of laser power with a single line scan strategy, controlled and repeatable micro-adjustment was achieved. The application of a hatched scan strategy increased the range over which micro-adjustment could be achieved whilst keeping the ablated groove to within approximately 2 μm depth, as shown in Figure 105.

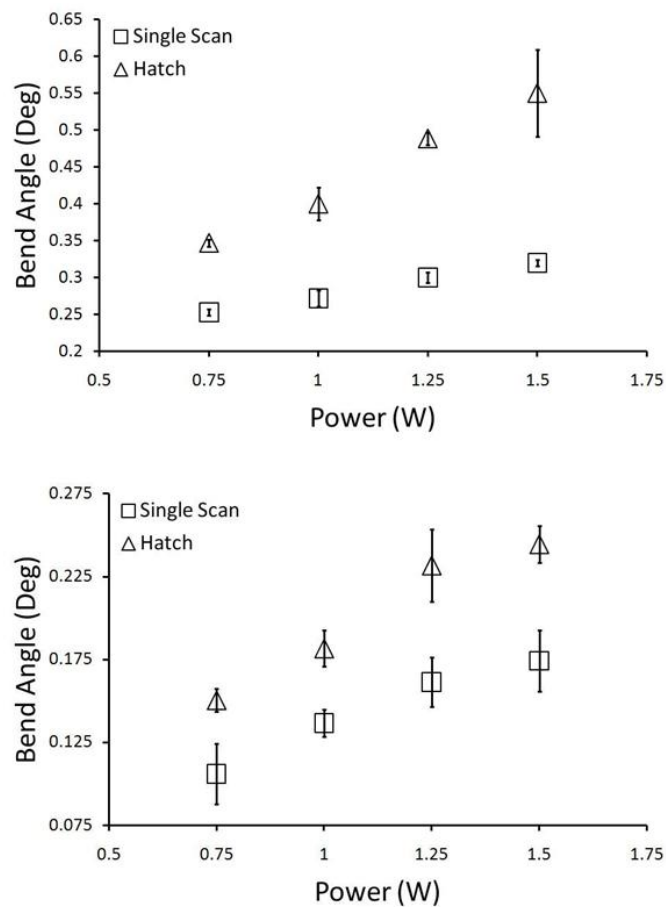


Figure 105 - Bend angle variation with increasing power, 50 and 75 μm thickness top and bottom respectively (1000 x 300 μm stainless steel AISI 302, 35 μm beam diameter, 500 kHz repetition rate, 35 mm/s traverse speed).

In this chapter, thin sheet thermal L μ F for the micro-adjustment of actuator style components was demonstrated using picosecond duration pulses with no absorptive coatings required. A full empirical study was conducted, with the effect of pulse overlap, laser power and irradiation strategy investigated.

The thermal L μ F technique presented in this chapter combines short pulse durations with high repetition rates and offers a method of generating localized heat build-up on the top surface of micro-scale components, allowing for controlled and repeatable micro-adjustment. Through a combination of irradiation strategies a large range of deformation is achievable, as shown in Figure 105.

The use of 20 ps pulse durations limits the heat diffusion depth to within a suitable range (i.e. half the sheet thickness) on the top surface of the component, whilst not being so short as to cause significant material removal by ablation. It was found that the repetition rate and therefore degree of pulse overlap must be high enough to ensure sufficient build up in temperature on the surface of the component for thermal forming.

The process has significant potential for the post-fabrication micro-adjustment of functional components in micro-electronic devices. Challenges include minimising ablation along the irradiated scan path and obtaining a larger range of deformation through optimized process parameters.

Conclusions

1. Factors affecting bend angle per pass

Analytical and numerical modelling of the LF process was used to ascertain which of the various factors identified (thermal effects, geometrical effects, variation in absorption, metallurgical effects) contribute towards variation in bend angle per pass with multiple irradiations and subsequently the magnitude of their contribution.

Thermal effects were found to be confined to the early stages of the process, becoming less influential as thermal equilibrium is reached, providing suitable processing parameters are chosen. This combination of parameters was found to be strongly affected by substrate material properties, most notably the thermal diffusivity; that is the materials ability to dissipate heat away from the irradiated area.

Numerical simulations in which thermal conductivity, specific heat capacity and thermal expansion co-efficient were varied independently of one another revealed that, over the first six passes in multiple scan LF, a lower thermal diffusivity resulted in a greater cumulative bend angle. This was attributed to a reduction in the flow stress of the component as a result of heat accumulation between laser scans.

Geometrical effects are an important consideration when considerable deformation is desired, as the beam shape impinging on the workpiece becomes more elliptical with increasing bend angle. FE simulations were developed in which the variation energy density as a result of the impinging beam geometry was simulated for single line laser forming in an edge-clamped cantilever arrangement. It was found that significant reductions in bend angle (that is, greater than 20%) occurred at bend angles greater than approximately 35° as a result of significantly reduced energy densities.

Absorption effects were found to become dominant later in the process, with increasing deformation and graphite burn-off respectively. The effect of graphite coating degradation in multi-pass LF was investigated both experimentally and numerically, with particular

emphasis placed on its effect on bend angle *per* pass due to variation in laser radiation absorption.

It was found that the detrimental effects of graphite burn-off were lessened by a darkening of the surface, similar to that observed in laser marking, effectively reducing its reflectivity and increasing the coupling efficiency for laser radiation absorption.

Any **metallurgical effects** of the LF process could have significant ramification on the subsequent performance of the part, necessitating accurate methods for the prediction of such effects. It was found that, whilst some combinations of process parameters offered significant deformation (*e.g.* high powers/low speeds) and no melting, the potential for austenitic transformation during laser heating and subsequent martensitic transformation upon cooling was increased. Using the models presented the suitability of process parameter combinations with regards to undesirable metallurgical transformations could be assessed numerically.

FE simulations were also used to analyse the development of undesirable asymmetric **edge effects** in 2D LF, and subsequently to devise new scan strategies to eradicate them.

A simple scan strategy in which the beam traverse speed increased at the mid-point of the sheet was used, reducing the amount of heat the leaving edge was required to dissipate and reducing asymmetry along the edge of the component. Analogous experimentation was conducted in which validated the predictions from these simulations.

2. LF of square section mild steel tubes

In work conducted in conjunction with Honda Engineering Europe Ltd, the applicability of the LF process in the axial bending and in plane ‘twisting’ of square section mild steel tubes for the automotive industry was investigated.

The work took the form of an initial feasibility study, with the following deliverables:

- Demonstrate out of plane bending around a central axis, ideally in the order of degrees, with special consideration given to:
 - Throughput and processing time.

- Pre and post-processing requirements, such as absorptive coatings and subsequent coating removal.
- Demonstrate in-plane ‘twisting’ of the component around a central axis.

Using the coupled analytical and numerical models detailed in Chapter 4 and implemented in Chapter 5, numerical simulations incorporating the square section tube geometry were conducted, the aim of which was to develop a scan strategy capable of inducing axial bending of the component towards the beam.

The scan strategy devised consisted of an in-plane shortening mechanism on three sides of the component, utilizing process parameters commonly associated with the buckling or upsetting mechanism. The result was a tapered compression of the component around a central axis, resulting in an out of plane bend towards the beam.

Optimal process parameters were predicted using the FE simulations and, in some instances, refined when validation was carried out experimentally. Consideration was given to both the propensity for microstructural change and carbon diffusion from the absorptive coating into the surface. The appearance of the HAZ was used to assess the suitability of the FE predicted process parameters.

The FE models were also used to develop a scan strategy for the in plane twisting of the component, which utilized the same approach of in-plane shortening used for axial bending. This was also demonstrated experimentally for validation purposes, with excellent qualitative agreement between the simulated and experimental deformation observed.

3. Short and ultra-short pulse micro-adjustment

Thin sheet L μ F for the micro-adjustment of actuator style components was conducted using picosecond duration pulses, with no absorptive or confining layers required. To fully understand the thermal aspects of the L μ F process, a thermal FE simulation was developed which incorporated a pulsed heat source.

This entirely novel technique combines short pulse durations with high repetition rates and offers a method of generating localised heat build-up on the top surface of micro-scale components, allowing for controlled and repeatable micro-adjustment.

A relatively large range of deformation was found to be achievable through a combination of hatched and single line irradiation strategies, varying laser power and traverse speeds.

Extensive empirical studies were conducted, with an emphasis on the use picosecond pulse durations in L μ F. The use of 20 ps pulse durations limited the heat diffusion depth to within a suitable range (that is, half the sheet thickness, see Sections 7.2.2 and 7.3.1.1) on the top surface of the component, whilst not being so short as to cause significant material removal by ablation. It was found that the repetition rate and therefore degree of pulse overlap must be high enough to ensure sufficient build up in temperature on the surface of the component for thermal forming, as indicated by experimental observations and affirmed by the results of thermal FE simulations.

Figure 107 compares both the relative aspect ratio (that is, depth multiplied by width) of formed components and maximum bend angle reported for those investigations detailed in Chapter 3, as well as for the work in this thesis. From Figure 106, the comparatively small scale of the formed component and relatively large range of deformation achieved in thermal L μ F using picosecond pulse durations is evident.

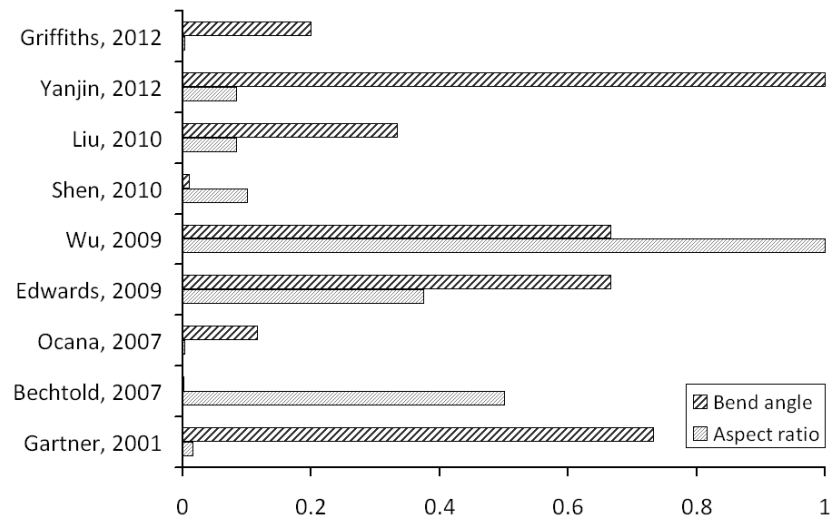


Figure 106 - Relative range of deformation and aspect ratio of components.

Future Work

1. Macro scale

1.1 Finite element modelling of laser forming

A key focus of future work on the model detailed in Chapter 4, Section 4.1 would be the integration of the numerical diffusion and analytical phase transformation models into the FE simulations. This would allow the user to post-process and visualize diffusion and transformation phenomena in 3D as a part of the specified geometry. In addition, it would increase the accuracy of the coupling between the phenomena, *e.g.* between thermal properties and the co-efficient of diffusion in the carbon diffusion FD simulation.

With increasing computational power, ever more accurate simulations are possible. This offers the modeller the potential to couple more and more distinct physical phenomena into a single simulation of a process. In the authors' opinion, the computational fluid dynamics (CFD) module (alongside the Heat Transfer and Structural Mechanics modules) is the next logical addition to the simulation of the LF process. Addition of this module would provide the opportunity to accurately model:

- Viscous forces in the melt pool during laser heating, although sub-melting temperatures are desirable during LF.
- Non-laminar flow at boundaries, particularly useful in modelling the effect of forced convective cooling or of assist/shroud gas jets emanating from the processing nozzle.

The development of residual stresses during multi-pass LF of complex geometries and their effect on deformation resulting from subsequent irradiations was a recurring theme at the IWOTE '11 conference on thermal forming in Bremen, Germany [126]. The effect of residual stresses in laser welded components on the correction of distortion by LF also featured prominently.

Numerical models could be used to develop scan strategies for closed loop systems in iterative LF of complex geometries, taking into account the effect of simulated residual stresses when determining the optimum scan strategy for each iteration.

For correction of distortion in laser welded components, experimentally determined stress fields could be incorporated into the model prior to simulation in order ascertain the magnitude of influence they had on the nature of deformation for given scan strategies.

1.2 Laser forming of square section mild steel tubes

A key aim of any further investigation would be process parameter optimization for increased throughput times. Primarily entailing numerical simulations, the aim of such investigation would be to establish combinations of power and spot size which satisfy the conditions for in-plane shortening when used in conjunction with high traverse speeds. For validation purposes, this would also require improvements to be made to the experimental set-up, specifically an increased speed of component rotation.

In addition, the following suggestions are made for further investigation:

- A full metallurgical study to validate the analytical and numerical predictions for phase transformation and diffusion of carbon from the absorptive graphite coating.
- The development of a closed loop control system for the correction of distortion in mechanically formed components. Based on an iterative approach, this would entail the profiling of the geometry both initially and after each application of the laser, with appropriate process parameters and scan strategies determined by algorithm, specifically tailored to the newly formed component geometry.

Whilst the aims of this feasibility study were fairly modest, FE modelling has the potential to be used in further process optimization. For instance, in the simulations detailed in Chapter 6 constant traverse speeds were used for simplicity due to the difficulty in implementing variable traverse speeds experimentally. However, variable traverse speeds offer the potential to enhance the in plane tapered compression required for the axial bending of square section tubes, with FE modelling being the ideal candidate for a cost-effective parametric study into this.

2. Micro scale

The L μ F process has significant potential for the post-fabrication micro-adjustment of functional components in micro-electronic devices, as illustrated in Figure 107.

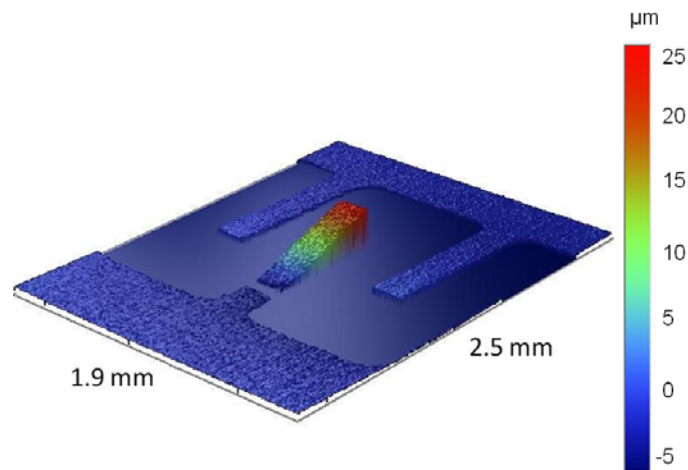


Figure 107 - WLI image of deformed actuator arm in a comb drive arrangement.

Challenges include minimising ablation along the irradiated scan path and obtaining a larger range of deformation through optimized process parameters.

In order to fulfil its potential in a micro-electronics manufacturing environment, empirical and numerical studies into L μ F of further miniaturised components are essential. This will require the design of systems for the accurate alignment of the beam on the workpiece. In addition, the inclusion of in-process monitoring of deformation would be essential to the creation of an automated closed loop system for the micro-adjustment of or correction of distortion in MEMS components.

Further numerical investigation of the L μ F process is essential in establishing the mechanism of deformation. Whilst the limited scope of the numerical modelling of pulsed laser heating presented in this thesis is useful in alluding to the possible mechanism by which deformation occurs, optimization of computational resource usage would enable full thermal-mechanical modelling of process. Such modelling would further the understanding of the key driving forces behind the mechanism, significantly aiding process development.

Also, joule heating models [127], which estimate the extent to which the temperature of the electrons are heated with respect to the metal lattice, would provide insight into the possible use of sub-picosecond, ultra-short pulse durations in L μ F.

References

- [1] Geiger M, Vollertsen F. The Mechanisms of Laser Forming. CIRP ANNALS 1993;42:301.
- [2] Magee J, Watkins KG, Steen WM. Advances in laser forming. Journal of Laser Applications 1998;10(6):235.
- [3] Di Pietro P, Yao YL. An investigation into characterizing and optimizing laser cutting quality — A review. Int J Mach Tools Manuf 1994 2;34(2):225-243.
- [4] Dubey AK, Yadava V. Laser beam machining—A review. Int J Mach Tools Manuf 2008 5;48(6):609-628.
- [5] Kaebernick H, Bicleanu D, Brandt M. Theoretical and Experimental Investigation of Pulsed Laser Cutting. CIRP Ann Manuf Technol 1999;48(1):163-166.
- [6] Noor YM, Tam SC, Lim LEN, Jana S. A review of the Nd: YAG laser marking of plastic and ceramic IC packages. J Mater Process Technol 1994 4;42(1):95-133.
- [7] Alexander DR, Khlif M-. Laser marking using organo-metallic films. Optics and Lasers in Engineering 1996 7;25(1):55-70.
- [8] Thomas H. Development of irradiation strategies for 3D-laser forming. J Mater Process Technol 2000 6/1;103(1):102-108.
- [9] Dearden G, Edwardson SP. Some recent developments in two- and three-dimensional laser forming for ‘macro’ and ‘micro’ applications. J Opt A: Pure Appl Opt 2003;5:8.
- [10] Homan HS, Sirignano WA. Minimum mass of burning aluminum particles for ignition of methane/air and propane/air mixtures. Symp Int Combust 1981;18(1):1709-1717.
- [11] Dirscherl M, Esser G, Schmidt M. Ultrashort Pulse Laser Bending. Journal of Laser Micro/Nanoengineering 2006;1(1).

- [12] Vollertsen F, Sakkiettibutra J. Different types to use laser as a forming tool. *Physics Procedia* 2010;5, Part B(0):193-203.
- [13] Steen WM, Mazumder J. *Laser Materials Processing*. 6th ed.: Springer; 2010.
- [14] Zhou JZ, Liu HX, Yang CJ, Cao XG, Du JJ, Ni MX. Non-Traditional Forming Process of Sheet Metal Based on Laser Shock Waves. *Key Engineering Materials* 2007;329:637.
- [15] Ocaña JL, Morales M, Molpeceres C, García O, Porro JA, García-Ballesteros JJ. Short pulse laser microforming of thin metal sheets for MEMS manufacturing. *Appl Surf Sci* 2007 12/15;254(4):997-1001.
- [16] Edwards K, Edwardson S, Carey C, Dearden G, Watkins K. Laser micro peen forming without a tamping layer. *The International Journal of Advanced Manufacturing Technology* 2010;47(1):191-200.
- [17] Sagisaka Y, Kamiya M, Matsuda M, Ohta Y. Laser Peen Forming with Femtosecond Laser - Influences of Irradiation Conditions and Prebending on Thin-Sheet-Metal Bending. *Journal of the Japan Society for Precision Engineering* 2009;75(12):1449.
- [18] Sagisaka Y, Kamiya M, Matsuda M, Ohta Y. Thin-sheet-metal bending by laser peen forming with femtosecond laser. *J Mater Process Technol* 2010 11/19;210(15):2304-2309.
- [19] Edwardson S, Griffiths J, Edwards K, Dearden G, Watkins K. Laser forming: overview of the controlling factors in the temperature gradient mechanism. *Proc Inst Mech Eng Part C* 2010;224(5):1031-1040.
- [20] Holt RE. Primary Concepts for Flame Bending. *J Welding* 1971;50(6):416.
- [21] Moshaiov A, Vorus WS. The Mechanics of the Flame Bending process: Theory and Applications. *Journal of Ship Research* 1987;31(4):13.
- [22] Hemmati SJ, Shin JG. Estimation of flame parameters for flame bending process. *Int J Mach Tools Manuf* 2007 4;47(5):799-804.
- [23] Klemens PG. Heat balance and flow conditions for electron beam and laser welding. *Journal of Applied Physics* 1976;47(5):2165-2174.

- [24] Thermal effects of substrate materials used in the laser curing of particulate silver inks. ; 2007.
- [25] Rowshan R. Thermal and Metallurgical Modelling of Laser Transformation Hardened Steel Parts. Materials Science Forum 2007;537-538:599.
- [26] Wallenberger FT. Rapid Prototyping Directly From the Vapour Phase. Science 3 1995;267:1274.
- [27] Scarparo MAF, Chen QJ, Miller AS, Zhang JH, Allen SD. Mechanisms of carbon dioxide laser stereolithography in epoxy-based materials. J Appl Polym Sci 1996;62(3):491-500.
- [28] Chung J, Ko S, Grigoropoulos CP, Bieri NR, Dockendorf C, Poulikakos D. Damage-Free Low Temperature Pulsed Laser Printing of Gold Nanoinks On Polymers. Journal of Heat Transfer 2005;127(7):724-732.
- [29] Schuöcker D. Handbook of the EuroLaser Academy, Volume 2. 1st ed.: Chapman and Hall; 1998.
- [30] Peet MJ, Hasan HS, Bhadeshia HK. Prediction of thermal conductivity of steel. International Journal of Heat and Mass Transfer 2011;54:2602-2608.
- [31] Semak VV, Damkroger B, Kempka S. Temporal evolution of the temperature field in the beam interaction zone during laser material processing. J Phys D 1999;32(15):1819.
- [32] Kim W, Sim B. Study of thermal behaviour and fluid flow during laser surface heating of alloys. Numerical Heat Transfer, Part A: Applications 1997;31(7):703-723.
- [33] Shi Y, Yi P, Liu Y. Numerical investigation of temperature field of different mechanisms in laser forming. Proc Inst Mech Eng Part C 2011;226(2):1.
- [34] Yu TX, Zhang L. Plastic bending: theory and applications. 1st ed.: World Scientific Publishing; 1996.
- [35] Schuocker D. Forming, Sintering and Rapid Prototyping. Handbook of the Eurolaser Academy. 2nd ed.; 1998. p. 410.

- [36] Che Jamil MS, Sheikh MA, Li L. A study of the effect of laser beam geometries on laser bending of sheet metal by buckling mechanism. *Optics & Laser Technology* 2011 2;43(1):183-193.
- [37] Pirch N, Wissenbach K. Mechanisms during laser bending. 2008 *Journal of Laser Applications*;20(3):135.
- [38] Edwardson SP, Watkins KG, Dearden G, French P, Magee J. Strain gauge analysis of laser forming. 2003 *Journal of Laser Applications*;15(4):225.
- [39] Edwardson SP, Abed E, Bartkowiak K, Dearden G, Watkins KG. Geometrical influences on multi-pass laser forming. *J Phys D* 2006;39(2):382.
- [40] Vollertsen F, Arnet H. Extending Laser Bending for the Generation of Convex Shapes. *Proc Inst Mech Eng Part B* 1995;209(6):433.
- [41] Vollertsen F, Komel I, Kals R. The laser bending of steel foils for microparts by the buckling mechanism-a model. *Modell Simul Mater Sci Eng* 1995;3(1):107.
- [42] Shi Y, Liu Y, Yi P, Hu J. Effect of different heating methods on deformation of metal plate under upsetting mechanism in laser forming. *Optics & Laser Technology* 2012 3;44(2):486-491.
- [43] Incropera F. *Fundamentals Of Heat And Mass Transfer*. 5th ed.: Wiley India Pvt. Limited; 2009.
- [44] Li W, Lawrence Yao Y. Numerical and Experimental Investigation of Convex Laser Forming Process. *Journal of Manufacturing Processes* 2001;3(2):73-81.
- [45] Shi Y, Yao Z, Shen H, Hu J. Research on the mechanisms of laser forming for the metal plate. *Int J Mach Tools Manuf* 2006 10;46(12–13):1689-1697.
- [46] Kou S, Sun D, Le Y. A Fundamental Study of Laser Transformation Hardening. *Metallurgical and Materials Transactions A* 1983;14(3):643-653.
- [47] Johnson W, Mehi K. Reaction Kinetics of Nucleation and Growth. *Trans TMS/LIME* 1939;135:416.

- [48] Avrami M. Kinetics of Phase Change - General Theory. *Journal of Chemical Physics* 1939;7(12):1103.
- [49] Avrami M. Kinetics of Phase Change. II Transformation - Time Relations for Random Distribution of Nuclei. *Journal of Chemical Physics* 1940;8(2):212.
- [50] Avrami M. Granulation, Phase Change, and Microstructure Kinetics of Phase Change. III. *Journal of Chemical Physics* 1941;9(2):177.
- [51] Zhang W, Elmer JW, DebRoy T. Kinetics of Ferrite to Austenite Transformation During Welding of 1005 Steel. *Scripta Materialia* 2002;46:753-757.
- [52] Ashby M, Shercliff H, Cebon D. *Materials: engineering, science, processing and design*. 2nd ed.: Butterworth-Heinmann; 2010.
- [53] Callister WD, Rethwisch DG. *Materials Science and Engineering*. 7th ed.: Wiley; 2011.
- [54] Mohammad Reza Allazadeh. *The Effect of Cooling Rate on the Microstructure Configuration of Continuously Cast Steel Slabs* University Of Pittsburgh.
- [55] Bhadeshia HK, Bhadeshia K, Honeycombe R. *Steels: Microstructure and Properties*. 3rd ed.: Butterworth-Heinemann; 2006.
- [56] Canova P, Ramous E. Carburization of Iron Surface Induced by Laser Heating. 1986 *Journal of Materials Science*;21:2143-2146.
- [57] Katsamas AI, Haidemenopolous GN. Laser-beam carburizing of low alloy steels. *Surface Coatings Technology* 2001;139:183-191.
- [58] Atkins P, Paula J. *Physical Chemistry*. 7th ed. Oxford: Oxford University Press; 2002.
- [59] Shen H, Vollertsen F. Modelling of laser forming – An review. *Computational Materials Science* 2009 10;46(4):834-840.
- [60] Cheng PJ, Lin SC. Using neural networks to predict bending angle of sheet metal formed by laser. *Int J Mach Tools Manuf* 2000 6;40(8):1185-1197.

- [61] Cheng JG, Yao YL. Process synthesis of laser forming by genetic algorithm. *Int J Mach Tools Manuf* 2004 12;44(15):1619-1628.
- [62] Model for the temperature gradient mechanism of laser bending. ; *Proceedings of the LANE*; ; 1994.
- [63] Yau CL, Chan KC, Lee WB. A new analytical model for laser bending. *Laser Assisted Net Shape Engineering 2, Proceedings of the LANE* 1997;2:357.
- [64] Liu FR, Chan KC, Tang CY. Theoretical analysis of deformation behavior of aluminum matrix composites in laser forming. *Materials Science and Engineering: A* 2005;396(1&2):172.
- [65] Shen H, Shi Y, Yao Z, Hu J. An analytical model for estimating deformation in laser forming. *Computational Materials Science* 2006 10;37(4):593-598.
- [66] Shi Y, Shen H, Yao Z, Hu J. An analytical model based on the similarity in temperature distributions in laser forming. *Optics and Lasers in Engineering* 2007 1;45(1):83-87.
- [67] Yang X. *A First Course in Finite Element Analysis*. 1st ed.: Luniver Press; 2007.
- [68] Ji Z, Wu S. FEM simulation of the temperature field during the laser forming of sheet metal. *J Mater Process Technol* 1998 2;74(1-3):89-95.
- [69] Shichun W, Zhong J. FEM simulation of the deformation field during the laser forming of sheet metal. *J Mater Process Technol* 2002 2/28;121(2-3):269-272.
- [70] Zhang P, Guo B, Shan D, Ji Z. FE simulation of laser curve bending of sheet metals. *J Mater Process Technol* 2007 4/12;184(1-3):157-162.
- [71] Zhang P, Liu H. FEM Realization of Laser Curve Bending Process. 2011;144:300-305.
- [72] Kyrsanidi AK, Kermanidis TB, Pantelakis SG. Numerical and experimental investigation of the laser forming process. *J Mater Process Technol* 1999 3/15;87(1-3):281-290.

- [73] Hu Z, Labudovic M, Wang H, Kovacevic R. Computer simulation and experimental investigation of sheet metal bending using laser beam scanning. *Int J Mach Tools Manuf* 2001 3;41(4):589-607.
- [74] Cheng J, Yao YL. Microstructure Integrated Modeling of Multiscan Laser Forming. *Journal of Manufacturing Science and Engineering* 2002;124(2):379-388.
- [75] Shen H, Shi Y, Yao Z. Numerical simulation of the laser forming of plates using two simultaneous scans. *Computational Materials Science* 2006 9;37(3):239-245.
- [76] Prithwani I, Otto A, Schmidt M, Griffiths J, Watkins K, Edwardson S, et al. Laser Beam Forming of Aluminium Plates under Application of Moving Mesh and Adapted Heat Source. *Proceedings of the Fifth International WLT-Conference on Lasers in Manufacturing* 2009.
- [77] Pitz I, Otto A, Schmidt M. Simulation of the laser beam forming process with Moving Meshes for large aluminium plates. *Physics Procedia* 2010;5, Part B(0):363-369.
- [78] Pitz I, Otto A, Schmidt M. Meshing strategies for the efficient computation of laser beam forming processes on large aluminium plates. *International Journal of Material Forming* 2010;3(0):895-898.
- [79] Fan Y, Yang Z, Cheng P, Egland K, Yao L. Investigation of Effect of Phase Transformations on Mechanical Behavior of AISI 1010 Steel in Laser Forming. *Journal of Manufacturing Science and Engineering* 2007;129(1):110-116.
- [80] Bhadeshia HK, Svensson LE. Modelling the Evolution of Microstructure in Steel Weld Metal. *Mathematical Modelling of Weld Phenomena* 1993:109.
- [81] Hao N, Li L. An analytical model for laser tube bending. *Appl Surf Sci* 2003 3/15;208–209(0):432-436.
- [82] Hsieh H, Lin J. Study of the buckling mechanism in laser tube forming. *Optics & Laser Technology* 2005;37(5):402.
- [83] Hsieh H, Lin J. Study of the buckling mechanism in laser tube forming with axial preloads. *Int J Mach Tools Manuf* 2005;45(12):1368.

- [84] Yanjin G, Sheng S, Guoqun Z, Yiguo L. Finite element modeling of laser bending of pre-loaded sheet metals. *J Mater Process Technol* 2003 11/25;142(2):400-407.
- [85] Safdar S, Li L, Sheikh MA, Liu Z. Finite element simulation of laser tube bending: Effect of scanning schemes on bending angle, distortions and stress distribution. *Optics & Laser Technology* 2007;39(6):1101.
- [86] J. Griffiths. *Simulation of Laser Heating Using COMSOL Multiphysics* University of Liverpool; 2008.
- [87] Griffiths J, Edwardson SP, Dearden G, Watkins KG. Modelling of Real Temporally variant Beam Shapes in Laser Materials Processing. *Proceeding of ICALEO '11* 2011.
- [88] Che Jamil MS, Li L. Understanding the effect of non-conventional laser beam geometry on material processing by finite-element modelling. *Proc Inst Mech Eng Part C* 2009;224:1061.
- [89] Che Jamil MS, Li L. A Numerical Study of the Temperature Gradient Mechanism in Laser Forming Using Different Laser Beam Geometries. *Lasers in Engineering*;22:413-428.
- [90] Che Jamil MS, Sheikh MA. A study of the effect of laser beam geometries on laser bending of sheet metal by buckling mechanism. *Optics & Laser Technology* 2011;43:183-193.
- [91] Zheng C, Sun S, Ji Z, Wang W, Liu J. Numerical simulation and experimentation of micro scale laser bulge forming. *Int J Mach Tools Manuf* 2010 12;50(12):1048-1056.
- [92] Ocaña JL, Morales M, García-Ballesteros JJ, Porro JA, García O, Molpeceres C. Laser shock microforming of thin metal sheets. *Appl Surf Sci* 2009 3/1;255(10):5633-5636.
- [93] Bechtold P, Schmidt M. Non-thermal Micro Adjustment Using Ultrashort Laser Pulses. *Journal of Laser Micro/Nanoengineering* 2007;2(3).
- [94] Edwards K, Edwardson S, Carey C, Dearden G, Watkins K. Laser micro peen forming without a tamping layer. *The International Journal of Advanced Manufacturing Technology* 2010;47(1):191-200.

- [95] Hua D, Yun W, Lan C. Laser shock forming of aluminum sheet: Finite element analysis and experimental study. *Appl Surf Sci* 2010 1/1;256(6):1703-1707.
- [96] Liu H, Shen Z, Wang X, Wang H, Tao M. Micromould based laser shock embossing of thin metal sheets for MEMS applications. *Appl Surf Sci* 2010 5/1;256(14):4687-4691.
- [97] Hoving W. Accurate Manipulation Using Laser Technology. *Proc SPIE* 1997:284-295.
- [98] Tam AC, Poon CC, Crawford L., Laser Bending of Ceramics and Application to Manufacture Magnetic Head Sliders in Disk Drives. *Analytical Sciences* 2001;17.
- [99] Singh G, Wu Z, Brown B, Kozlovsky W. Laser Gram Load Adjust for Improved Disk Drive Performance. 2001 *IEEE Transactions on Magnetics*;37(2):959.
- [100] Gartner E, Fruhauf J, Loschner U, Exner H. Laser Bending of Etched Silicon Microstructures. *Microsystem Technologies* 7 2001:23-26.
- [101] Wu W, Liang NG, Gan CH, Yu G. Numerical investigation on laser transformation hardening with different temporal pulse shapes. *Surface and Coatings Technology* 2006 1/24;200(8):2686-2694.
- [102] Shen H. Mechanism of Laser Micro-Adjustment. *Journal of Physics D* 2008;41:9.
- [103] Shen H, Peng L, Hu J, Yao Z. Study on the mechanical behaviour of Laser Micro-Adjustment of Two-Bridge Actuators. *Journal of Micromechanics and Microengineering* 2010;20.
- [104] Shen H, Gong C, Hu J, Yao Z. Numerical and experimental study on bi-direction deformations in laser micro forming of two-bridge actuators. *Int J Mach Tools Manuf* 2012 0;54–55(0):66-72.
- [105] Guan Y, Zhang H, Liu J, Sun S. Laser micro-bending process based on the characteristic of the laser polarization. *J Mater Process Technol* 2012 3;212(3):662-671.
- [106] COMSOL. COMSOL MultiPhysics. 2008;3.5a.
- [107] MathWorks. MATLAB. 2009;2009a.
- [108] Carslaw HC, Jaeger JC. Conduction of heat in solids. 2nd ed.: Clarendon Press; 1986.

- [109] Dowling NE. Mechanical Behaviour of Materials. 4th ed. USA: Pearson; 2012.
- [110] Honeycombe R. Steels: Microstructure and Properties. 1st ed. Colchester, UK: Edward Arnold; 1981.
- [111] Zhang W, Elmer JW, DebRoy T. Modeling and real time mapping of phases during GTA welding of 1005 steel. Materials Science and Engineering: A 2002;320-335.
- [112] Elmer JW, Wong J, Ressler T. Spatially resolved X-ray diffraction mapping of phase transformations in the heat-affected zone of carbon-manganese steel arc welds. Metallurgical and Materials Transactions 2001;A(32):1175.
- [113] ASM Metals Handbook. 10th ed.: ASM International; 1990.
- [114] Edwardson S, Griffiths J, Dearden G, Watkins K. Temperature gradient mechanism: Overview of the multiple pass controlling factors. Physics Procedia 2010;5:53-63.
- [115] Verhoeven JD. Steel Metallurgy for the Non-Metallurgist. 1st ed. USA: ASM International; 2007.
- [116] Van Vlack LH. Elements of Materials Science and Engineering. 6th ed. New York (USA): Addison-Wesley Publishing; 1990.
- [117] Mitchell C. Carbon and alloy steels. In: Boyer HE, Gall TL, editors. Metals Handbook Desk Edition. 1st ed. Orlando (USA): Taylor & Francis Group.
- [118] Effects of Laser Interaction with Graphite Coatings. Laser Assisted Net Shape Engineering 5; 2007.
- [119] Bao J, Yao YL. Analysis and Prediction of Edge Effects in Laser Bending. Journal of Manufacturing Science and Engineering 2001;123(1):53-61.
- [120] Cheng J, Yao L. Cooling Effects in Multiscan Laser Forming. Journal of Manufacturing Processes 2001;3(1):60.
- [121] Silve S, Steen WM, Podschier B. Laser forming tubes: a discussion of principles ICALEO '98; Laser Materials Processing Conference 1998 16-19 Nov.

- [122] Garino TJ, Morales A, Buchheit T, Boyce B. The Fabrication of Stainless Steel Parts for MEMs. *Mater Res Soc Symp Proc* 2002;687:149.
- [123] Mannion P, Magee J, Coyne E, O’Conner G. Ablation thresholds in ultrafast micro-machining of common metals in air. *Proc Of SPIE* 2003;4876.
- [124] Mannion PT, Magee J, Coyne E, O’Connor GM, Glynn TJ. The effect of damage accumulation behaviour on ablation thresholds and damage morphology in ultrafast laser micro-machining of common metals in air. *Appl Surf Sci* 2004 6/30;233(1–4):275-287.
- [125] Singh G, Brown B, Werlich W, Kozlovsky W. Laser Processing to Adjust the Suspension Preload of Magnetic Recording Head Stack Assemblies. 2000 *IEEE Transaction of magnetics*;36(5):2724.
- [126] Vollertsen F, editor. IWOTE '11. 3rd International Workshop on Thermal Forming and Weld Distortion; April 6-7th; Bremen, Germany: Verlag; 2001.
- [127] J. Cheng. Ultrafast Picosecond Laser Micromachining of Metallic Materials University of Liverpool; 2010.
- [128] Cezairliyan A, Miiller AP. Thermophysical measurements on low carbon 304 stainless steel above 1400 K by a transient (subsecond) technique. *Int J Thermophys* 1980;1(1):83-95.

Appendix A

FINITE ELEMENT MODEL VALIDATION

The FE thermo-mechanical simulation detailed in Chapter 4, Section 4.1 was validated against experimentally determined temperature and bend angle data, as detailed in the following subsections.

A.1 Thermal analysis

Initially the simulated transient temperature profile at three positions on the top surface away from the central irradiation path was compared to results from analogous experimentation conducted using the same experimental and numerical set up as detailed in Chapter 5.

Thermocouples were used to measure the temperature in the experiments. These sensors are composed of two dissimilar metals, producing an electric potential of which temperature is a function. Therefore, by passively measuring the voltage drop across the two dissimilar metals the transient temperature can be determined.

Three K-type (composed of Nickel chromium (positive) and Nickel Aluminium (negative)) thermocouples were welded in an inert atmosphere to the upper surface of an 80 x 200 x 1.5 mm AISI 1010 steel substrate at 10, 22 and 34 mm away from the irradiation path on the unclamped side of the component. Both the distance from the irradiation path and between thermocouples was dictated by the method of fixing the thermocouple tips in position. Adhesive thermal pads were used, which offered heat resistance up to approximately 530 K. This limited the proximity at which the thermocouple can be placed with respect to the irradiation path. The minimum spacing of the thermocouples was approximately 12 mm due to the width of each thermo pad.

K-type thermocouples were chosen due to their suitability over the temperature range encountered under typical TGM conditions, having a linear temperature range of -270 °C to

1372 °C. A data logger (34970A, Agilent Technologies UK Ltd.) was used to record the data, which had a maximum bandwidth of 250 Hz and an on-board calibrated reference junction, therefore not requiring manual calibration.

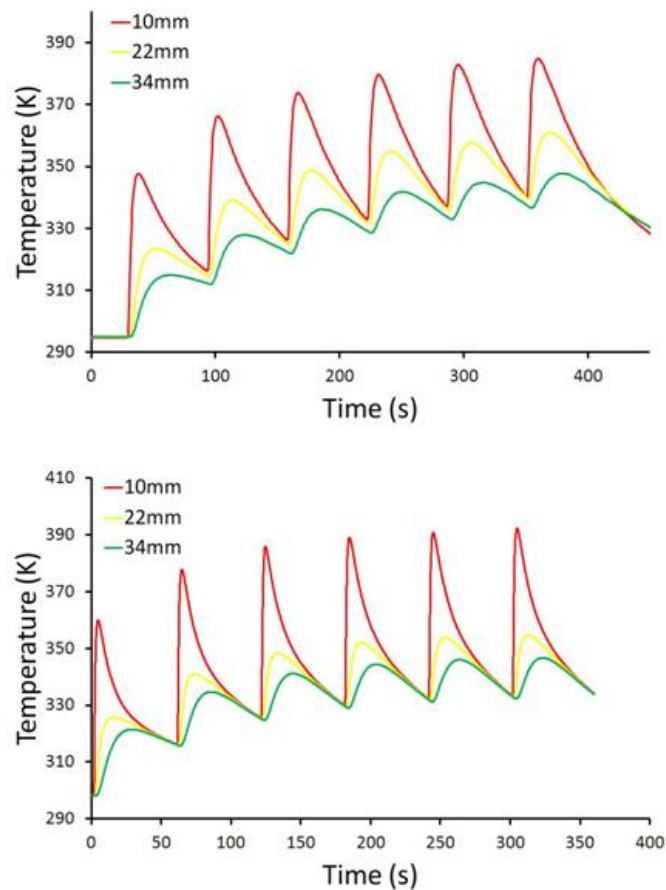


Figure A.1. 1 - Experimental (top) and simulated (bottom) transient temperature profiles at three distances away from the central irradiation path.

Figure A.1.1 reveals a good correlation between the experimental and simulated temperature profiles.

A.2 Bend angle analysis

Subsequent to thermal validation, a full parametric study was conducted in order to validate the structural mechanical properties of the model. It is worth noting that in this investigation a truncated 30 x 80 x 1.5 mm component was used to save material.

The study consisted of measuring the initial bend angle in straight line laser forming of an edge clamped component, using the same experimental and numerical set up as detailed in Chapter 5. Powers, traverse speeds and spot sizes were selected which represented a suitable range for TGM laser forming on the ElectroX system, as detailed in Table A1.

Power [W]	Traverse speed [mm/s]	Distance from focus [mm]
200	30	20
500	50	40
800	80	60

Table A 1 – Process parameters used in parametric study.

The distance from focus refers to the z-height on the 3-axis CNC system on the ElectroX, which is an effective way of controlling the laser beam diameter incident on the workpiece. The distances of 20, 40 and 60 mm correspond to beam diameters of 4, 6 and 8 mm respectively.

Using the process parameters listed in Table A1, a full parametric sweep (Table A2) was conducted both experimentally and numerically.

Iteration no.	Power [W]	Traverse speed [mm/s]	Distance from focus [mm]
1	200	20	20
2	200	20	40
3	200	20	60
4	200	50	20
5	200	80	20
6	200	50	40
7	200	80	40
8	200	50	60
9	200	80	60
10	500	20	20
11	500	20	40
12	500	20	60
13	500	50	20

Modelling of Laser Forming at Macro and Micro Scales

14	500	80	20
15	500	50	40
16	500	80	40
17	500	50	60
18	500	80	60
19	800	20	20
20	800	20	40
21	800	20	60
22	800	50	20
23	800	80	20
24	800	50	40
25	800	80	40
26	800	50	60
27	800	80	60

Table A 2 – Process parameters used for each iteration of the parametric study.

The results of the parametric sweep are depicted in Figure A.2.1, revealing a good correlation between experimentally determined and numerically simulated initial bend angle.

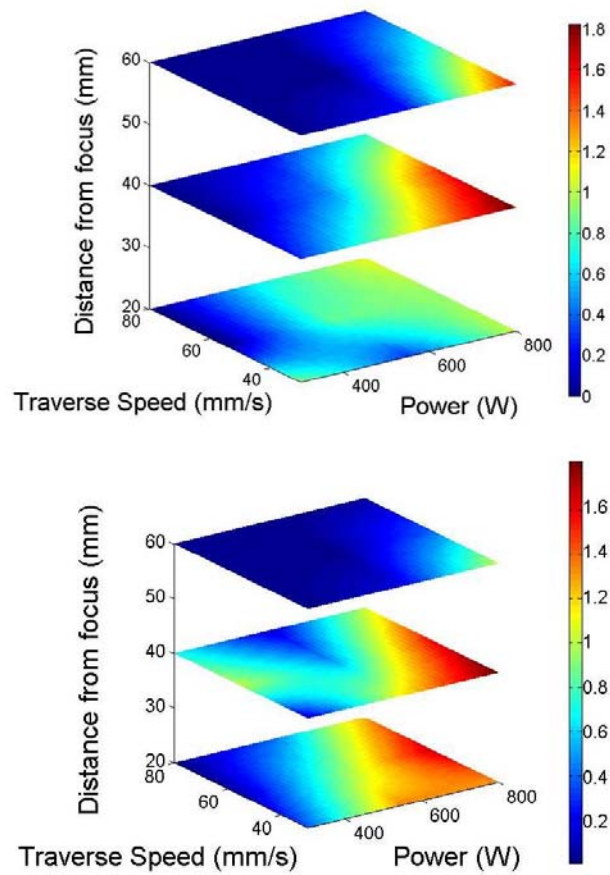


Figure A.2. 1 - Experimental (top) and simulated (bottom) initial bend angle in degrees as a function of traverse speed, power and distance from focus.

Appendix B

TEMPERATURE DEPENDENT MATERIAL PROPERTIES

B.1 AISI 1010 Mild Steel

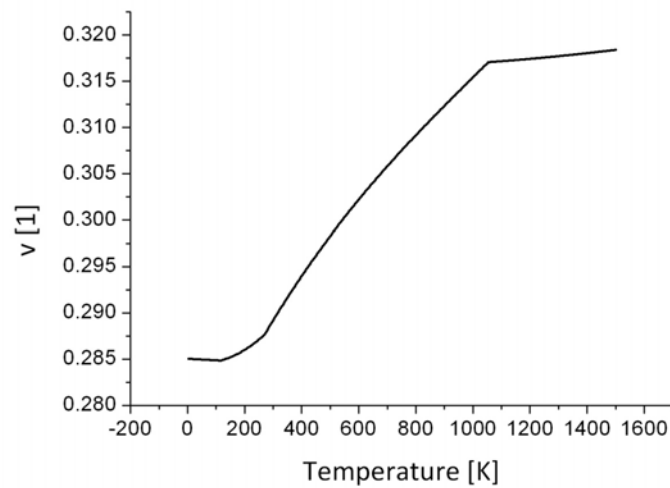


Figure B.1. 1 - Temperature dependent Poisson's ratio for AISI 1010 mild steel.

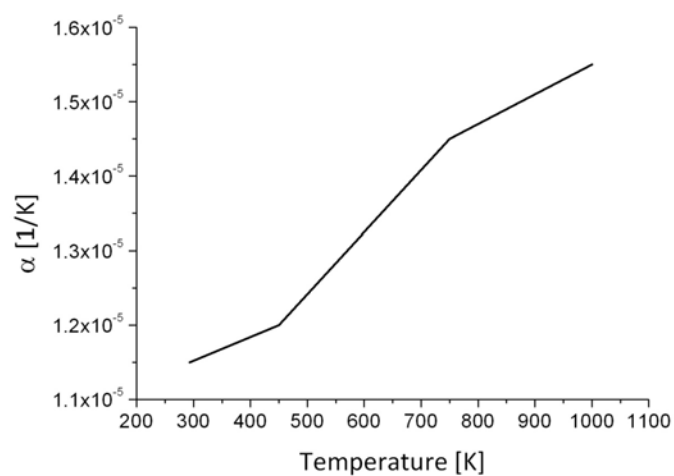


Figure B.1. 2 - Temperature dependent thermal expansion coefficient for AISI 1010 mild steel.

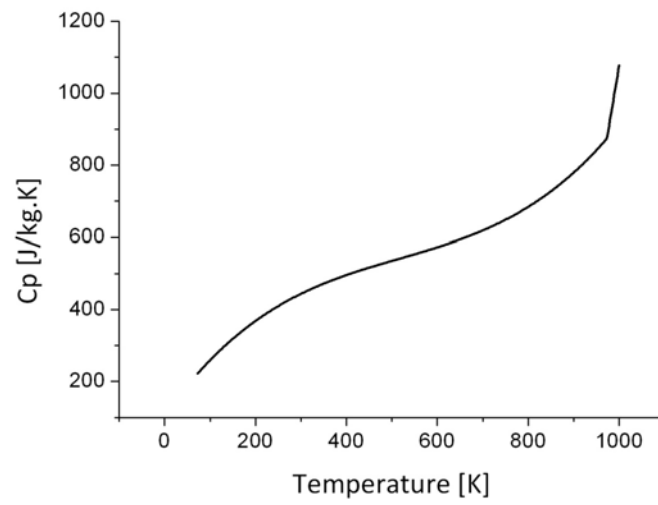


Figure B.1. 3 - Temperature dependent specific heat capacity for AISI 1010 mild steel.

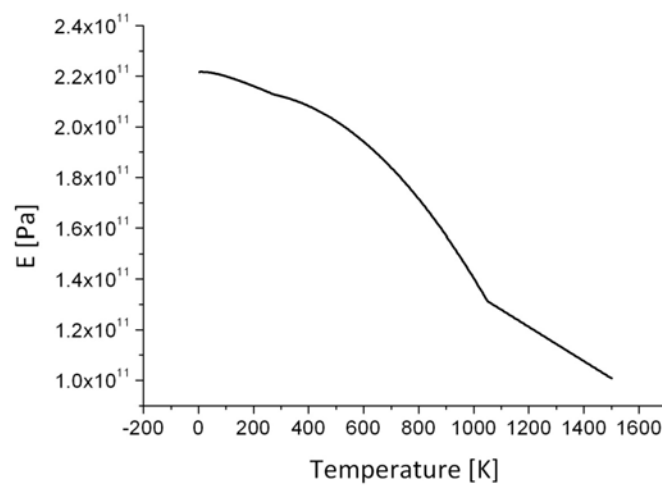


Figure B.1. 4 - Temperature dependent Young's modulus for AISI 1010 mild steel.

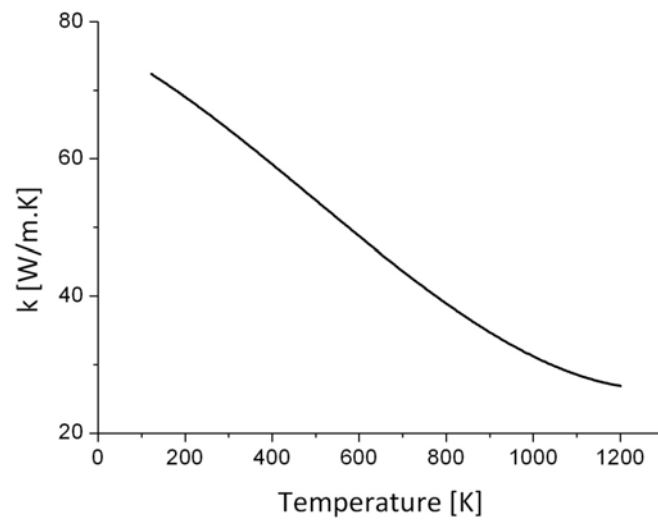


Figure B.1. 5 - Temperature dependent thermal conductivity for AISI 1010 mild steel.

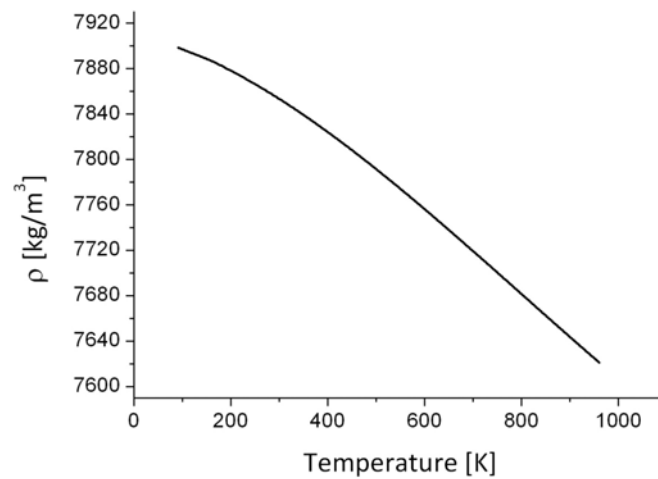


Figure B.1. 6 - Temperature dependent density for AISI 1010 mild steel.

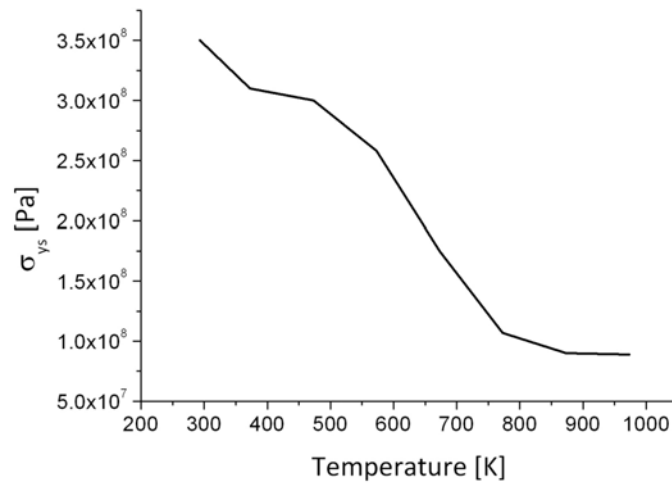


Figure B.1. 7 - Temperature dependent yield strength for AISI 1010 mild steel.

B.2 AISI 302 Stainless Steel

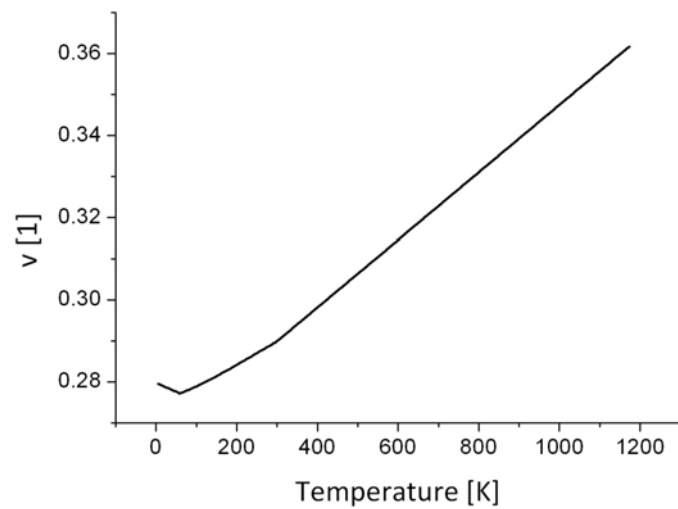


Figure B.2. 1 - Temperature dependent Poisson's ratio for AISI 304 stainless.

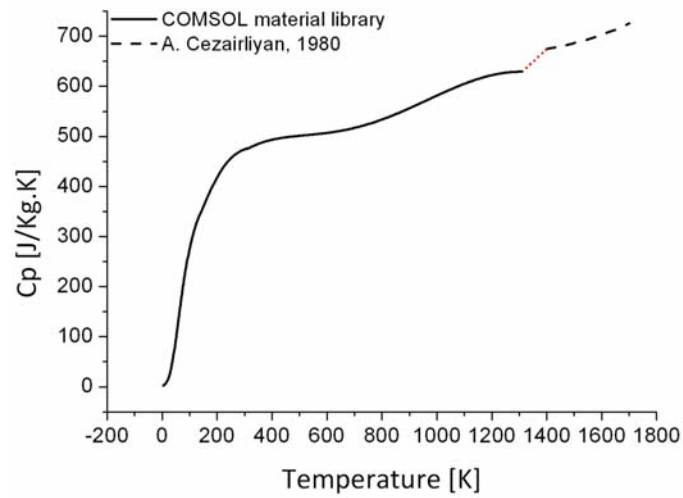


Figure B.2. 2 - Temperature dependent specific heat capacity for AISI 304 stainless steel [128].

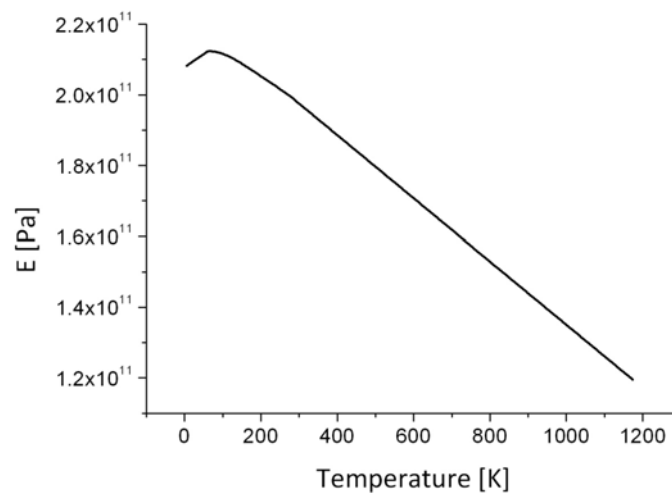


Figure B.2. 3 - Temperature dependent Young's modulus for AISI 304 stainless steel.

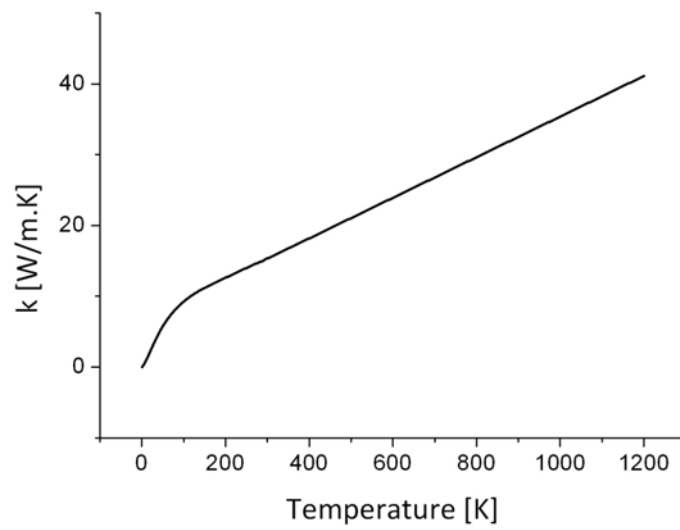


Figure B.2. 4 - Temperature dependent thermal conductivity for AISI 304 stainless steel.

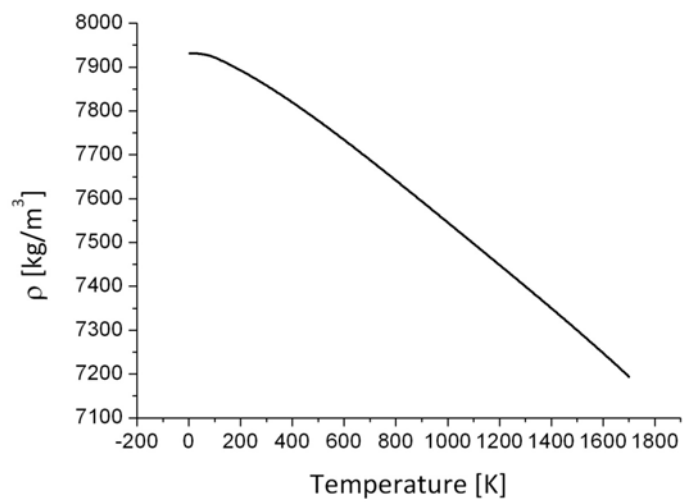


Figure B.2. 5 - Temperature dependent density for AISI 304 stainless steel.

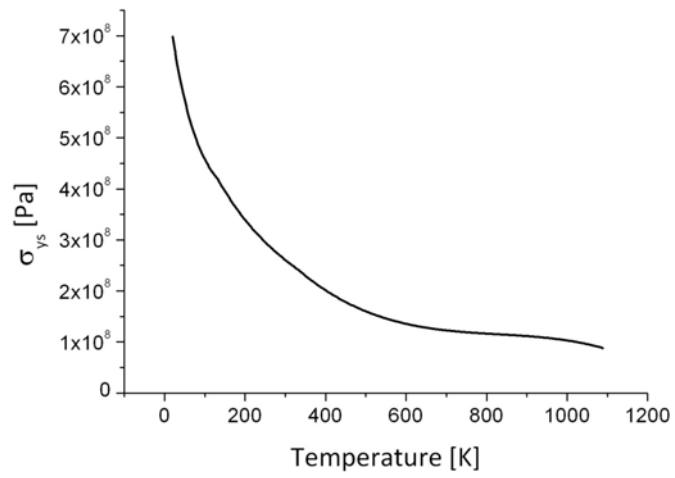


Figure B.2. 6 - Temperature dependent yield strength for AISI 304 stainless steel.

Appendix C

CODE EXAMPLES

C.1 MATLAB code

C.1.1 FDM diffusion model

```
% COUPLED_FDM_COMPLETE.m

clear all
clc

% Import time/temperature data from COMSOL Multiphysics
DATA = importdata('T.txt');
timeDATA = DATA(:,1);
Temp = DATA(:,2);
[timeDATA,ind] = unique(timeDATA(:,1)); % Finds unique time values and
records their index number
Temp = Temp(ind,1); % Creates array of T values which correspond to the
unique time index numbers
sizeDATA = size(Temp);
sizeDATA = sizeDATA(1,1);
Tmin = min(timeDATA);
timeDATA = timeDATA(:,1)-Tmin;
Tmax = max(timeDATA);

% Physical parameters
L = 0.0015; % Domain length (m)
C0 = 0.13; % Initial carbon concentration of steel (%wt)
Lt = Tmax; % Overall solution time (s)
Tamb = 298.15; % Temperature of steel at room temperature (K)
alpha = 0.17e-5; % Thermal diffusivity (m2/s)
R = 8.3; % Boltzmann constant (J/mol/K)
Q = 1.42e5;
D0 = 2e-5; % Proportionality constant (m^2/s)
TT = 1163;

% Set spatial/temporal mesh parameters
nxt = 5; % Number of nodes (Heat equation)
nx = 1500; % Number of nodes (Fick's second law)
nt = sizeDATA; % Number of timesteps
dt = Lt/nt; % Timestep (s)
dx = L/(nx-1); % Node spacing (Fick's second law)
dxt = L/(nxt-1); % Node spacing (Heat equation)
x = 0/2:dx:L; % Mesh (Fick's second law)
xt = 0/2:dxt:L; % Mesh (Heat equation)
```



```
% Initial conditions
C = ones(size(x))*C0;
T = ones(size(xt))*Tamb;
time = 0;

for n=1:nt % Timestep loop

    Tnew = T;%ones(1,nxt)*Tamb;
    Cnew = zeros(1,nx);

    % Solve heat equation for current time step
    for i =2:nxt-1
        Tnew(i) = T(i)+(alpha*dt)*((T(i+1)-(2*T(i))+T(i-1))/(dxt^2));
    end

    % Interpolate temperature distribution data to match diffusion
    element
    % number
    stept = L/nx;
    y = Tnew;
    y(1,1) = Temp(n,1);
    xi = 0:stept:L-stept;
    yi = interp1(xt,y,xi);
    yi(isnan(yi)) = 0;

    % Solve Fick's second law for current time step
    for i=2:nx-1
        if yi(i-1) > TT
            D = D0*exp(-Q/(R*yi(i-1)));
        else
            D = 0;
        end
        Cnew(i) = C(i)+(D*dt)*((C(i+1)-(2*C(i))+C(i-1))/(dx^2));
    end

    % Set boundary conditions
    Cnew(1) = 2;%T(1);
    Cnew(nx) = C(nx);
    Tnew(1) = Temp(n,1);%T(1);

    % Update temperature and time
    T = Tnew;
    C = Cnew;
    time = time+dt;

    % Plot
    figure(1), clf
    ax(1)=subplot(2,1,1);
    [AX,H1,H2] = plotyy(x,Cnew,x,yi);
    xlabel('x (m)')
    set(get(AX(1),'Ylabel'),'String','C (%/wt)')
    set(get(AX(2),'Ylabel'),'String','T (K)')
    title([num2str(time),' seconds'])
```

```
    xlim([0 0.0015])
    xlim(AX(2),[0 0.0015]);
    ax(2)=subplot(2,1,2);
    plot(timeDATA,Temp);
    hold on
    scatter(time,Temp(n,1))
    xlabel('x (m)')
    ylabel('Temperature (K)')
    xlim([0 Lt])
    drawnow
end

figure(2)
plot(x*1e6,Cnew)
hold on
plot(x*1e6, repmat(C0, length(x*1e6), 1), 'r--')
h = legend('Additional carbon content', 'Initial carbon content', 2);
xlabel('z (\mum)')
ylabel('C (%/wt)')
xlim([0 20])
ylim([0 3])
```

C.1.2 Analytical phase transformation model

```
%martensite_analytical v1.3
%J. Griffiths, Il Busca
%09-08-2010

clear all; close all; clc;

load T.txt

% Remove duplicate time-step data
[t,ind] = unique(T(:,1)); %Finds unique time values and records their
index number
T = T(ind,2); % Creates array of T values which correspond to the unique
time index numbers

n = 1.9;          % JMA time exponent
k0 = 1.33e5;      % Pre-exponential constant
Q = 117.07;       % Activation energy of transformation kJ/mol-1
R = 8.31e-3;      % Universal gas constant kJK-1mol-1
A1 = 996.15;      % A1 temperature
CCR = -450;       % Critical cooling rate for martensitic transformation

k_all = k0*exp(-Q./(R*T));
indx = find(T>A1);
k = zeros(size(t));
k(indx) = k_all(indx);
```

```
resetpoint = [];  
resetpointup = indx(1);  
  
for count=1:size(indx,1)-1  
    if indx(count+1)==indx(count)+1  
    else  
        resetpoint = [resetpoint; indx(count)];  
        resetpointup = [resetpointup; indx(count+1)];  
    end  
end  
resetpoint = [resetpoint; indx(end)];  
  
deltat = t(2:end)-t(1:end-1);  
deltat = [0;deltat];  
  
dT = T(2:end)-T(1:end-1);  
dT = [0;dT];  
  
CR_all = zeros(size(t));  
CR_all = dT./deltat;  
  
indx2 = find(CR_all<CCR);  
CR = zeros(size(t));  
CR(indx2) = CR_all(indx2);  
  
resetpoint2 = [];  
for count=1:size(indx2,1)-1  
    if indx2(count+1)==indx2(count)+1  
    else  
        resetpoint2 = [resetpoint2; indx2(count)];  
    end  
end  
resetpoint2 = [resetpoint2; indx2(end)];  
  
startp = 1;  
f = zeros(size(t));  
  
for count=1:length(resetpoint)  
    kt = 0;  
    for count2=startp:resetpoint(count)  
        kt = kt+k_all(count2)*deltat(count2);  
        f(count2,1) = 1-exp(-kt^n);  
    end  
    if count<length(resetpoint)  
        startp = resetpoint(count)+1;  
    else  
        f(resetpoint(count)+1:length(t))=zeros(length(t)-  
resetpoint(count),1);  
    end  
end
```

```
indx3 = find(f>0.001);
resetpoint3 = [];
for count3=1:size(indx3,1)-1
    if indx3(count3+1)==indx3(count3)+1
    else
        resetpoint3 = [resetpoint3; indx3(count3)];
    end
end
resetpoint3 = [resetpoint3; indx3(end)];

Vm = zeros(size(t));

startp = 1;
for count2=startp:resetpoint3(1)
    Vm(count2,1) = f(count2,1);
end

startp=count2;
for count=2:length(resetpoint2)
    for count2=startp+1:resetpointup(count)
        Vm(count2,1) = Vm(startp,1);
    end
    for count2=resetpointup(count):resetpoint3(count)
        Vm(count2,1) = f(count2,1);
    end
    startp=count2;
    for count3=resetpoint3(count):resetpoint2(count)
        Vm(count3,1)=Vm(startp,1);
    end
    if count<length(resetpoint2)
        startp = resetpoint2(count);
    else

Vm(resetpoint2(count)+1:length(t))=repmat(Vm(resetpoint2(count)),length(r
esetpoint2(count)+1:length(t)),1);
    end

end

TEXT = ['martensite_analytical v1.3, J. Griffiths, Il Busca, 09/08/10'];
disp(TEXT);

figure
ax(1)=subplot(3,1,1);
plot(t,T)
hold on
plot(t,repmat(A3,length(t),1),'r--')
xlabel('Time (s)')
ylabel('Temperature (K)')

ax(2)=subplot(3,1,2);
```

```
plot(t,f);
hold on
plot(t,Vm,'r')
h = legend('\gamma-iron', 'Martensite', 2);
xlabel('Time (s)')
ylabel('f')
linkaxes(ax,'x');

ax(3)=subplot(3,1,3);
plot(t,CR_all);
hold on
plot(t(resetpoint2),CR_all(resetpoint2),'ro')
xlabel('Time (s)')
ylabel('dT/dt [K/s]')
linkaxes(ax,'x');
```

C.2 Visual BASIC code

C.2.1 Example of linear interpolation

```
#Z1 % Start program
SB3 % Arm shutter
SP14000.000000,14000.000000 % Set x,y speed
AC450000.000000,450000.000000 % Set acceleration
DC450000.000000,450000.000000 % Set deceleration
CB3 % Open shutter
WT200.000000
LM XY % begin linear interpolation sequence
VA450000.000000 % Set vector acceleration
VD450000.000000 % Set vector deceleration
DP0.000000,0.000000 % Set current co-ordinates to zero
LI0.000000,0.000000<14000.000000>14000.000000
LI2465480.828582,399885.644433<14000.000000>14000.000000
LI2226081.446957,399873.865166<14000.000000>14000.000000
LI1769744.555855,399941.752808<14000.000000>14000.000000
LE % End linear interpolation sequence
BGS % Begin movement
AM
CB3 % Close shutter
EN % End
```